POLITECNICO DI TORINO

Master's Degree
in
Electronic Engineering – Electronic for micro and nanosystems

Study of gate polarization in an Electrolyte Gated Organic Transistor

Supervisor:
Prof. Matteo Cocuzza

Co-supervisor:
Dr. Simone Marasso

Candidate:
Alessandro Stella

Academic year 2020/2021

Abstract

The aim of this thesis is to investigate the electrical behaviour of the Electrolyte-Gated-Organic Field-Effect Transistors (EGOFETs) when working with poly[3-(5-carboxypentyl)-thiophene-2,5-diyl] (P3CPenT) as organic semiconductor with polarizable or non-polarizable gate electrodes and provided with an electrolytic solution of deionized water (DI H_2O) and sodium chloride (NaCl) at different concentrations. These devices are developed with equivalent technological process and are subjected to a complete electrical characterization according to three variables: the gate electrode, the ionic strength of the electrolyte and the scan rate of the measurements. The experiments are performed in a semi-automatized environment which includes a proper microfluidic system. The electrical characterizations are followed by the analysis of some of their main figures of merit to offer a comparison when changing one or more parameters.

Summary

Introduction

The work of this thesis was carried out at *Chilab - Materials and Microsystems Laboratory*, section of Department of Applied Science and Technology (DISAT) of Politecnico di Torino. The work done and the developed device are part of two projects Politecnico di Torino is collaborating to: the first "*Free Drug Food*" project, whose aim is to develop a miniaturized and portable platform for the detection of antibiotics in food products, specifically in honey, milk and eggs. The ultimate goal would be to be capable of monitoring any contamination in the production chain that can be potentially dangerous for consumers. The second project, called "*Digital tEchnology For Lung Cancer Treatment*" (*DEFLeCT*), has the purpose of building a digital platform to support the early diagnosis of non-small cell lung cancer (NSCLC). The development of these two projects gives the spotlight to two of the biggest classes of research for biosensors: monitoring and prevention.

Biosensors are one of the most challenging devices that the scientific community has been studying, developing, and improving for almost 60 years now, and the numerous applications where biosensors can be employed have only increased the attraction towards them in the past few decades. There are many fields where biosensors have already been exploited, such as environmental and ecological applications [1], healthcare screening [2] and diagnosis [3], prosthetic devices [4], agriculture and food analysis [5], and veterinary applications [6].

Since Ion-Sensitive Field-Effect Transistors (ISFETs) appeared in 1970, proving that Field Effect Transistors (FETs) could be used efficiently as biosensors [7]. Since then, several FET-based biosensors have been developed [8]. Among them EGOFETs, belonging to the category of Organic Field Effect Transistors (OFETs), are the focus of this thesis. EGOFETs were fabricated on a silicon substrate with a thin layer of silicon dioxide on top, interdigitated gold source and drain electrodes, and P3CPenT used as OSC. On top of that, an electrolytic solution was placed, contained in a microfluidic chamber. The gate terminal was not integrated in the technological process but immerged afterwards inside the electrolyte. The device was tested with different types of gate electrodes, namely silver/silver chloride (Ag/AgCl) and gold (Au), characterized at different scan rates ($8\ mV/s, 20\ mV/s, 80\ mV/s$) and with different electrolyte ionic strength ($1\ mM, 10\ mM, 100\ mM$) in order to understand how the behaviour of the device changes by varying these parameters and if the device can be taken a step forward into working as biosensor. To work as a biosensor, stability is a crucial parameter, and despite EGOFETs promising advantages (see *Chapter 1.3*) stability is not one of them. Medium- and long-term performance degradation affect EGOFETs and up to now, it prevented these devices to successfully enter the market. Typical instabilities are related to gate leakages, reduction of drain current and hysteresis caused by mode of operation. Due to lack of a complete understanding of these degradation mechanisms, the development of a generation of "degradation-free" EGOFET would make up a decisive step towards the implementation of EGOFETs as commercial biosensors.

First, it will be given a complete overview about organic transistors, their features and how they can be employed as biosensors. Afterwards, the focus turns to

EGOFETs, fabricated with a state-of-the-art process. Finally, experimental results will be discussed, and the comparison of the different experimental set-ups will be analysed by means of typical figures of merit.

1 CHAPTER: OTFT

1.1 Biosensors

The first biosensor appeared in 1962, produced by the biochemist L. Clark who realised an enzymatic amperometric glucose sensor. Clark, together with C. Lyon also gave the first description of a biosensor [9], that have been changing throughout the year. For the first commercial biosensor the waiting is extended to 1975, when a glucose sensor based on the so-called Clark electrode was brought into market by Yellow Spring Instruments. Today, the most modern definition of biosensor is given by IUPAC (International Union of Pure and Applied Chemistry), stating that a biosensor is "*a device which uses specific biochemical reactions mediated by isolated enzymes, immuno-systems, tissues, organelles or whole cells to detect chemical or biological compounds, usually by use of electrical, thermal or optical signals*" [10]. The definition already identifies most of the common components for a biosensor: a recognition site (bioreceptor), a biotransducer and electronic system which includes a signal amplifier and a data processing module. The bioreceptor is capable to interact and cooperate with an analyte of interest for a specific application; the result of this interaction is compatible with the transducer, whose role is to convert the biochemical measure, into an output signal that can be of various type, according to the type of bio-transducer itself.

There are many ways to classify biosensors; each way focuses on a particular point of view and distinguishes biosensors in two or more sub-families. One can splits them according to the detection method (label-free and label-based), according to type of biomolecule (single molecule and cell-based) or according to the bioreceptors and transducers. The latter is the most common classification. In the first case, biosensors are grouped in several sub-types as: antibody/antigen, cells, enzyme, tissues, etc… In the other case, biosensors are usually divided into gravimetric, electrochemical, electronic, optical, piezoelectric, pyroelectric. OFETs show advantageous features in various biomedical applications and in the healthcare sector in general: high sensitivity, high resolution, low costs, portability, and compatibility with the scaling processes of the semiconductor industry. Despite the numerous advantages, OFETs are still to be optimized before they could be considered reliable in sensing applications.

Monitoring and prevention are the two main classes of application for biosensors, and the optimization of EGOFETs presented in this work implements both. Monitoring is accomplished within *Free Drug Food*: the drug quantities desiderable to be detected in food are considerably small, so small that in daily life, the risk of "poisoning" is basically zero. For this reason, one might ask what the purpose is in detecting such small contaminations if those will not be dangerous for the health. The answer is associated to a phenomenon, called antibiotic resistance. When a drug enters the food chain (within this project the contaminant is most likely an antibiotic) the main problem is that bacteria might still be present in the body. Making an habit out of the unaware assumption of antibiotic in small doses would let the bacteria live, since the dose is too small to be effective. An even worse consequence is that the bacteria will develop a real resistance to the antibiotic. In this way, when really needed and even if given in standard doses, the antibiotic will not have the desired effect. Prevention instead is carried out by the project "DEFLeCT". It is nowadays obvious, and supported by many studies [11], [12], [13], [14] that the cure and survival probability to cancer is much higher if the disease is diagnosed in early stage, when it is still small and limited to a local zone of the body. In this case, a biosensor could be helpful in making the procedure non-invasive for the patient and contemporarily, saving time and complexity for the medical staff.

1.2 From inorganic to organic FET

Often the electronic biosensors are associated with the concept of Field Effect Transistors, already very well-known in the world of electronic devices since the '70s, even if the invention goes back to 1960 [15]. Metal-Oxide-Semiconductor Field Effect Transistor (MOSFET) has been the most successful FET designed for years, and nowadays all the electronics is based on this technology or its derivations. A MOSFET is a device essentially made up by three terminals (or four including the bulk): gate, source and drain (see *Fig. 1.1.1*) As stated by the name itself, this device is composed by stacking up three different layers: a semiconductor, which in the vast majority of cases it is Si; an oxide layer, SiO_2; and a metal contact which works as the gate of the device. Being a semiconductor, Si needs implantation of impurities in order to achieve an effective conduction of charges. MOSFETs can be: nMOS, where acceptor" impurities, like Boron or Gallium are implanted to achieve a p-type semiconductor. Donors are pentavalent impurities, contributing to the conduction donating free electrons. pMOS, where "donor" impurities like Arsenic or Phosphorus, are implanted to achieve a n-type semiconductor. Acceptors are trivalent impurities, contributing to the conduction, creating holes. Then, an opposite doping is performed locally, below source and drain contacts, to create two highly doped regions, respectively n+ and p+. Regardless the device type, when an external field is applied at the gate electrode, a conductive channel is obtained in the semiconductor, connecting source and drain and allowing electrical conduction. For an nMOS the majority charge carriers in the channel are electrons; in a pMOS the majority charge carriers are holes.

When in strong inversion conditions, the MOSFET (*Fig. 1.1*) behaves like a variable resistor in which the intensity of the electric field (and consequently the applied voltage) establishes the conduction of charges.
Having control over the electric field, by controlling the external voltage applied to the transistor terminals allows for the modulation of the channel extension. Consequently, also the current flowing through it can be modulated up to saturation, the region where the current becomes independent from variations of voltages between source and drain contacts.

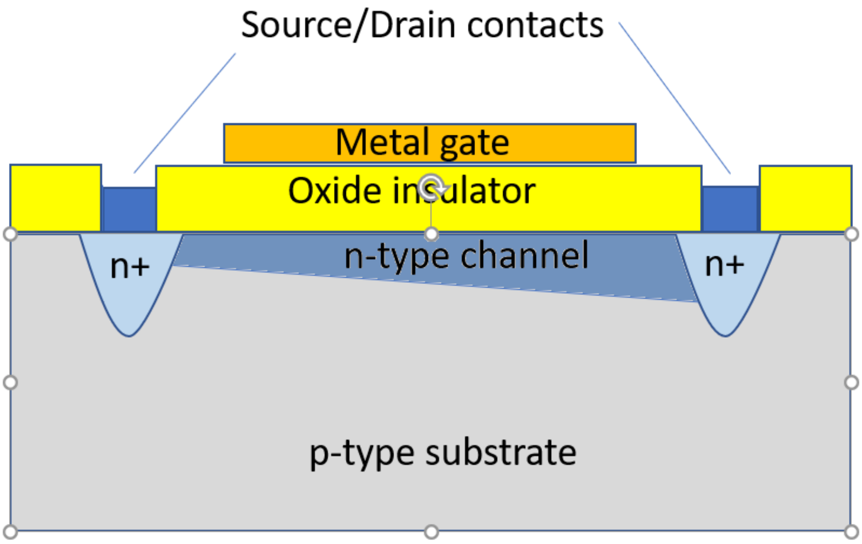

Fig. 1.1: Typical MOSFET configuration for a nMOS. MOSFETs usually work in inversion region, hence in this case the majority carriers flowing through the channel (or inversion layer) are electrons. pMOS has opposite channel polarity due to opposite substrate and S/D implantations and substrate as well.

The introduction of ISFET in 1972, made up the first step in moving towards FET-based biosensors. An ISFET is basically a MOSFET, where the metal gate has been replaced by a permeable membrane (whose function is carried out by an high-k dielectric layer in the last years, similarly to what is happening in MOSFET technology), and an electrolyte where a reference electrode is immerged (see *Fig.* 1.2) [7]. One of the main difference between an ISFET and a classic MOSFET is the threshold voltage V_{th}: while in MOS transistors it depends on many factors, like oxide thickness, temperature, body effect, for an ISFET the threshold voltage has a strong dependence from the pH of the electrolyte solution. [16]

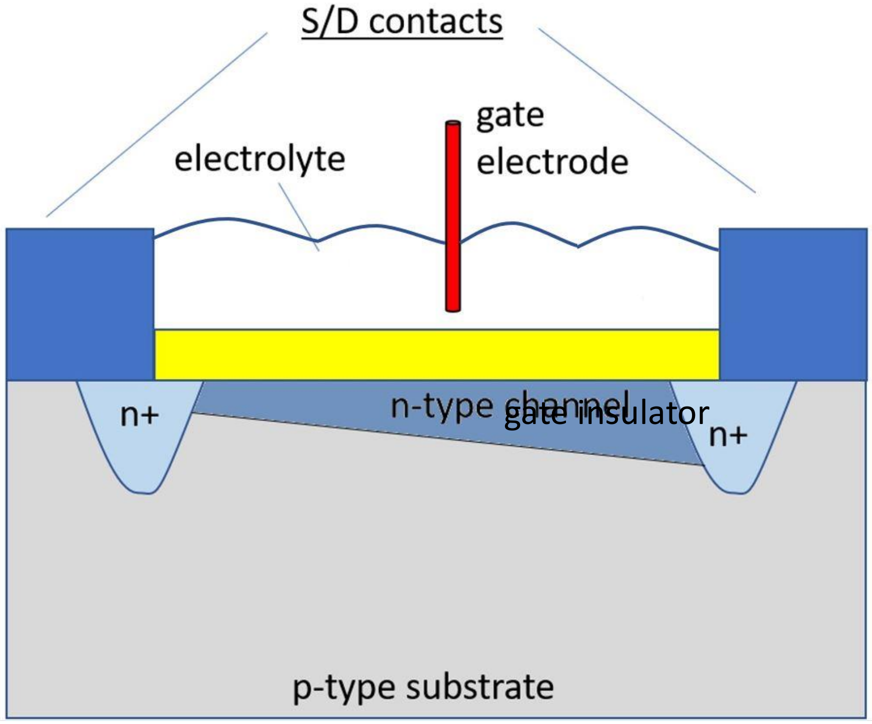

Fig. 1.2: Typical ISFET configuration

The ion sensitive transistor was considered the first Bio-FET or FET-based sensor ever produced. Since then, their development never stopped, thanks to their straightforward manner to physically convert the biochemical input into an electric signal at the output. At the same time ISFETs are quite simple to integrate in the conventional cleanroom processes. The neatness of the process goes in contrast with its expensiveness, and since costs, practically make up the most important parameter for companies' decisions, emerging Organic Thin Film Transistors (OTFT) showed a promising and cheaper alternative for the future. An OTFT is a transistor, where the active material is of organic nature, exploiting the architecture of a conventional TFT, presented by Weimar in 1962 [17]. The first OTFT appeared in the late 80s: in 1986, a team of researchers at Mitsubishi Electric came up with the idea of an OTFT which already used a conjugated polymer, the thiophene [18]. OTFT is quite a generic term to indicate a large family of devices, based on an organic component. They share this feature with other devices, and among the most successful, Organic Light Emitting Diode (OLEDs) and OFETs (Organic Field Effect Transistors) are included. The first ones are nowadays growing strongly in the screen market (for televisions, smartphones, etc…), in such a way that they are replacing in many applications the standard LCD displays [19]. The second ones generally work in accumulation mode, differently from MOSFETs [20]. They are finding space in either the sensors and biosensors world, with numerous applications such as lactate detection [21] (also integrated in flexible electronics [22]), gas sensors [23], detector of chemicals in either freshwater and seawater [24], pressure sensors for health-care [25], biomonitoring [26], DNA detection [27].

In spite of their poor performances when compared with the dominating silicon-based technology, they become a valuable option for many reasons: to begin with, the organic material has got weak molecular interactions. As a consequence, the processing temperature can be kept low with respect to relatively higher processing temperature of the inorganic world. For this reason, substrates could be replaced by flexible and plastic ones. Also, they allow to fabricate devices over relatively large areas, without employing vacuum processes but only coating or printing technology [28].

OFETs can be fabricated with different configurations depending on the electrodes’ arrangement. Source and drain contacts can be grown after the organic material is deposited, hence above the film in a “top contact configuration”, or before the deposition of the organic material, and so taking the name of “bottom contact configuration”. Both configurations include a bottom gate configuration; another possibility would be to adopt a top gate configuration in combination with bottom contacts. The three configurations are shown in *Fig. 1.3*

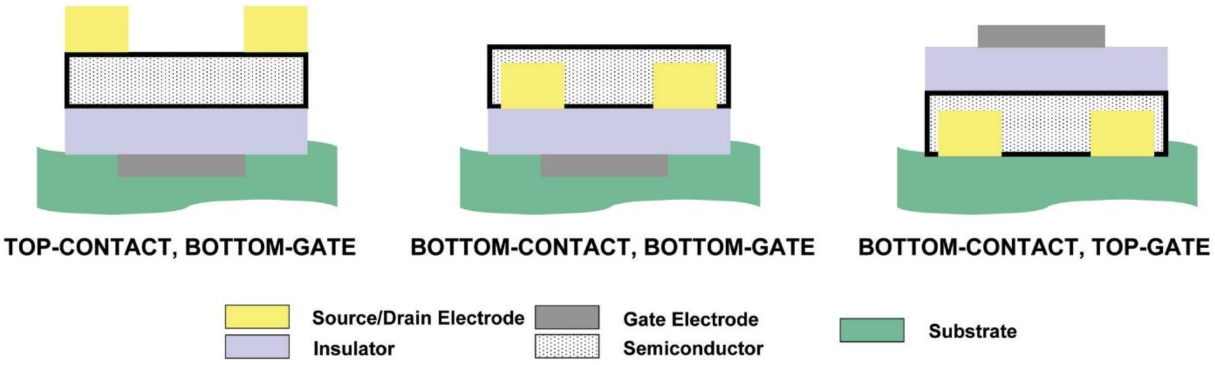

Fig. 1.3: The three possible configurations for OFETs [20]

1.3 EGOFETs

EGOFETs are three terminal devices: source, drain and gate are the three electrodes. Although EGOFETs are included in the OFETs category, there are differences among the two: the gate is not in direct contact with the semiconductor, but it is immerged in an electrolyte, and in turn the electrolytic solution is in contact with the organic material. In other words, EGOFETs combine the major characteristics from OFETs and ISFETs. From the OFETs it is the exploitation of an organic material as semi- conductive component, with the possibility to approach many bio-related applications thanks to its functionalization; from the ISFETs the fact that the organic material is directly exposed to the electrolyte, removing the metallic layer (see *Fig. 1.4)*. Also, the working mechanism resembles the ISFETs one, because of the creation of two electrical double layers: one at the interface gate/electrolyte, and the other at the interface, polymer/electrolyte.

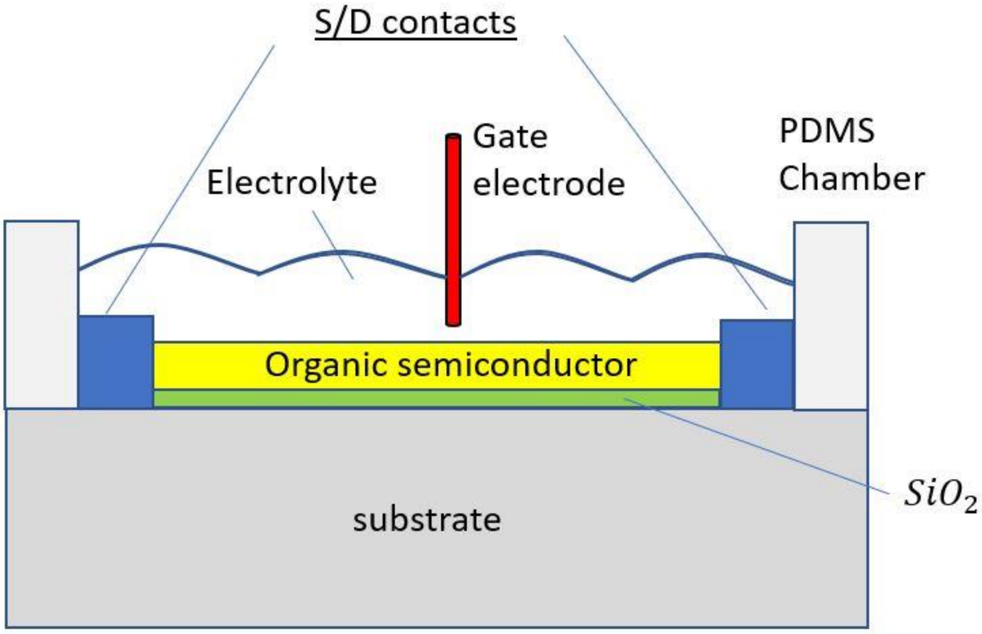

Fig. 1.4: cross section of a typical EGOFET depicted as a synthesis between an OFET (electrolyte acts as insulator) and an ISFET (gate in contact with the electrolytic solution)

The electrolyte media acts effectively as a gate dielectric, causing the lowering of the operational voltages, down to 1 V and below, thanks to electrical double layer (EDL) capacitance (see *Chapter 1.3.3*), that increases the capacitance of this devices up to tens of $\mu F/cm^2$, which results averagely, in at least 2-3 orders of magnitude higher than that of inorganic technology with standard dielectrics [29].

EGOFETs have recently been subject of many studies when employed as biosensors [30], [31], ; the reasons for such an interest are several: they are solution processable, which makes them cheap and suitable for integration on flexible substrates, and at the same time to be based on a label-free detection method**.** This device has shown high sensitivity, with a detection limit of $2.4 \cdot 10^3$ molecules in 100 μL of solution [30], which is a key advantage for a biosensor that has to detect the smallest quantities of analytes. Moreover, they are capable to biorecognise a wide range of analytes [32]. Last but not least, they are bio-compatible, and versatile towards functionalization, whether it is applied at gate electrode or at the organic material.

1.3.1 Organic semiconductors

Organic materials do not include exclusively semiconductors, but also insulators and conductors. Their behaviour is strongly related to the electronic state that carbon atoms assume in the chemical bonds, in fact, carbon atoms made up a consistent part of the organic molecules' backbone structure. Organic semiconductors have a key feature which makes them suitable for electronic applications: the conjugation. An organic material is conjugated when the backbone chain is built up by alternating double and single covalent bond. [33].

There are two types of organic materials that are exploited for organic electronics: conjugated small molecules and conjugated polymers. The formers are mostly reported on photovoltaics applications. In particular, in small molecules, carriers do not flow among terminals, but they hop from molecule to molecule. This process is hampered by the electron-to-electron repulsion and by poor HOMO overlaps. In fact, due to the herringbone structure molecules arrange themselves, charge carrier mobilities are limited. Moreover, mobility reduces when the molecules “lose the conjugation”, that occurs both in liquid phase because of photo-dimerization and in solid phase because of photo-oxidation [34]. It was thanks to the development of a better and deeper understanding of chemistry that it was possible to improve from low mobility values around $10^{-6}\ cm^2/V \cdot s$ to values of 6-7 higher magnitudes, and anyways to values that surpass amorphous silicon TFT [35]. Polymers have the advantage of flexibility regarding the deposition technique and processability: spin coating, inkjet printing and other low-cost methods are all suitable for this kind of semiconductor. Polymers are basically macromolecules, or high weight molecules, made up by several molecular groups chain-bonded throughout a covalent bonding.

To understand how to properly exploit a polymer as a semiconductor, it is necessary to introduce the concepts of Highest Occupied Molecular Orbital (HOMO), Lowest Unoccupied Molecular Orbital (LUMO) and molecular orbitals. Orbitals are wave functions describing the density of probability to find electrons around an atom; when two atoms interact, or simply their distance is small, their orbitals superimpose themselves, forming bonding or antibonding molecular orbital. A bonding molecular orbital occurs when the electrons are distributed in between the two atoms in the lower energy bands, hence stabilizing the orbital; an antibonding molecular orbital instead is obtained when electrons among the atoms are few, resulting in a greater repulsion forces between the two, hence increasing the energy of the system and destabilizing the orbital. Bonding molecular orbitals are divided into sigma (σ-), pi (π-) and delta (δ-). The first occurs by frontal overlapping of molecular orbitals. The second occurs due to lateral overlapping of two orbitals (commonly with p symmetry). The third occurs by overlapping of four lobes (typical with d symmetry).

The electronic state describes the electron arrangement within an atom. An atom could be at ground state, which represent the lowest energy configuration, or at the excited state which is a configuration with any level of energy higher than the ground state. In *Table 1,* are defined the principles to represent an electronic configuration. The three types of s and p orbitals hybridization are:

- sp hybridization is typical of situations where an atom is surrounded by two groups of electrons. It includes one p orbital and one s orbital resulting in two sp orbitals oriented with an angle of 180°
- sp^2 hybridization is typical of semiconducting and conducting polymers: three valence electron orbitals make up a linear structure with separation angles of 120°
- sp^3 hybridization is typical of insulating polymers: four valence electron orbitals take tetrahedrical shape, where the angle among the lobes is 109.5°

At electronic ground state, the π orbital is filled by electrons while the corresponding antibonding π^* orbital is depleted. In this way the double bond creates a band gap among the two in the range of $[1;\ 4]$ eV which is characteristic of semiconductors.

SHELL	**SUBSHELL**	**MAXIMUM NUMBER OF ELECTRONS IN THE SUBSHELL (SHELL)**
K	1s	2 (2)
L	2s	2 (8)
	2p	6 (8)
M	3s	2 (18)
	3p	6 (18)
	3d	10 (18)
N	4s	2 (32)
	4p	6 (32)
	4d	10 (32)
	4f	14 (32)

Table 1: Organization of electron orbits in shell and subshells and their maximum number allowed. K is the inner shell, N the most external one.

In the world of standard transistors implantation of impurities is the dominant technology. In the polymers field, it is possible to distinguish various doping techniques: charge transfer from a dopant to the polymer; electrical polarisation of the OSC; injection of charges, either unipolar or bipolar, to the OSC through one or two electrodes; photogeneration of electron–hole exposed to a source light; last but not least, ion implantation [36].

The successful development of OLEDs, that offered a better understanding of OSCs. These materials were used considering their p-type or n-type behaviour according to intrinsic properties like low ionization potential for the former and high electron affinity for the latter [37]. The majority of OSC studied showed intrinsic p-type behaviour. Only in the last years an effective way to dope the polymer, with the so-called molecular doping has been developed, with the introduction of proper donors and acceptors.

In the following, are described one of major conjugated polymer Poly(3-hexylthiophene) (P3HT), and one of its derivatives, subject of this thesis, P3CPenT.

1.3.1.1 P3HT

P3HT belongs to the polythiophenes family. Thiophenes are a five atoms ring compound, as it can be seen in *Fig. 1.5(c)*, where the position 1- is occupied by a sulfur atom, while in all the other position there is a C-H bond; thiophenes can be polymerized by acid materials or catalyst. The positions 2- and 5- of the polythiophene monomer are the ones in charge to link the molecule with the others and according to the coupling of these links, it is possible to distinguish three different regioisomeric configurations due to polymerization: 5-5′, called tail-to-tail; 2-5′, called head-to-tail; 2-2′, called head-to-head. The behaviour to assume only one configuration along the chain is measured in percentage and it is called regioregularity. Regioregularity is referred to the head-to-tail configuration, so that, ideally a 100% regioregular head-to-tail polymer offers the lowest energy configuration, hence the best optoelectronic properties in terms of charge transfer and energy adsorption (see *Fig. 1.5(a)-(b)*) [38]. Unsubstituted polythiophenes though are difficult to be processed at industrial level, especially for its insolubility with all solvents except for some As mixtures (i.e., tetrahydrofuran) and for this reason the hydrogen position 3- is replaced with long flexible chains. Among the various polythiophene 3-substituted, when a hexyl (C_6H_{13}) side chain is attached at each monomer element, poly(3-hexylthiophene-2,5-diyl) is the result. Commonly known as P3HT, it is a derivative of Poly(3-alkylthiophenes) (P3ATs). Among derivatives of P3AT are also included: poly(3-butylthiophene) (P3BT), poly(3-octylthiophene) (P3OT) and poly(3-decylthiophene) (P3DT).

P3HT is a very well-known conjugated polymer and widely used for solar cells structures, but also as OSC in TFT applications [39]. Its blends with PCBM, referred to as P3HT:PCBM; it is arguably the most studied and researched topic in the new millennium for bulk hetero-junction solar cells [40]. P3HT perfectly fits processability requirements because of increased solubility toward common solvents (i.e., toluene, chlorobenzene, di-chlorobenzene, chloroform), showing noticeable optoelectronics properties; the term at the end of the name stands as indicator of polydispersity.

Many semiconducting conjugated polymers employed in OFETs, show complex microcrystalline domains arrangement, though ordered. This morphological property makes charge carriers transport difficult, hence very low mobilities are common, in the order of $10^{-5}\ cm^2/V \cdot s$. OFETs employing P3HT as OSC have shown relatively high carrier mobility instead, up to $0.1\ cm^2/V \cdot s$ [29]. This is possible because of a different morphological structure that this conjugated polymer shows with respect to many others: by self-assembly, P3HT forms a lamellae structure, where the backbone sheets can be arranged vertically or in parallel depending on the process and having consequences on other factors such as charge carriers mobility.

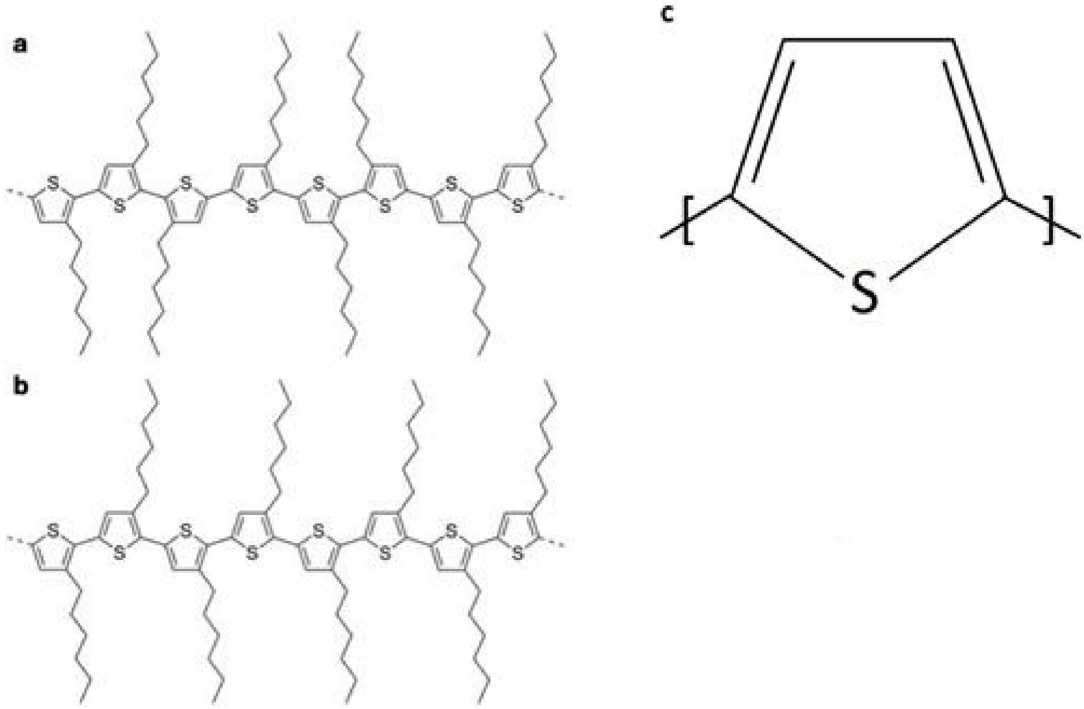

Fig. 1.5: (a) regioregular and (b) regiorandom P3HT; [85] (c) representation of the thiophene monomer; the sulphur atom occupies position 1-, and from there, turning anti-clockwise, carbon atoms occupy positions from 2- to 5-

1.3.1.2 P3CPenT

Poly[3-(carboxyalkyl)thiophene-2,5-diyl] (P3CAT) are conjugated polymers introduced as p-type OSC. The morphology of the polymer is made up by the standard thiophene monomer substituted at position 3- with carboxyalkyl group $-(CH_2)_xCOOH$. The x value is included in the range [3; 6] and the resulting polymers are from the longest to the shortest sidechains: poly[3-(6-carboxyhexyl)thiophene-2,5-diyl], poly[3-(5-carboxypentyl)-thiophene-2,5-diyl], poly[3-(4-carboxybutyl)-thiophene-2,5-diyl], poly[3-(3-carboxypropyl) thiophene-2,5-diyl], or respectively abbreviated as P3CHexT, P3CPenT, P3CButT, P3CProT (see *Fig*. 1.6). The increasing of x defines an increasing distance among the crystalline planes, with linear dependence. The x range for P3CATs is small enough to ensure that acceptable values of mobility are achieved: side chains longer than 12 substituents might move the mobility down to values not suitable for OTFT applications as a result of the side chain predominance of the film matrix; on the contrary, side chains shorter than 3 substituents, would compromise the solubility and film growth [41].

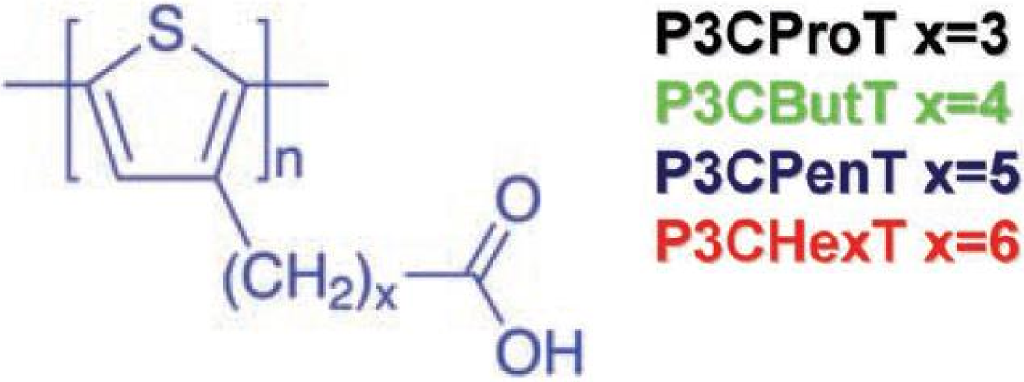

Fig. 1.6: P3CATs are thiophenes substituted with carboxyalkyl $(CH_2)_x$ *side chains, where the length x identifies four different materials of the same series [43]*

Among the carboxylic acid derivatives, the one that has given the most promising results is P3CPenT. Its specific applications available in literature are more focused in the organic photovoltaics sector. Nonetheless, compared to the other members of the P3CAT family, P3CPenT highlights higher hole mobility ($10^{-3} - 10^{-4}\ cm^2/V \cdot s$) [42], probably thanks to a larger crystalline structure , and it's important to underline that this result remains unchanged regardless the solvent, or at least whether the chosen solvent is pyridine, DMSO or DMF [43] [44]. Results reported for P3CPenT values of HOMO and LUMO energy, in magnitude, respectively of 5.13 eV and 3.20 eV, for a bandgap of 1.93 eV [43].

1.3.2 Figures of merit

Figures of merit are used to give a complete analysis about the different devices at different conditions. The ON current (I_{ON}) is the current between source and drain when, that is when the applied voltage to the gate is $V_{GS} = -0.5V$ and the device is in saturation, that is when the drain voltage is $V_{DS} > (V_G - V_{th})$, with $|V_G| > |V_{th}|$. Off current (I_{OFF}) is the current flowing through source and drain in the OFET when no voltage is applied among them ($V_{GS} = 0\,V$) or anyways, when $V_{DS} < (V_G - V_{th})$ and the device can be considered in the OFF state. Ideally, it would be zero, meaning that the OFET is behaving as a perfect switch. I_{ON}/I_{OFF} is the ratio among the two currents. It is used as a measure to evaluate the performance (more related to the nominator) and the power consumption (related to the denominator) of a device. Typical values of the I_{ON}/I_{OFF} ratio for EGOFETs are around 10^3 [45].

The figure of merit that most is related to this concept of on/off is, by definition, the threshold voltage (V_{th}). This is the minimum level of voltage drop between gate-source that must be applied in a transistor, to be able to create a conductive channel.

The equation describing V_{th} is:

$$\mathrm{V_{th}} = \mathrm{V_{TO}} + \gamma \cdot \left(\sqrt{|\mathrm{V_{SB}} + 2\Phi_\mathrm{F}|} - \sqrt{|2\Phi_\mathrm{F}|}\right) \tag{1.1}$$

where V_{TO} is the threshold voltage neglecting body bias, V_{SB} is the voltage source to body, $2\Phi_F$ is the surface potential and γ is the body effect.

Vth can be extrapolated in many ways. ELR (Extrapolation in the Linear Region) is one of the most common, but it carries with it uncertainties related to and drain parasitic capacitances and mobility degradation [46].

In this work, threshold voltage is extrapolated from the linear fit of $\sqrt{Ids}\ vs.\ Vgs$ in the saturation region where $Ids = \frac{1}{2}\,\mu\, Cg\,\frac{W}{L}\,(Vg\ - Vth)^2$: the intercept with the voltage axis of the prolongation as a straight line of the linear part of the curve is the Vth, as *Fig. 1.7*: Vth extrapolation with linear fit of a transfer curve in the linear region shows. [47]

Transconductance (g_m) defines how fast the drain current I_D changes for infinitesimally small gate voltage V_G variations, while the voltage from drain to source V_{DS} is held constant. The higher the transconductance, the better conductivity response per unit of biomolecule charge excitation. Therefore,

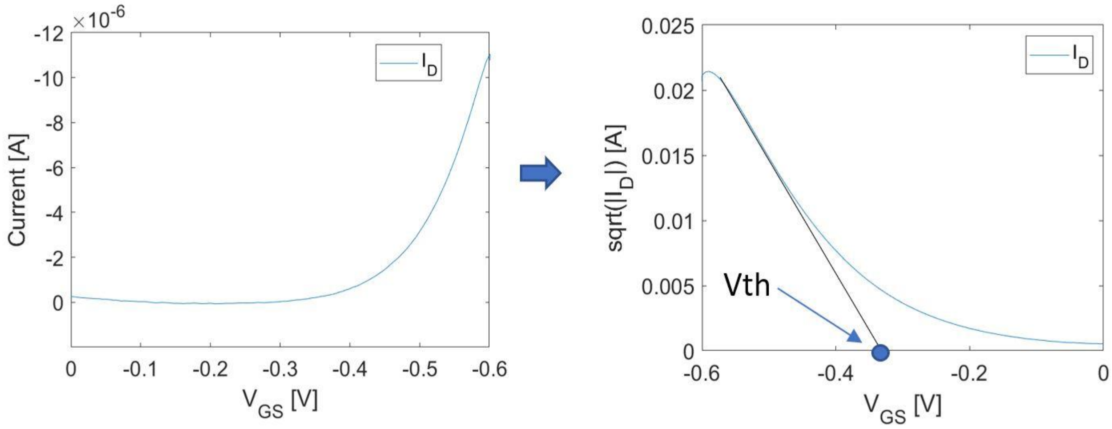

Fig. 1.7: Vth extrapolation with linear fit of a transfer curve in the linear region

transconductance is positively connected with the device sensitivity and can be considered one of the key parameters for sensing applications [48].

Reported values for EGOFETs are in the range of tens of μS [47], [49], It is calculated directly from:

$$gm_{max} = max\left(\frac{\partial I_{DS}}{\partial V_{GS}}\right) \tag{1.2}$$

According to Melzer et al. [49] two are the main parameters that indirectly influence the transconductance: the Helmoltz layer capacitance (discussed in *Chapter 1.3.3*) and the low field mobility (μ).

Mobility is an important parameter, expressing how fast holes or electrons can move in a semiconductor, or broadly speaking in a solid material, when an electric field is applied to it. Its definition comes as a proportionality function between the drift velocity v_d and the electric field E:

$$v_d = \mu \cdot E \tag{1.3}$$

In order to extract mobility from the acquired data, one should consider that the most robust method might change from one application to another. In particular, the extraction of charge carrier's mobility for OFETs has led to inflation of the extracted values, reportedly for several reasons [50]:

1. Linear and saturation regime mobilities mismatch due to large state delocalisation, which lead to a dependence from the applied field.
2. Underestimation of the double layer capacitance, due to trapped charges
3. Contact resistance, which might boost the mobility (graphically, steeper current curves) at very low or high potentials.

Mobility is extracted from the linear fit of output curves, as in *Fig. 1.8*, particularly from the slope of the fit in the linear region where:

$$Ids = \mu\, Cg\, \frac{W}{L}(Vgs - Vth)Vds \qquad (1.4)$$

for $V_{ds} \ll V_G - V_{th}$

while for the saturation regime it is valid the well-known current equation:

$$Ids = \frac{1}{2}\mu\, Cg\, \frac{W}{L}(Vgs - Vth)^{2} \qquad (1.5)$$

for $V_{ds} > V_G - V_{th}$

This model is verified when assuming the gradual channel approximation, that assumes a gradual voltage drop along the channel, and that mobility does not depend on charge carriers concentration (semiconductor bandgap is "states-free") [51].

Since mobility is mathematically related to other figures of merit, from *(1.4)* through the inverse formula:

$$\mu = \frac{Ids}{Cg\,\frac{W}{L}(Vgs - Vth)Vds}$$

it will be necessary, first the extraction of the unknown parameters $Cg, Vth,$ then the ratio $\frac{Ids}{Vds}$ is extracted from the linear fit of the linear part of the output curves, as in *Fig. 1.8.*

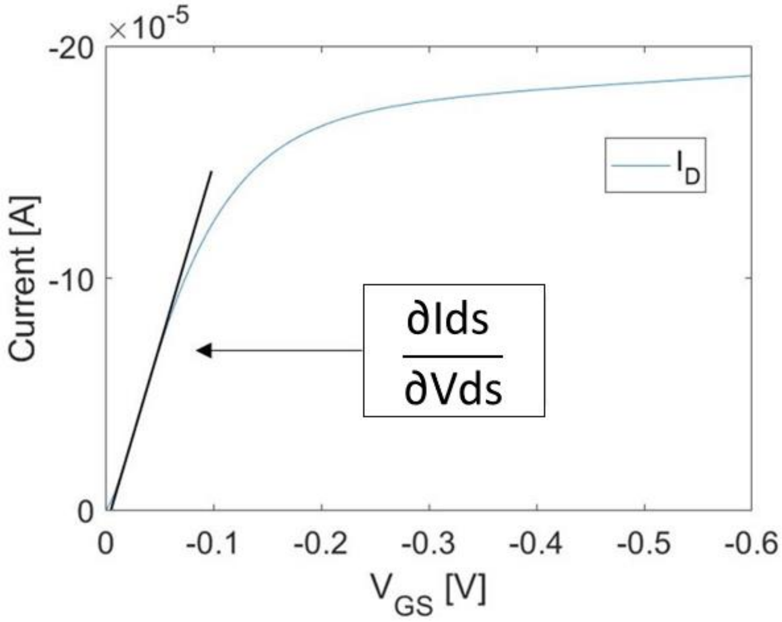

Fig. 1.8: The coefficent to extract the mobility is obtained by fitting the linear part of the output characteristic.

1.3.3 Working principle: the electrical double layer

The working principle of an EGOFET is strictly connected to its characteristic feature, which is the electrolyte. EGOFETs are biosensors developed for carrying out detection of analytes in an in-liquid environment. The liquid could be any kind of body-biological fluid (blood included), hence working in electrolyte solutions offers a good starting model thanks to the presence of ions. Fixing the potential on the gate and between source and drain, ions re-arrange within the electrolyte. This, added to differences in electron affinity, have the effect of polarisation on the gate itself, creating a so-called electrical double layer (EDL). The arrangement of charges is such that two EDL arise: one at the gate electrode-electrolyte interface, due to the polarisation. The other EDL right at the interface between the polymer and electrolyte, which have an impact on the semiconductor surface as well.

The first consistent formulation of the electric double layer was given by Gouy-Chapman model, which gives the name to Gouy-Chapman layer (also called diffuse layer). This layer forms in the electrolyte, in proximity of the electrode. The charges that contribute into the electrolyte are large-radius ions. A finite width layer of those, not only cannot stop the diffusion of the charges from the electrode but also causes a potential drop within the diffuse layer that is modelisable with the Poisson-Boltzmann equation:

$$\nabla^2\Psi = \frac{\delta^2\Psi}{\delta x^2} + \frac{\delta^2\Psi}{\delta y^2} + \frac{\delta^2\Psi}{\delta z^2} = \frac{\varrho}{\varepsilon_r\varepsilon_0} \tag{1.6}$$

Where Ψ is the electric potential, ϱ is the charge density in C/m^3, ε_r is the dielectric constant of the solvent and ε_0 is the permittivity in free space.

The Gouy-Chapman model, however, does not describe perfectly the electrical double layer: it was noticed an overestimation on the interface charge, hence on the double layer capacitance estimation [52].

The Stern formulation of Gouy-Chapman model added the incapability of ions to approach the surface closer that their own radius, so the closest distance is what is called the outer Helmholtz plane (OHP): a free of charge layer will give rise to a constant capacitance, the Stern capacitance.

Gouy-Champan-Stern (GCS) model is the most used description for the EDL. This model divides the interface in two layers: Stern layer and the diffuse layer. Stern layer is the layer closer to the surface and it is made up by specifically adsorbing ions, which are ions where can be distinguished two effects. One is Coulomb interactions act through the attraction-repulsion principle: when ions attach to a particle it changes its potential and repulse all the same sign ions. The other force is rather complex, and in this work will be assumed it is just a combination of different forces due to nature of ions, nature of electrolyte and other interfacial species. The diffuse layer is populated by indifferent absorbing ions instead, which are ions showing no other forces than attraction-repulsion (simple and double hydrogen bondings or Van der Walls forces) [53], [54].

The most important difference between these two layers is that the ions of the former are fixed, while for the latter they are free to move.

In a first approximation, the only contribution taken into account is the ion size. The Stern layer is closest layer to the interface. It is made up by a layer of ions of opposite polarity to the surface.

A differential capacitance can be defined:

$$C_1 = \frac{\partial \sigma^o}{\partial(\psi^o - \psi^d)} = -\frac{\partial \sigma^d}{\partial(\psi^o - \psi^d)} \tag{1.6}$$

Where σ^o is the surface charge density, ψ^o the corresponding potential, σ^d is the charge in the diffuse region and ψ^d the corresponding potential. The capacitance of the double layer is simply the series of the tw capacitances:

$$\frac{1}{C} = \frac{1}{C^i} + \frac{1}{C^d} \tag{1.7}$$

If not only the size of ions, but also specific adsorption is considered, the concept of IHP has to be introduced. Indeed, if the specific adsorption is the phenomenon that bounds the counter-charge to the OSC by non-electrostatic forces, so an ion interacting non-electrostatically has to approach the surface within a certain distance of adsorption which is the IHP itself [53].

At this point the differential capacitances to be defined are two, one for each layer:

$$C_2^{IHP} = \frac{\partial \sigma^o}{\partial(\psi^o - \psi^i)} \tag{1.8}$$

$$C_2^{OHP} = \frac{\partial(\sigma^o + \sigma^i)}{\partial(\psi^i - \psi^d)} = -\frac{\partial \sigma^o}{\partial(\psi^i - \psi^d)} \tag{1.9}$$

Where σ^i and ψ^i are respectively are the specifically adsorbed charge density and corresponding potential.

In this case, the three capacitances cannot be considered in series: by calling K the integral capacitance, result of the integration of the differential capacitance, we had that in the first case also the integral capacitance could be considered as the series:

$$\frac{1}{K} = \frac{1}{K^i} + \frac{1}{K^d} \tag{1.10}$$

Since

$$K = \frac{1}{\psi^0 - \psi^d} \int_0^{\psi^0 - \psi^d} C \ \partial(\psi^o - \psi^d) \tag{1.11}$$

While in this second case it gives back:

$$\psi^0 - \psi^d = \frac{\sigma^0}{K_2^{IHP}} + \frac{\sigma^d}{K_2^{OHP}} \tag{1.12}$$

Which results in:

$$\frac{1}{C} = \frac{1}{C_2^{IHP}} - \left(\frac{1}{C_2^{OHP}} + \frac{1}{C^d} \right) \frac{\partial \sigma^d}{\partial \sigma^o} \tag{1.13}$$

Finally, as last assumption, by supposing that the specific adsorption is superequivalent, meaning negative charge in the IHP surpass the surface charge, leading to irregular coagulation: while the surface charge gets bigger and bigger, the diffuse charge can be re-stabilized at higher solution concentration *[53]*. The three electrical double layer models are shown in

Fig. 1.9: Charges arrangement in an electrical double layer taking into account a) ion size b) specifical adsorption c) superequivalent

Fig. 1.9

An important remark to add to this discussion concerns ψ^i, which is not easily evaluable. Two of the simplest approximation that can be done are:

1) Ignoring the change of slope at the inner-outer Helmholtz and assume: $\psi^i = \frac{[(\psi^i - \psi^d)\psi^o + (\psi^o - \psi^i)\psi^d]}{d}$
   where d is the distance from the surface
2) Assuming that specific adsorption occurs only at OHP interface, in this way $\psi^i = \psi^d$

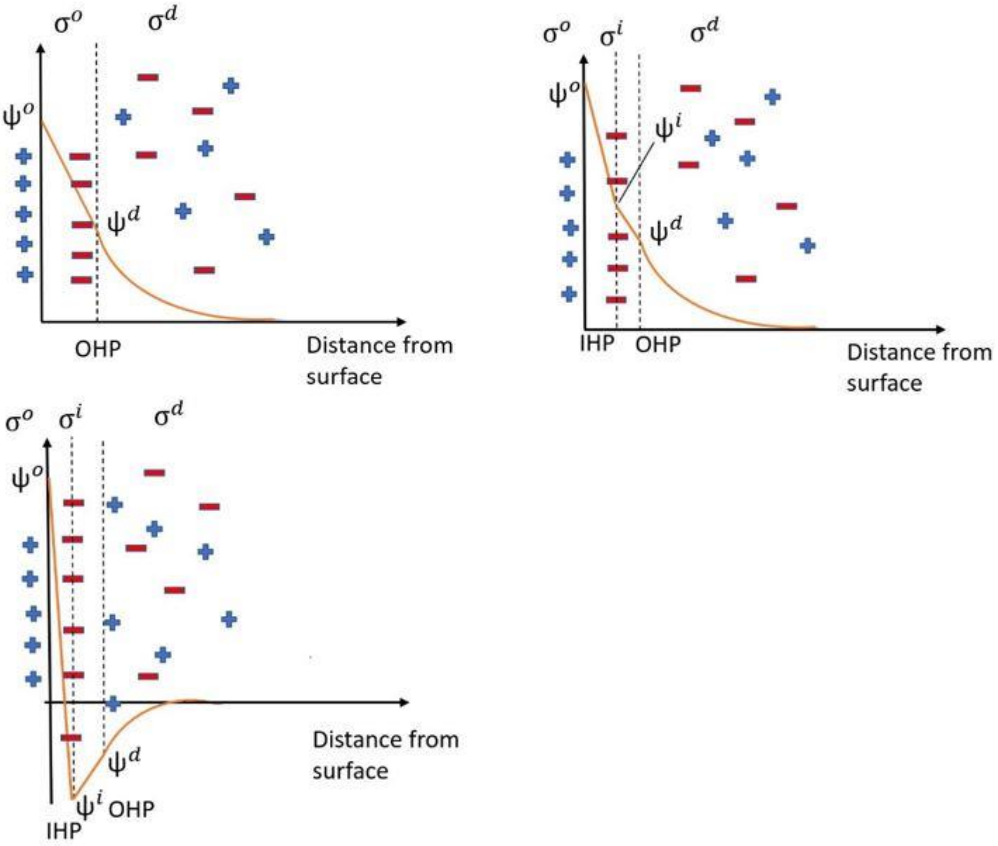

Fig. 1.9: Charges arrangement in an electrical double layer taking into account a) ion size b) specifical adsorption c) superequivalent adsorption.

The double layer capacitance can also be connected to the Debye length. The definition of Debye length is given in plasma, electrolyte or in a semiconductor environment as the distance over which ions and electrons are capable to shield the electric field. In other words, is the distance over which charge separation occurs significantly. Debye length is introduced in this context as a measure of the EDL thickness. According to the environment, there are more than one analytical representation of it. In an electrolyte solution, Debye length is denoted with the symbol k or $\frac{1}{k}$ and expressed by:

$$k^{-1} = \sqrt{\frac{\varepsilon_r \varepsilon_0 k_B T}{2\ x\ 10^3 N_A e^2 I}} \qquad (1.14)$$

Where ε_r and ε_0 are respectively the permittivity of the electrolyte, and the permittivity in free space, k_B is Boltzmann constant, T is the temperature, N_A is the Avogadro number, e is the elementary charge and finally I is the ionic strength.

It is clear the proportional dependence of the Debye length from the ionic strength of the electrolyte. For water at room temperature (20 °C), and substituting the constants in the equations, Debye length can be expressed only as function of the ionic strength:

$$k^{-1} = \frac{0.304}{\sqrt{I}}\ [nm] \qquad (1.15)$$

Where k^{-1} is expressed in nm if the ionic strength is expressed in M or mol/L.

The electrical double layer potential, it is referred to as zeta potential (ζ-potential), which in the most recent definition is "*the potential difference between the dispersion medium and the stationary layer of fluid attached to the particle*" [55]. Zeta potential is defined at the slipping plane, which the ideal plane separating IHP and OHP. Since, this model would be very complex to head, for sake of simplicity, charge density within the surface and IHP can be considered so low to be neglected, as well as for the region among the two Helmholtz planes, zeta potential can be considered the potential at the OHP and the EDL simplified in the Stern layer and diffuse layer separated by the OHP itself [56]. This simplification helps at least in three different ways: the equations of diffuse layer are simpler; errors coming from the neglection are actually low; OHP and slip plane match.

The most used technique to calculate ζ-potential is the micro-electrophoresis [57], where electrophoretic mobility u_E is converted into ζ-potential through Henry's equation:

$$u_E = \frac{2\,\varepsilon\,\zeta\,F(ka)}{3\eta} \qquad (1.16)$$

Where ε is the dielectric constant of the dispersant, $F(\kappa a)$ is the Henry function and η is the viscosity.

Smoluchowski equation can be considered a particular case of it [57], even if introduced before. Smoluchowski approach establishes a relation between Debye length and ζ-potential under two assumptions:

- Thin double layer model, which means the Debye length $\frac{1}{k}$ is much smaller than the charge carrier's radius a ($k \cdot a \ll 1$). This is valid for most of the aqueous systems that have a Debye length of few nanometres.
- Condition of a small Dukhin number ($Du \ll 1$), which neglects the contribute of the surface conductivity.

1.3.4 Polarizable and non-polarizable electrodes

Electrodes can be ideally classified in perfectly polarizable and non-polarizable electrodes. The formers are crossed by a displacement current and so the interface with the electrolyte can be modelled by a capacitor; the latters let current pass through very easily instead, and they can be modelled by a resistor.

In non-ideal cases, a third type of electrode can be distinguished from the two mentioned above, the so called partially polarizable electrodes. These electrodes are more complex to describe since they show different characteristics; an approximated model would be an RC circuit (see *Fig. 1.10*).

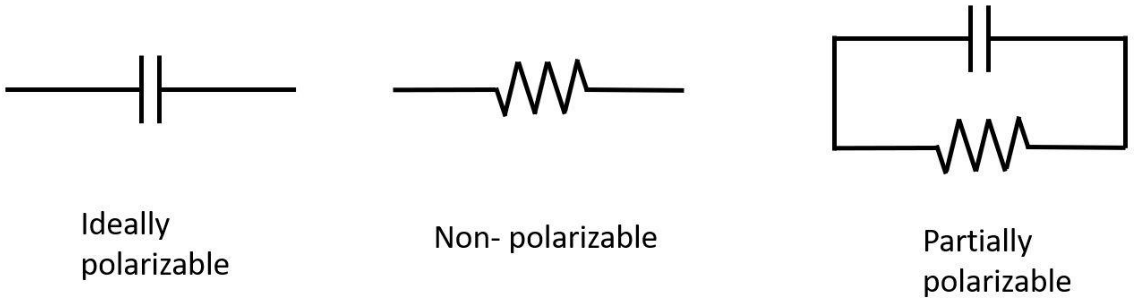

Fig. 1.10: The simplest modelisation of the three type of electrodes

When a metal comes in contact with an electrolyte, red-ox reactions cause a separation of net charges at their interface due to their chemical potentials. Unless an external force is applied, the charge at the interface, makes up an electric field that result in a constant electrostatic potential, called equilibrium potential (or half-cell potential when no current is passing through the interface). This cannot be measured with traditional methods for its own nature. However, it is possible to measure it with respect to a reference electrode like the circuit in *Fig. 1.11* depicts. Hydrogen electrodes has been chosen as reference for standard electrode potential (also referred to as SHE=Standard Hydrogen Electrode) [52].

To sum up, it is when an external field is applied that conduction is possible: if the potential applied is greater than the equilibrium potential, a part of it will match this potential, and the rest of it, the so-called overpotential will work for conduction. [58]

For this thesis two electrodes have been used as gate electrodes to test whether a polarizable electrode affect performance of EGOFETs with respect to a non-polarizable electrode. An Au electrode was used as polarizable electrode and an Ag/AgCl electrode was used as a non-polarizable one.

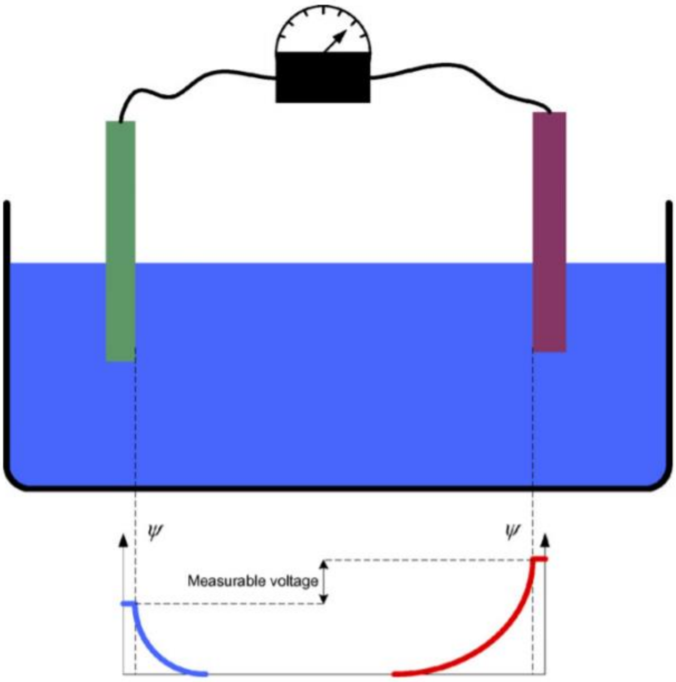

Fig. 1.11: Circuital configuration to measure the equilibrium potential [58]

Gold falls into the category of polarizable electrodes, which practically means that it exhibits such an high resistance that current is fully capacitive and by applying a voltage at the gate, it drops both across the electrolyte/OSC interface and at the electrode/electrolyte, correspondingly to their electrical double layer. On the other hand, the Ag/AgCl electrode can be assumed to be non-polarizable, which practically can be translated in a impedance so low to allow faradaic current to pass through, and whatever the applied potential is, the voltage drop will entirely occur at the electrolyte/semiconductor interface.

The Ag/AgCl electrode is made up by an AgCl coated Ag wire, immersed in a KCl saturated solution. The reversible reaction that takes place at the electrode is:

$$AgCl(s) + e^{-} \leftrightarrow Ag^{+}(s) + Cl^{-}(sat, d)$$

The standard reduction potential is $+0{,}222\ V$, while the potential referred to a hydrogen reference electrode is $+0{,}197\ V$.

2 Materials and methods

2.1 Instruments and measurement set-up

Error! Reference source not found. and *Fig. 2.2* show a block diagram and an electric scheme of the measurement instruments and devices connection. For the whole experience, it was used the MPI TS150-THz Probe System. A Keysight Technologies B2912A

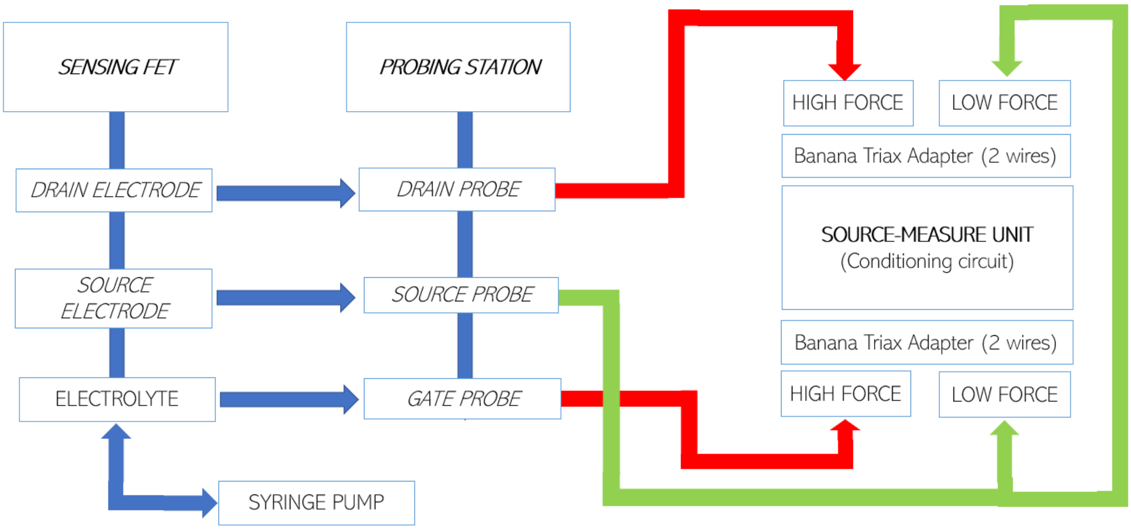

Fig. 2.1: Block diagram of the measurement system

Precision Source/Measure Unit was used to perform the measurement. It was driven via laptop (a SONY Vaio) through the proprietary Keysight software Benchvue, for all output and transfer characteristic measurements, while for chronoamperometry measurements Quick IV Measurement Software was employed instead.

At this experimental set-up (see *Fig. 2.3*) was added a NE-4000 Double Syringe Pump by New Era Pump Systems, Inc., charged with Hamilton syringes filled with the electrolyte at fixed concentration. The solution was sent at constant flow rate (typically 20 μl/min) into the microfluidic chamber (see *Fig. 2.5*), where an EGOFET sample was placed.

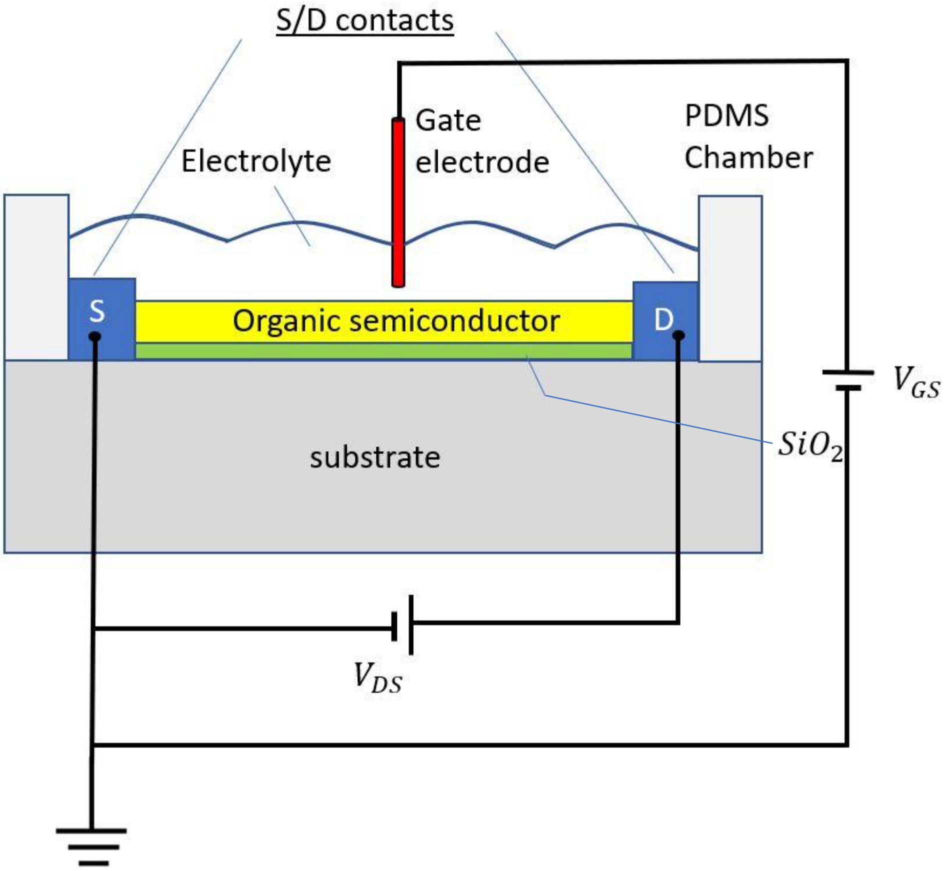

Fig. 2.2: Electrical connection scheme of the EGOFET

The whole equipment required for making the microfluidic system work is shown in *Fig. 2.4.*

The sample was contacted through micromanipulator probes and connected to the source-meter via triax cable.

Source terminal was kept at ground state and connected to both channels through the Low Force input of the triax adapter; drain contact is connected to the High Force input of channel one (CH1) and gate terminal is connected to the High Force input of channel two (CH2). The potentials V_{DS} and V_{GS} applied respectively to CH1 and CH2 are both referred to the source. The corresponding current is measured.

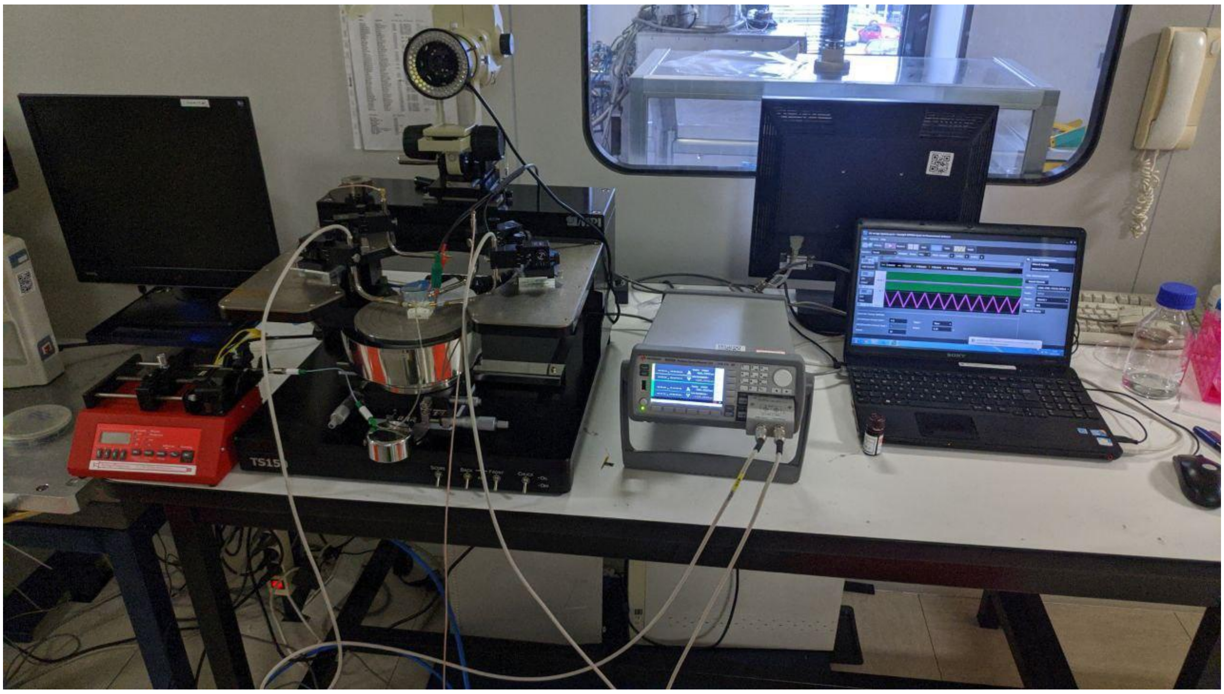

Fig. 2.3: Workstation composed by (from left to right): syringe pump, probe station, source meter, laptop.

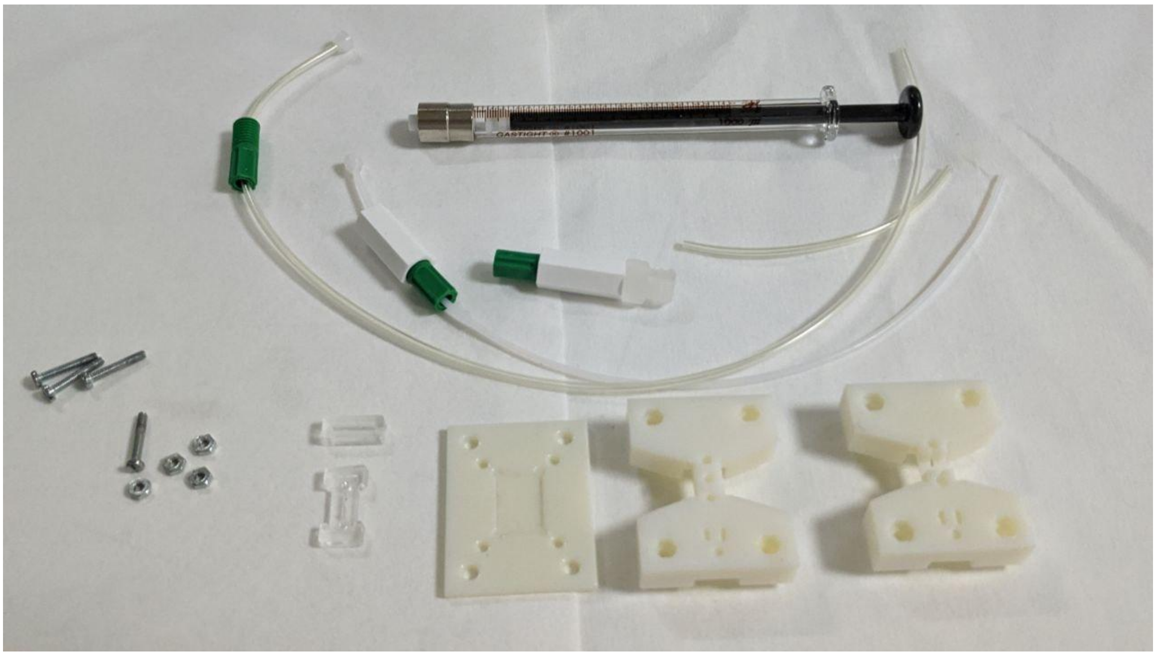

Fig. 2.4: Microfluidic equipment includes: mini screws and bolts, microfluidic tubes, Hamilton syringes, PDMS chamber (top and bottom), 3-D printed microfluidic device.

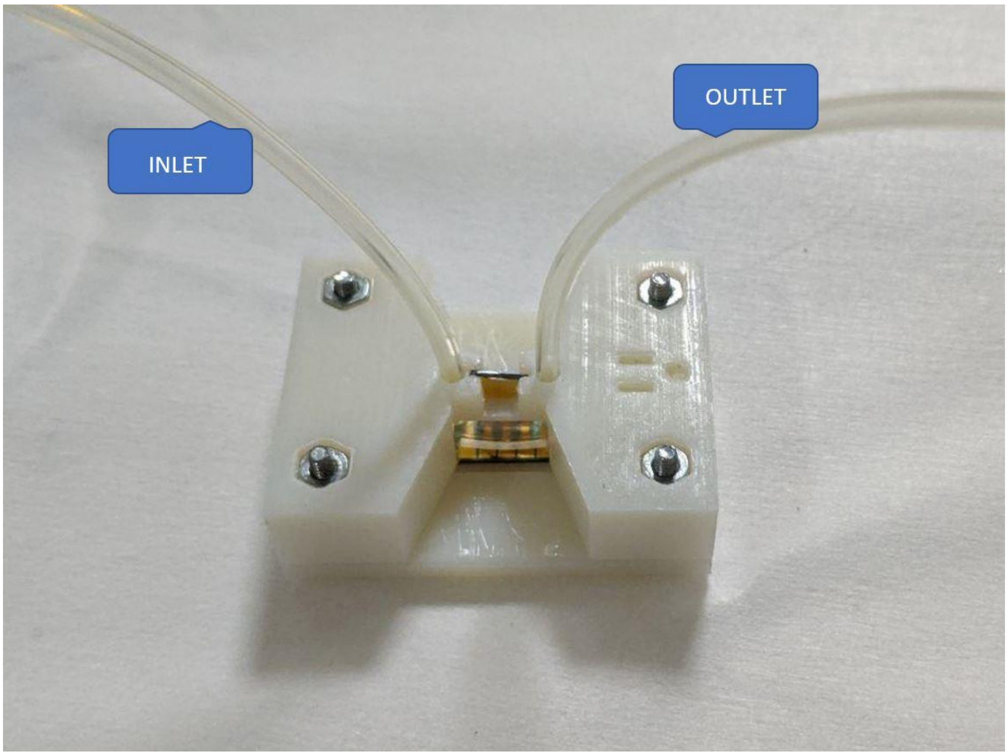

Fig. 2.5: An EGOFET sample, contacted with a PDMS chamber, containing the electrolyte, and with a gold electrode dipped into it. Inlet microtube delivers the electrolyte solution and outlet microtube let it flow to the external world. Inlet and outlet are labelled.

2.2 Methods

2.2.1 Technological process

The starting point of the technological process was a p-type Si wafer covered by 1 μm of SiO_2; the first step was the electron-beam evaporation of two layers: 10nm of Ti and 100nm of Au.

In a class 100 clean room, standard UV photolithography was carried out to pattern interdigitated source and drain electrodes as in *Fig. 2.13*.

A positive tone photoresist (AZ1518, MicroChemicals GmbH) (see *Fig. 2.6*: Positive and negative resist. With a positive resist (a) it is possible to create holes in the zones not covered by the photomask; with a negative resit (b) holes are created correspondingly to the etch resistant mask features) was spin coated on the substrate at 500 rpm for 5 s and 4000 rpm for 30 s and then soft-baked onto a hot plate at 110 °C for 60 s.

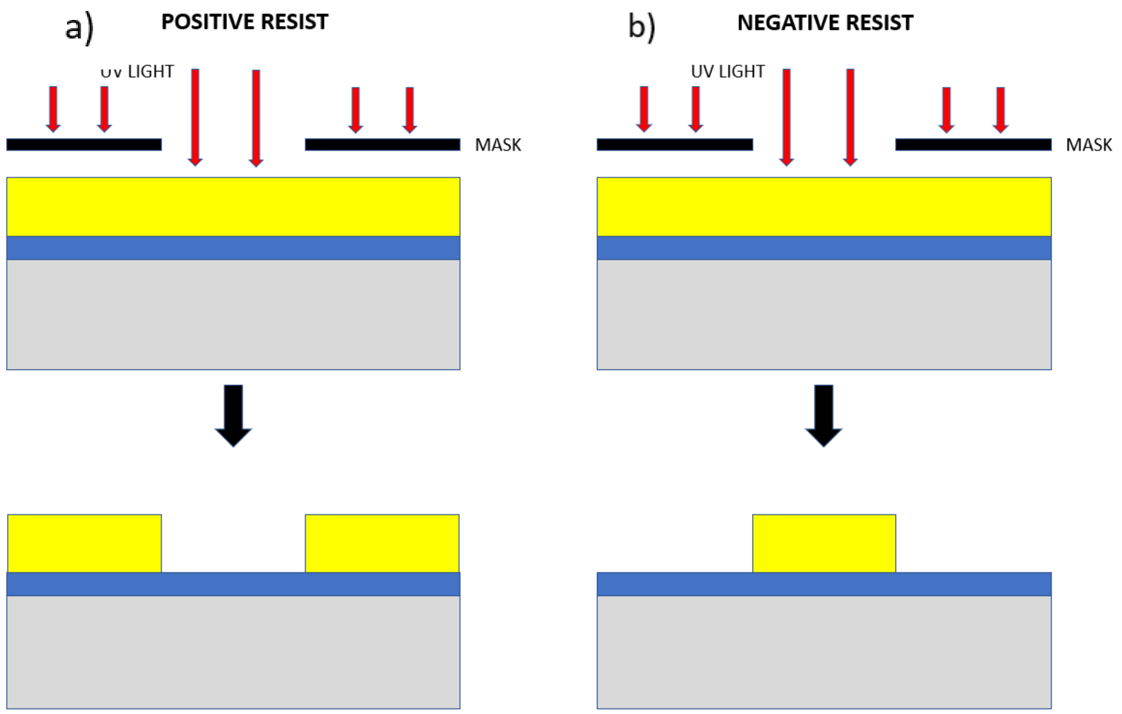

Fig. 2.6: Positive and negative resist. With a positive resist (a) it is possible to create holes in the zones not covered by the photomask; with a negative resit (b) holes are created correspondingly to the etch resistant mask features.

Exposure and development are the crucial steps for photolithography: the exposure is performed in contact mode, and the wafer exposed to UV light for 5 seconds at a power of $10\, mW/cm^2$. For the exposure it was employed a Neutronix Quintel NXQ-4006 Mask Aligner (see *Fig. 2.7*). To check whether the samples were produced successfully or not, it was used a microscope Nikon Eclipse ME600.

During exposure, alignment of the mask with the wafer is mandatory as shown in *Fig. 2.8.*

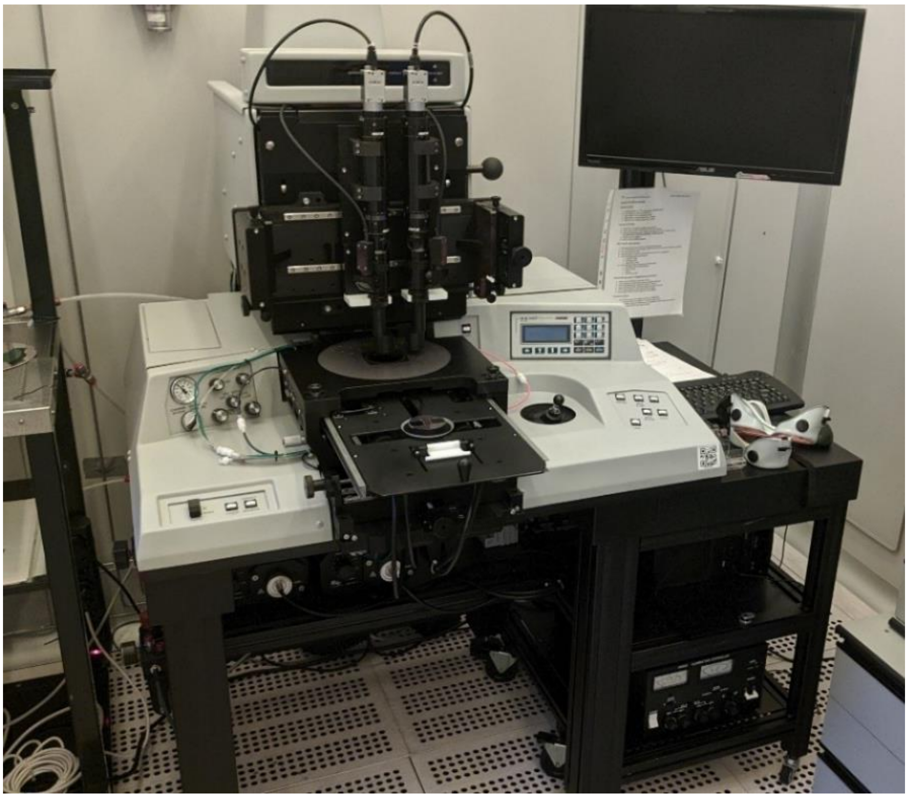

Fig. 2.7: Neutronix Quintel NXQ-4006 Mask Aligner

Following exposure, developing the photoresist in aqueous-alkaline solution is essential to dissolve the part exposed to the UV rays (for a positive resist). This recipe uses a solution of water and developer (AZ400K, Microchemicals GmbH) in proportion 3:1; wafers are dipped into it for about 30 seconds and then rinsed in water. To optimize the process an hard bake at $115°C$ for 60 seconds can be performed after developing.

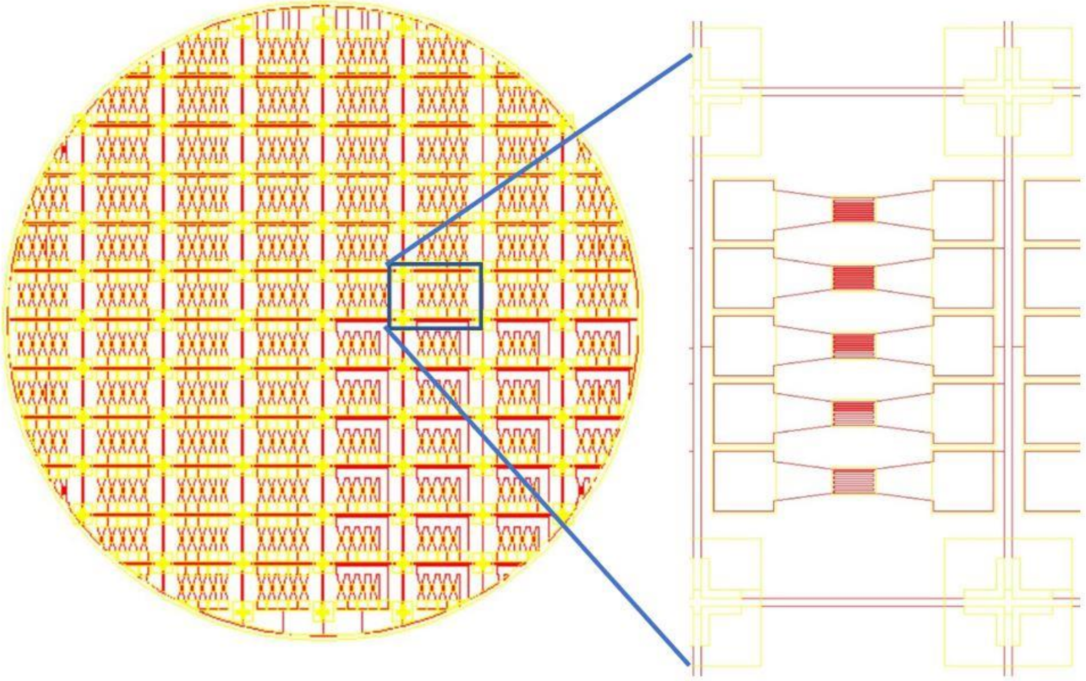

Fig. 2.8: Mask pattern of EGOFETs wafer. In the detail on the right, one can appreciate the alignment marks on the corners of each set of five device which are very useful to adjust the wafer by translation and rotation according to similar marks on the wafer.

The process is then completed with etching. Etching is the final step that remove unwanted areas, dissolving them in chemical solution (wet etching) or by reacting with gases (dry etching).

In the present work, source and drain are patterned through a wet gold (Techni Etch AC12, MicroChemicals GmbH), followed by titanium etch, $(HF + H_2 0_2 +$

$H_2O = 1:1:20$) generally faster and cheaper than dry etching, while the areas protected by not developed resist will remain unchanged.

The following step is passivation. Usually, for devices operating in non-aqueous conditions, passivation is used for protection against corrosion due to air and external agents. EGOFETs instead, require passivation as a protection against short-circuits between the gold electrodes (source and drain) and the electrolyte when in contact. Passivation requires another photolithographic multi-step process:

a) Application of a primer or adhesion promoter: Ti prime was chosen because it can be easily applied via spin-coating without drawbacks. Ti prime was spin coated at 4000rpm for 60 seconds and followed by an hard baked at $120°C$ for 120 seconds.
b) Polyamide was spin-coated at 4000rpm for 60 seconds, then baked at $85°C$ for 120 seconds. Polyamide is a polymer whose repeating unit is made up by the amide (see *Fig. 1.13*)
c) Exposition for 25 seconds
d) Development for 120 seconds
e) Hard bake at $350°C$ for 120 seconds

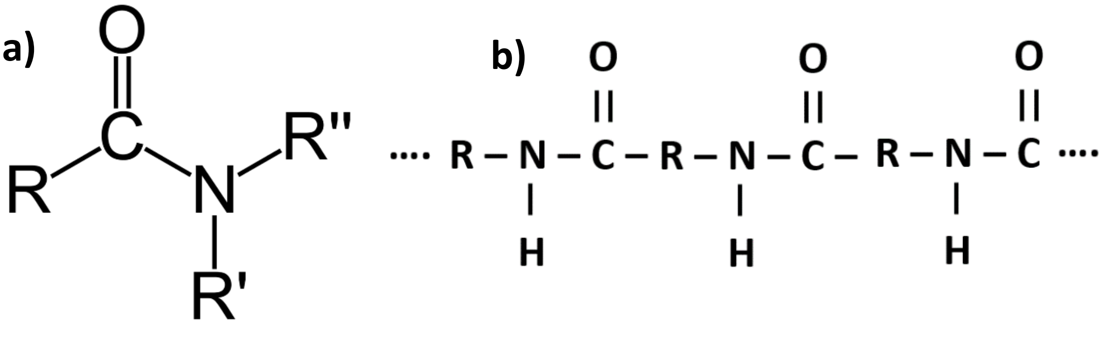

Fig. 2.9: a) Amide monomer. The letters R, R′ and R′′indicate often hydrogen groups or organic groups b) Polyamide chain

For the developing of passivation photolithography, the developer AR300-26 was purchased from All Resist.

Wafers were laser cut by external service. At this point the chips, with five devices in parallel each, are obtained and ready for the deposition of the polymer (see *Fig. 2.10*).

Preparation of polymer solution is carried out: the polymeric powder is dispersed in a proper solvent in accurately measured quantities: for this work, the chosen solvents for P3CPenT was DMSO in proportion 2,5 mg/mL. P3CPenT was purchased from Rieke Metals and DMSO from Sigma-Aldrich. Afterwards, the solution is left stirring overnight at $50°C$ and 400rpm. The compounds are spin coated onto the devices at 500rpm for 5 seconds and at 2000 rpm for 30 seconds.

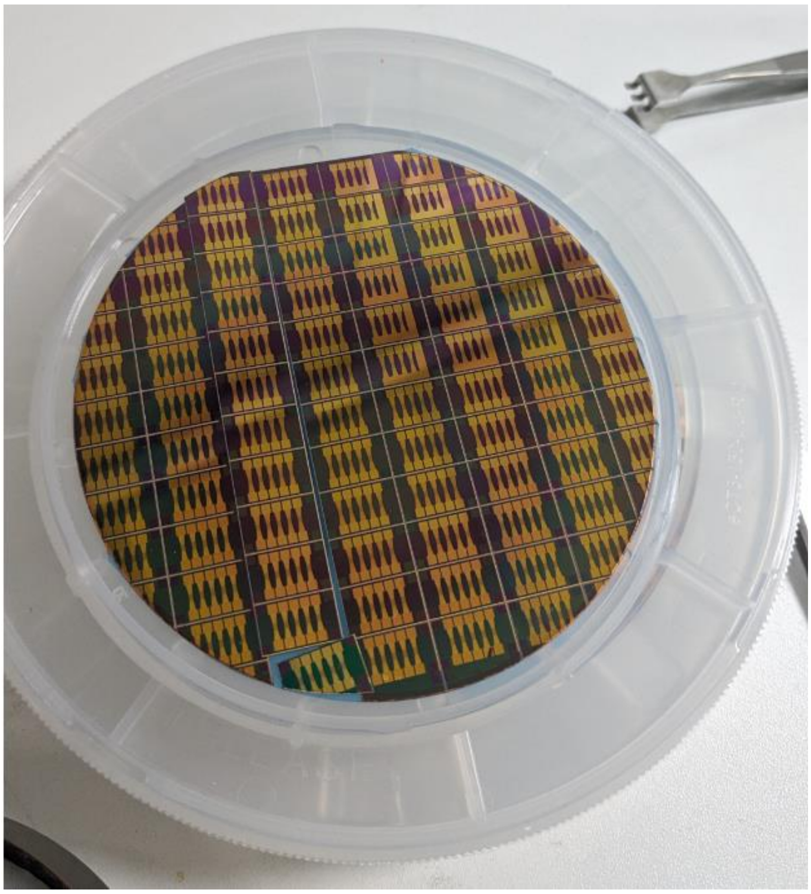

Fig. 2.10: After laser cutting, chips on the wafer are ready for polymer spinning.

The last step is the hard bake: chips are kept protected from light, placed in an oven shielded by the light, avoiding any kind of stress one the light sensitive polymer, and then cooked at least for 2 hours at 75°C.

At the end of the fabrication process, an example of a sample ready to be tested is shown in *Fig. 2.11*.

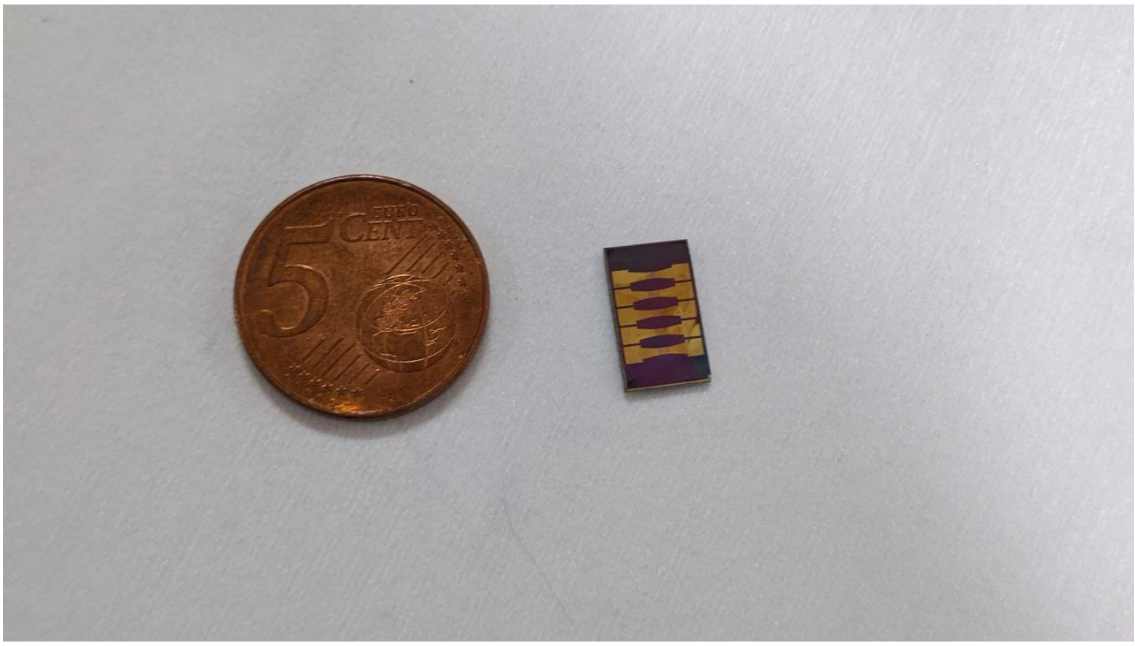

Fig. 2.11: EGOFET sample at the end of the technological process, next to a 5 cents coin

In *Fig. 2.12* is shown the pattern used to define the interdigitated pattern of source and drain on the device. The interdigitated geometry defines a channel width W=9590 μm and a channel length L=10μm, so that the channel width cannot be counted as a straight path from one electrode to the other but as the serpentine defined by the interdigitated fingers: in this way W/L ratio is maximized and consequently, the current flow in the channel. In order to check whether the technological process was carried out successfully, the samples were observed at microscope, as in *Fig. 2.13*.

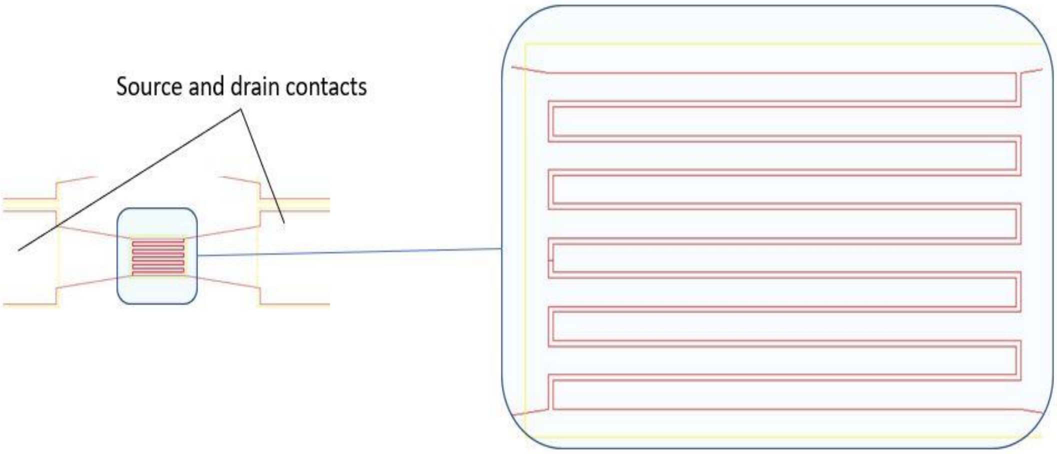

Fig. 2.12: Interdigitated source and drain mask pattern.

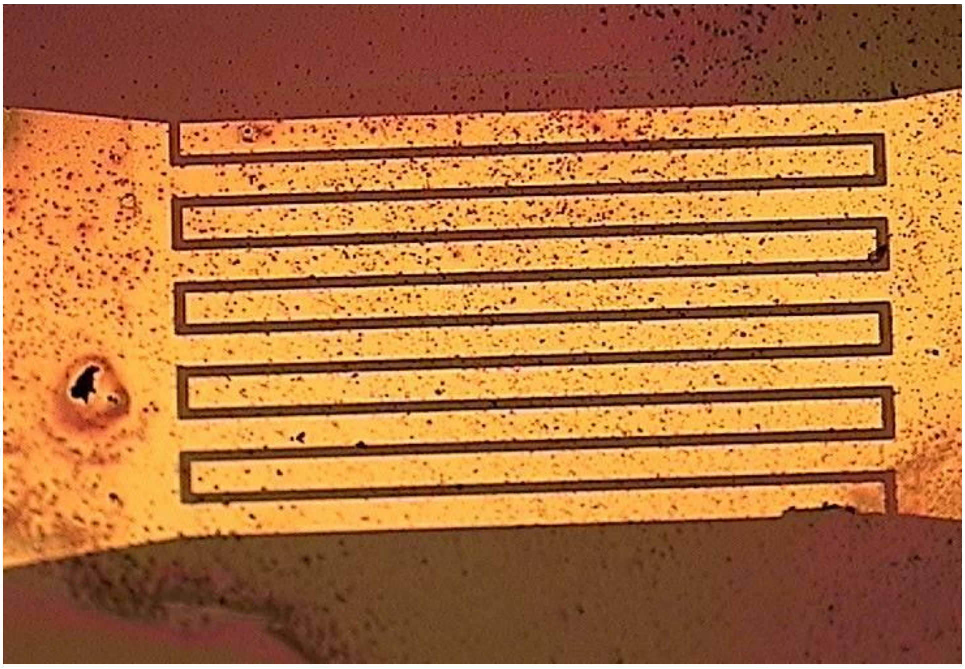

Fig. 2.13: Interdigitated source and drain layout view at microscope. The little black points are polymer aggregates. For this snapshot it was used the 10x focus.

2.2.2 Microfluidic set-up

A microfluidic chamber is required to host the electrolyte upon the device. For this work the simple idea to fill a Polydimethylsiloxane (PDMS) chamber placed upon the channel and allowing contact with the electrodes was chosen. PDMS was produced with Syligard 184 Silicone, both elastomer and curing agent purchased from DOWSIL.

PDMS is a polymeric organosilicon compound, which is often employed in microfluidic since its biocompatibility, and relatively ease of production. To produce the PDMS microfluidic chamber, a PMMA master with the layout of the chamber was employed and the silicone was made with two compounds: the elastomer and the curing agent in proportion 10:1. The two are mixed, and then degassed in a vacuum doorbell to remove all the bubbles. When the mixture showed no bubbles, it was poured in the PMMA master and left for 2 hours onto a hot plate at $75°C$. The PDMS chamber (see *Fig. 2.14*) final volume is of 60 µL.

The PDMS chamber is part of a larger system that is included in what was called "Microfluidic device"; the other parts that makes up this system are a 3D-printed sample holder and a 3D-printed cap. There are two different caps because of the two different electrodes shapes (see *Fig. 2.15*): one is designed for the Ag/AgCl electrode, so it has a small circular hole; the other has to fit when using the gold gate and it is provided with a tiny rectangular aperture.

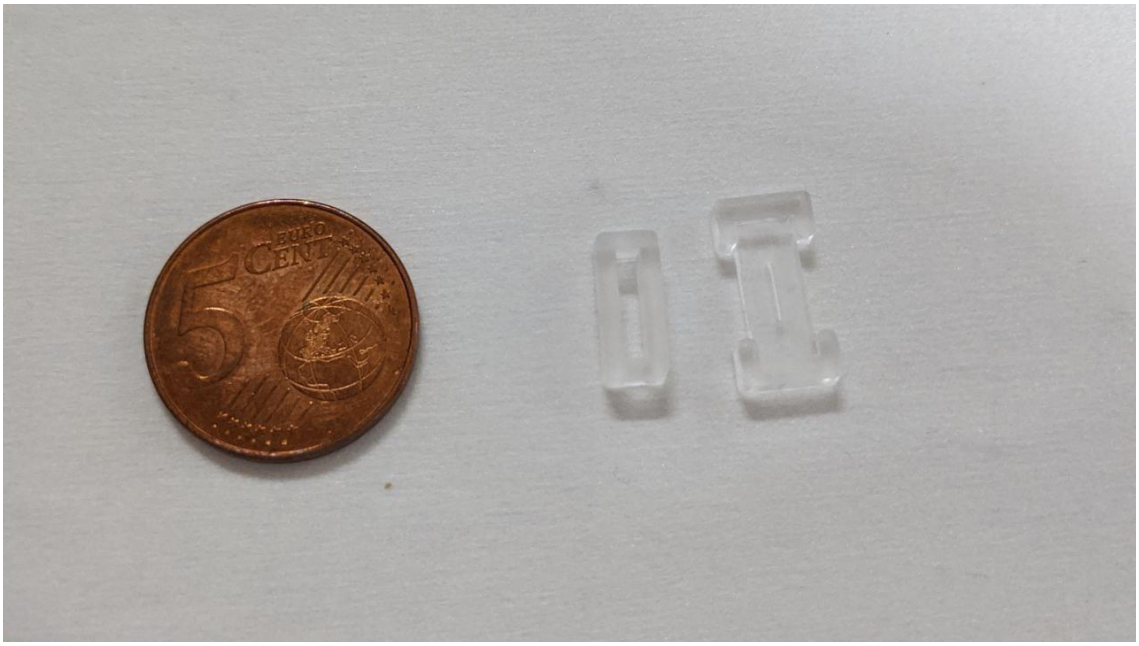

Fig. 2.14: A PDMS chamber with a corresponding cap, used to avoid leaks of the electrolytic solution.

Advantages of this configuration are:

- no PDMS-wafer bonding required

- leakage-free liquid flow up to 120 μL/min

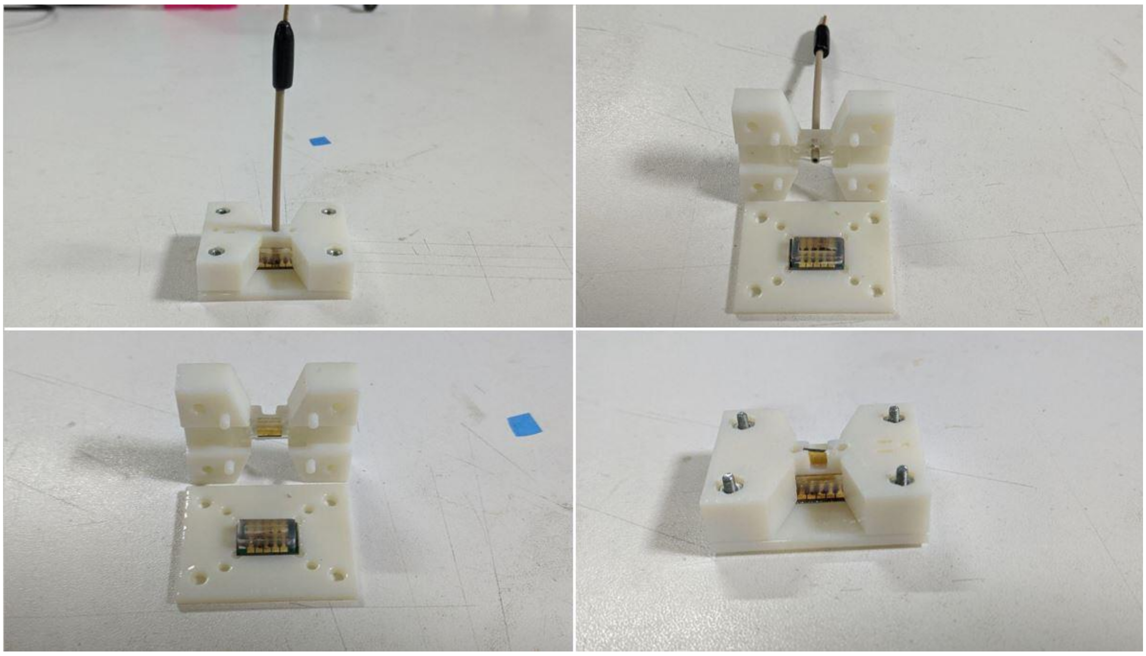

Fig. 2.15:Top left and right corner for the microfluidic chamber integrated with the Ag/AgCl electrode; down left and right corner for the microfluidic device integrated for the gold electrode

2.2.3 Measurements

All the measurements performed can be divided in two bigger categories: characterizations and current vs. time curves.

A first- static characterization cycle was performed on the day of fabrication: it included transfer characteristics and output characteristics at fixed electrode and ionic strength in the electrolyte. For the output curves, the sweep of V_{DS} occurs with a step of 5 mV in a range $[-0.6; 0]$ V: voltage V_{DS} moves from 0 V down to -0.6 V and back to 0 V, and every time a cycle is completed V_{GS} is increased with a step of 0.1 V, starting from 0 V up to $-0.5V$. The obtained curves are of the same type as in *Fig. 2.16* . Output curves have been measured at scan rates: 8 mV/s, 20 mV/s and 80 mV/s. For the transfer characteristics, the sweep of V_{GS} is performed with a step of 5 mV in a range $[-0.6; 0]$ V: voltage V_{GS} moves from 0 V down to -0.6 V and back to 0 V, and every time a cycle is completed V_{DS} is increased with a step of 0.1 V, starting from 0 V up to -0.5 V (see *Fig. 2.17*). Transfer curves have been measured at the same scan rates: 8 mV/s, 20 mV/s, 80 mV/s.

Repeated transfer characteristic: it is a repeated transfer characteristic measurement while the drain is at a fixed potential, usually at 0.5 V, and anyways within the above-mentioned output characteristic V_{DS} sweep range ($[-0.5; 0]$ V).

For the acquisition, V_{GS} is swept with 10 mV steps in a range from 0 V moving down to -0.6 V and back to 0 V. Repeated transcharacteristic measurements have been performed at a scan rate of 40 mV/s for 10 times and 100 times.

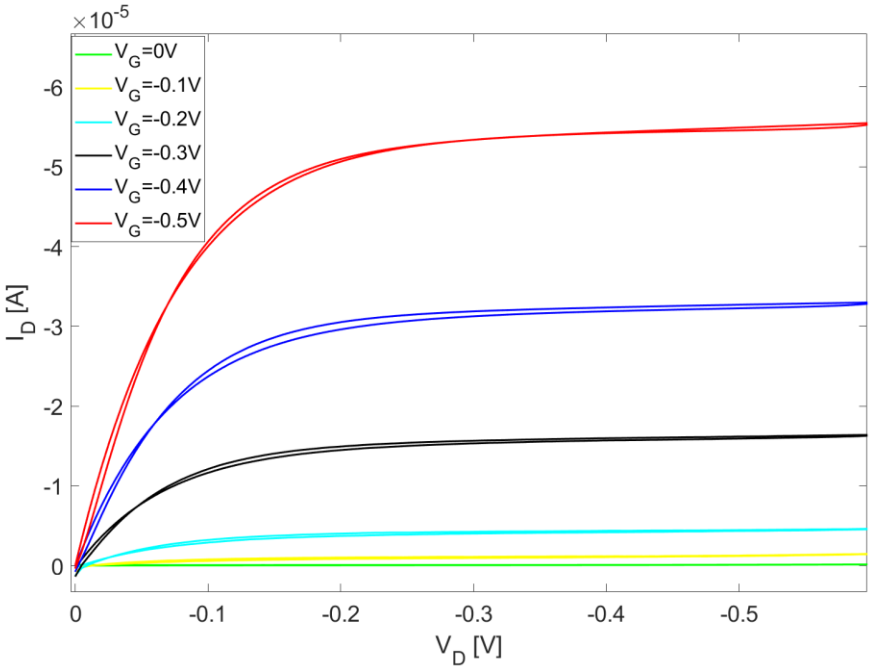

Fig. 2.16: Example of output characteristic response at different drain voltage values.

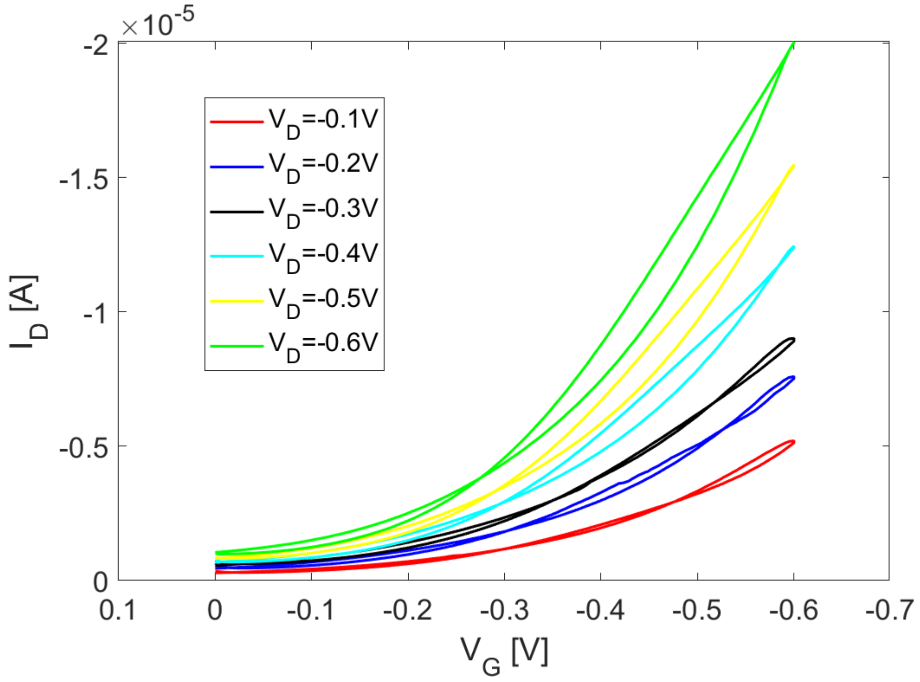

Fig. 2.17: Example of transfer characteristic response at different voltage swipe

After characterization of all devices was completed at every scan rate, gate voltage pulses measurements were carried out: this technique is based is on recording the current flowing in the device in response to a double potential step, where the second potential step was the same potential as the initial one, resulting in a square wave. This input was applied at the gate with increasing voltages steps of 100 mV, from 100 mV up to 500 mV, while the drain was kept at 0 V. By analysing the behaviour of the current, one can acknowledge whether the current can be assessed to be a capacitive one (due to separation of charges between the electrode and the electrolyte), or a faradaic one (a current mainly generated from the electrode by oxidation and reduction reactions of chemical substance).

For negligible bulk capacitance device, Faradaic processes are usually much slower than capacitive ones, therefore, to enhance the observation of the capacitive component due to charge/discharge of the double layer, the measurement has to be performed at high sampling rates. For these experiments, every new point was acquired after 10 ms, resulting in a sampling rate of 100 Hz.

As it can be seen in *Fig. 2.18*, the potential step is kept high for a time τ, after which it goes to the second potential step, that in this experiment matched with the initial condition. After the pulse had been sent to the gate terminal, the response of the device is recorded in a plot I_G *vs. time*; then one must divide the capacitive current from the faradaic contribute: in the first instants immediately after the square wave is applied, the discharge has an exponential decay, showing that capacitive contribute is dominating, whilst for the rest of the measure, the slow decay of the faradaic current becomes dominant (see *Fig. 2.19*) [59] [60].

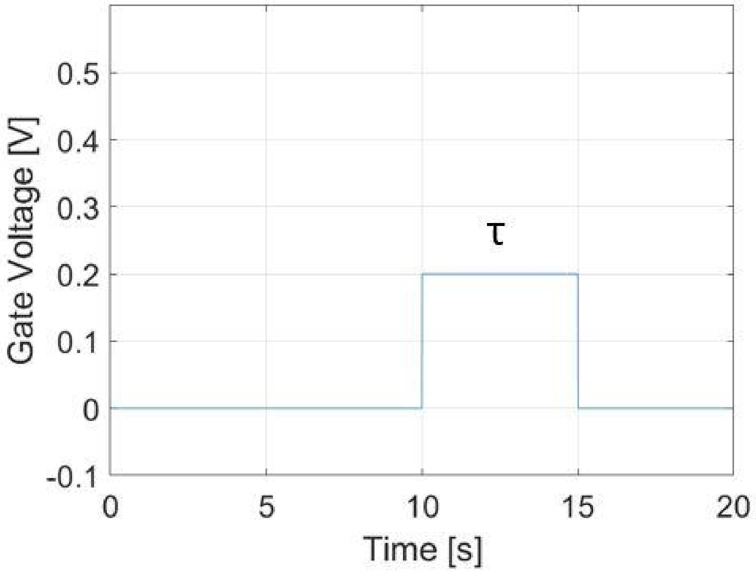

Fig. 2.18: Example of a double potential step for chronoamperometry. In this example the square wave applied has an amplitude of 0.2V

Faradaic current is addressable to charges that manage to cross the electrode/electrolyte interface thanks to reduction and oxidation reactions. This is established as a steady-state process. Indeed, it could go on as long as a current flows, supplying the reactants to replace the by-products that leave the electrode. Non-faradaic or capacitive current are those related to the progressive charge/discharge of the electrical double layer.

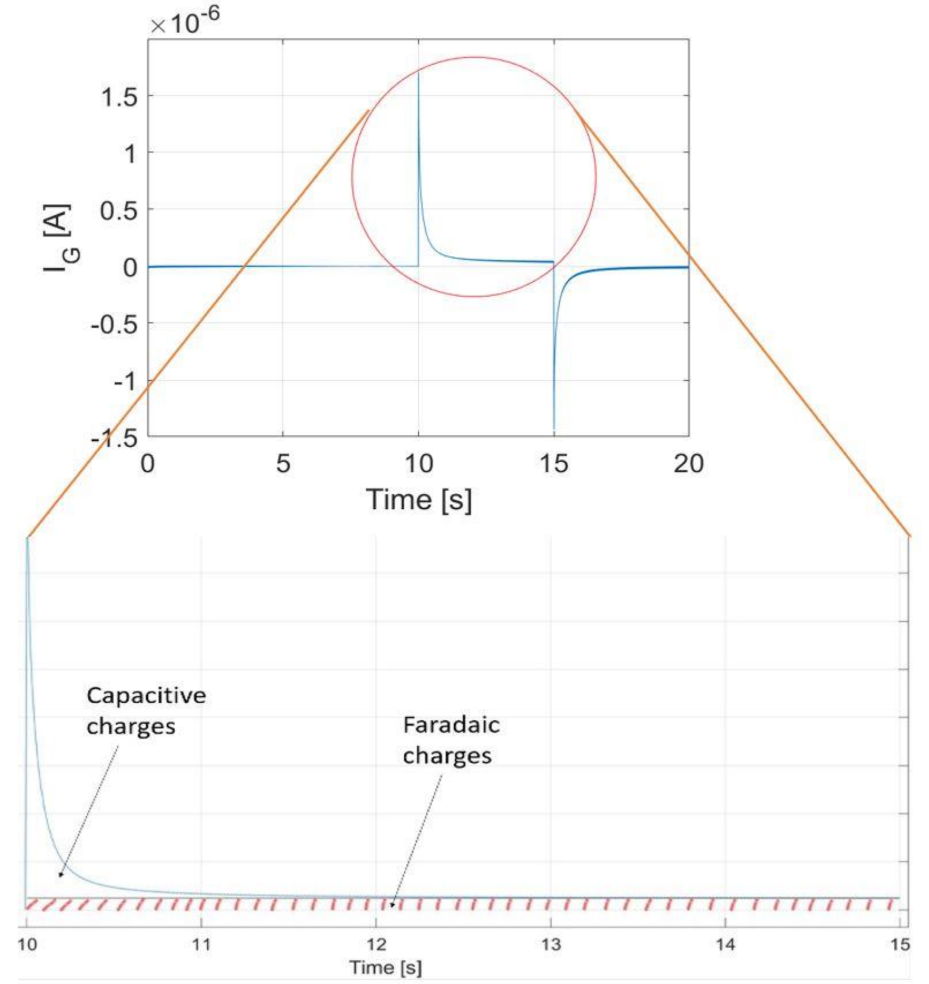

Fig. 2.19: Ideal separation of the faradaic and non-faradaic contributes

The electrical double layer capacitance has been extracted from these gate pulse measurements (see *Fig. 2.18* and *Fig. 2.19*). Only the contribution due to capacitive effects was kept, while the faradaic current was discarded [61].

As it holds the following:

$$i = \frac{\partial Q}{\partial t} \qquad (2.1)$$

To obtain the charge associated to this measurement, it is sufficient an integration, which practically reduces to the calculation of the area under the non-faradaic curve. To determine the capacitance, five gate voltage pulses measurements were carried out, each one with a different potential to polarise the gate: *100 mV, 200 mV, 300 mV, 400 mV, 500 mV*.

For each one the charge was calculated, as a contribute related to a specific gate voltage value, and in turn plotted in a *Q vs. V* plane.

As it can be seen in *Fig. 2.20*, the points can be fitted into a straight line, whose slope gives the capacitance [62]. The slope of the fitted curve represents the total capacitance.

Finally, dividing the slope of the fit by the active area of single device, it can be expressed as capacitance per unit area.

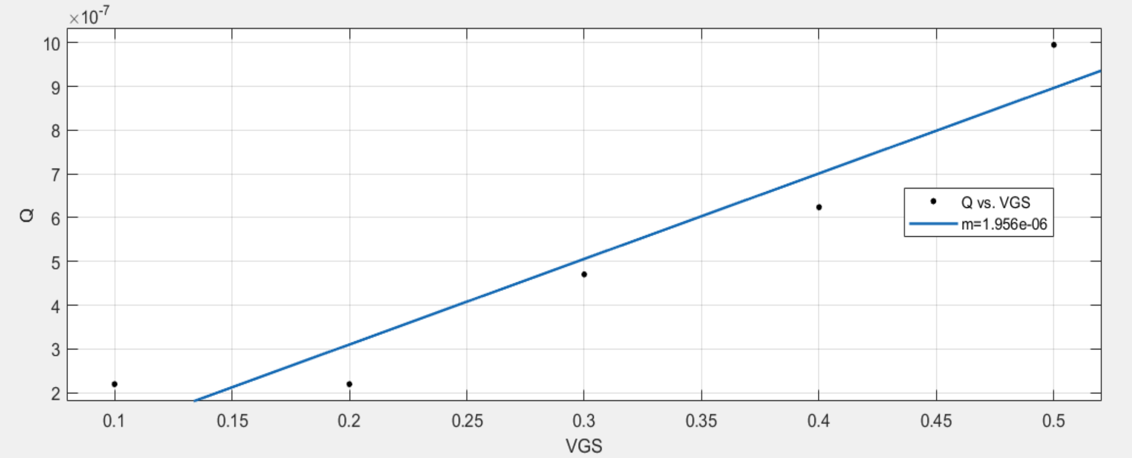

*Fig. 2.20: Example of a straight line fit of the capacitive charges with respect to the gate voltage VGS. The fitted model is described by the equation: f(x) = p1*x + p2, where p1 = 6.303e-06 (p1=m), p2 = -5.882e-07 and with R-square: 0.8936*

Capacitance is a very important parameter for the future implementation of EGOFETs as biosensors. In order to work as a biosensor, the devices will require an interface functionalization, whether it is practiced on the gate/electrolyte or on the polymer/electrolyte surface. Functionalization is a treatment specifically tailored to make a surface (whether it is applied on the gate or the polymer) sensitive to a target molecule. When target molecules are present into the electrolyte, the functionalized device is capable to capture it. This operation physically changes the arrangement of the electrical double layer, and consequently the capacitance at the interface.

Following the characterization and the gate voltage pulse measurements, the best working device of the sample, underwent a stability test. Whilst the characterizations mentioned above are very well-known in the transistors world, as they are plotted to characterize the electrical behavior of an electronic device, this kind of measure is widespread in the biosensors world instead. But if more generally, real-time measurements are employed for monitoring current variation correlated in time when different analytes are introduced into the system, in this thesis they are performed to evaluate the stability overnight of the tested devices. A typical measurement lasted between 12-16 hours: during the measurement, each device underwent an applied voltage of $-0.5V$ at the gate electrode and of $-0.4V$ at the drain terminal.

2.3 Materials

Gate electrodes used are squared "homemade" gold plate of dimensions $5x5\ mm$ and a commercial Ag/AgCl Leak Free Reference electrode purchased from Warner Instruments (see *Fig. 2.21).* Taking into account, that only a part of the electrodes will be dipped into the electrolyte, which is around *1.5 mm,* the estimated effective areas, that will take an active part are approximately one ten times of the other:

- $AREA_{Ag/AgCl} = \pi \cdot r^2 = \pi \cdot (0{,}5\ mm)^2 = 0{,}785\ mm^2$
- $AREA_{Au} = b \cdot h = (5\ mm) \cdot (1{,}5\ mm) = 7{,}5\ mm^2$

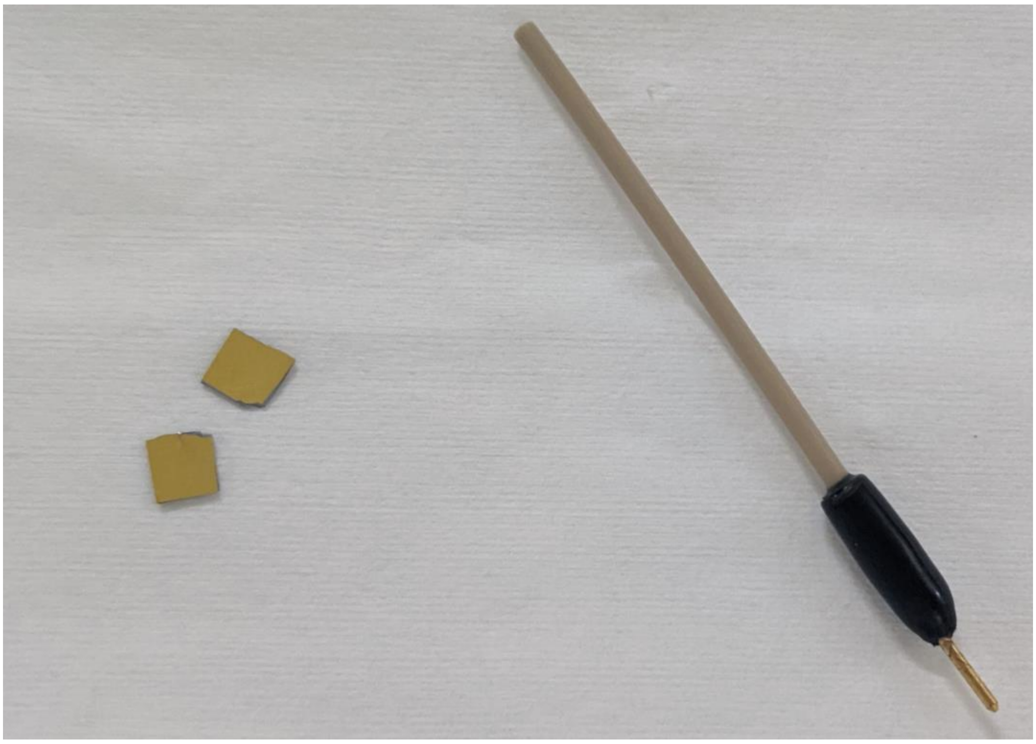

Fig. 2.21: On the left, gold plates used as polarizable electrodes; on the right the Ag/AgCl leak free reference electrode used as non-polarizable electrode.

Common Ag/AgCl reference electrodes, are subject to chloride ions leak through the porous junction, thus affecting the measurements. The 'Leak free' reference electrodes (Model W4 69-0025) use a non-porous and highly conductive junction that ensures no migrations of the solution in either direction and great stability in time and temperature. Thanks to this particular feature, it manages to eliminate the problems associated with the use of conventional porous junction-based reference electrodes such as clogging, sample contamination, electrolyte loss, changing of ionic strength of the sample, and the difficulties with organic based solvents [63]. The gold electrode was fabricated, by e-beam evaporation of a 10 nm Ti adhesion layer and 100 nm-thick Au layer. The dicing of the wafer in 5 $mm\ x$ 5 mm squares was performed in Microla Optoelectronics.

The electrolyte was produced by dissolving 100 mM of $NaCl$ in deionized water ($DI - H_2 0$). To prepare the 10mM and 1mM solutions, the 100mM was first diluted 1:10 to obtain the former, and then again further diluted in ratio 1:10 to obtain the latter. NaCl was chosen for its structural simplicity: its lattice is composed by two big grains Cl^- and Na^+ which results in a structure much simpler to analyse with respect to more complex buffers (i.e., PBS).

3 Results and discussion

3.1 Characterization curves

Transfer and output characteristics have been performed for all the five devices over each sample at three different scan rates for both electrodes. Leakage current (not showed) has been monitored throughout all the experiments and found to be at least 2-3 orders magnitude below the source and drain current. The transfer and output measurements, performed at scan rates 8 mV/s, 20 mV/s, 80 $mV/$s are shown for the Ag/AgCl gate electrode according to their ionic strength: in *Fig. 3.1* and *Fig. 3.2* NaCl concentration is 1 mM, in *Fig. 3.3* and ***Error! Reference source not found.****4* NaCl concentration is 10 mM, and in *Fig. 3.65* and *Fig. 3.56* NaCl concentration is 100 mM. The corresponding measurements performed with the Au gate electrode are shown in ***Error! Reference source not found.****7,* ***Error! Reference source not found.****8,* ***Error! Reference source not found.****9* and ***Error! Reference source not found.****0.* Data acquired for the samples with gold gate electrode at 1mM ionic strength were considered not reproducible and will not be discussed in the following. Gate leakages are registered with values around $10 - 100\ nA$, ensuring overall, two-three order of magnitude difference from I_{DS}.

An insight on gate currents is offered at *Fig. 3.111* and ***Error! Reference source not found.****2,* for the case at 10mM.

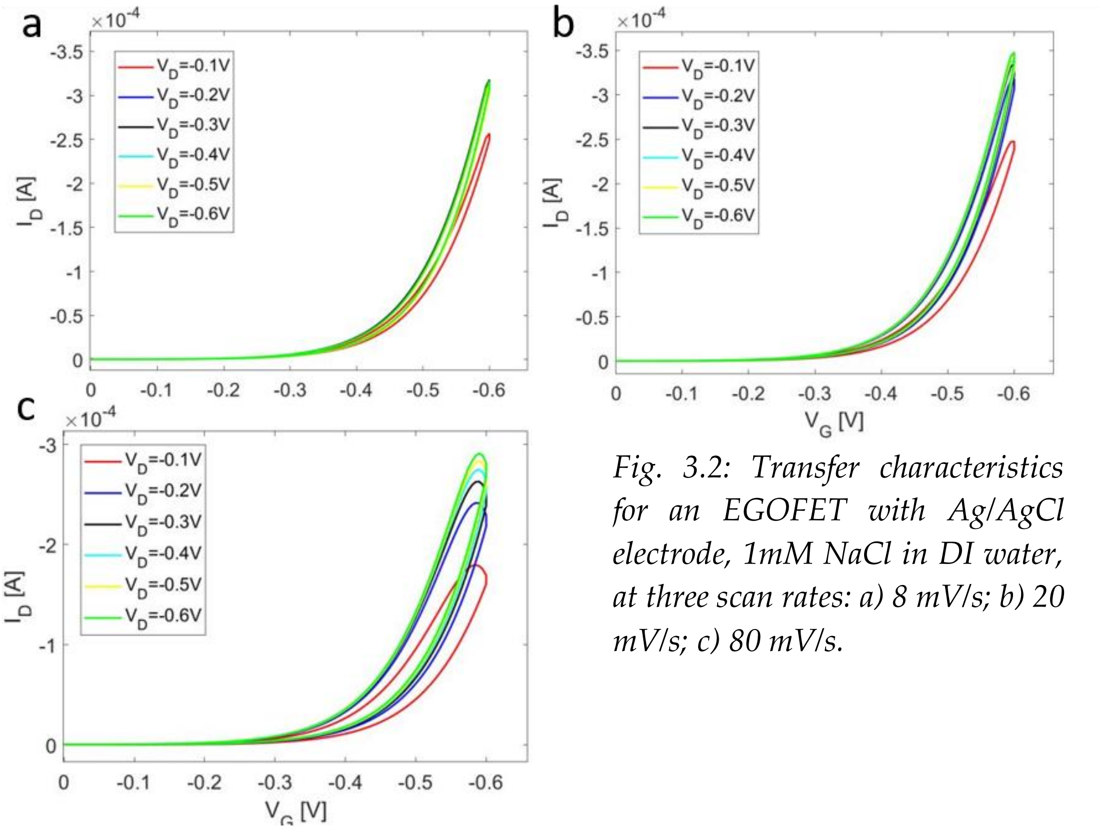

Fig. 3.2: Transfer characteristics for an EGOFET with Ag/AgCl electrode, 1mM NaCl in DI water, at three scan rates: a) 8 mV/s; b) 20 mV/s; c) 80 mV/s.

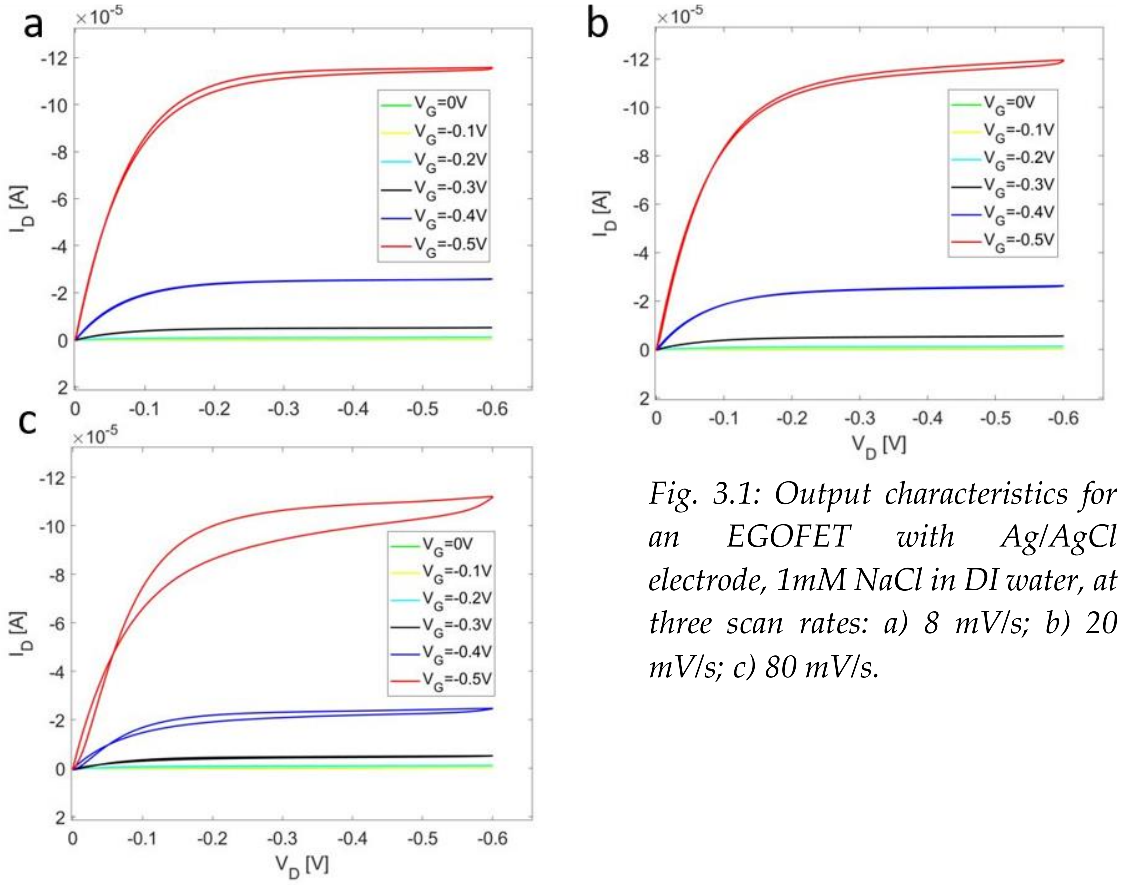

Fig. 3.1: Output characteristics for an EGOFET with Ag/AgCl electrode, 1mM NaCl in DI water, at three scan rates: a) 8 mV/s; b) 20 mV/s; c) 80 mV/s.

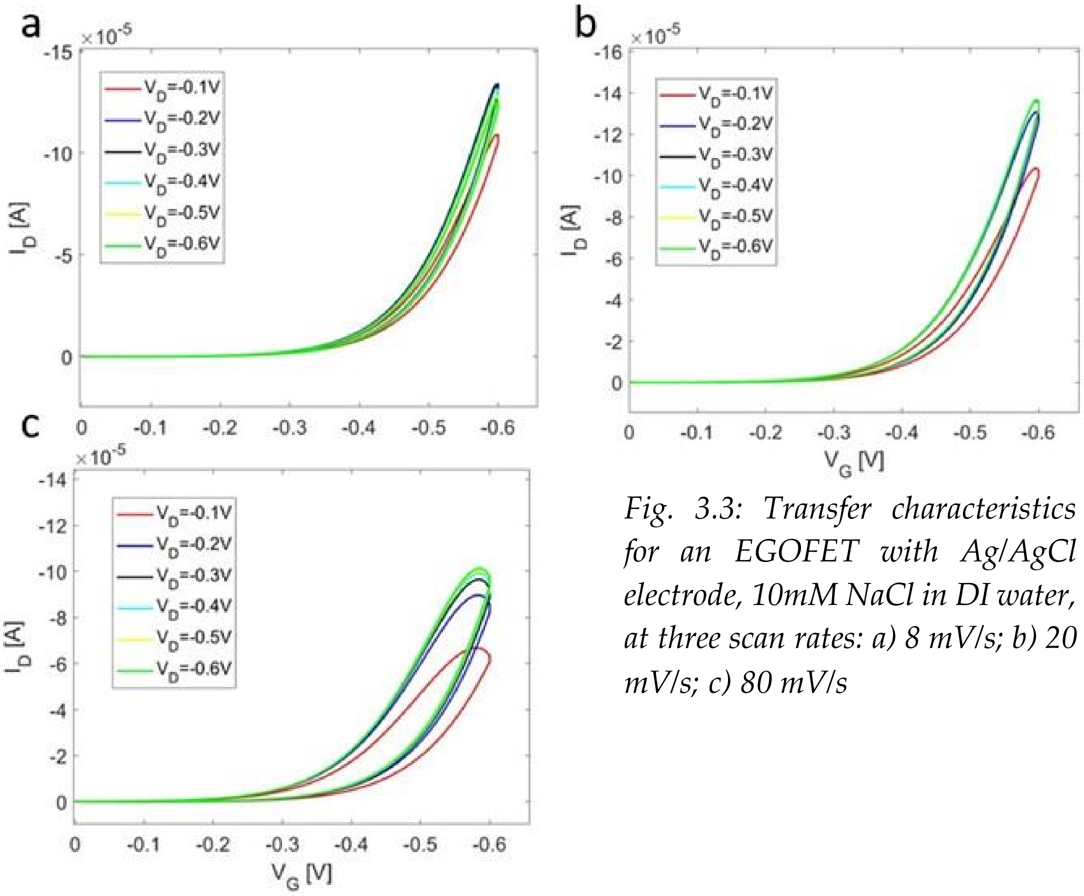

Fig. 3.3: Transfer characteristics for an EGOFET with Ag/AgCl electrode, 10mM NaCl in DI water, at three scan rates: a) 8 mV/s; b) 20 mV/s; c) 80 mV/s

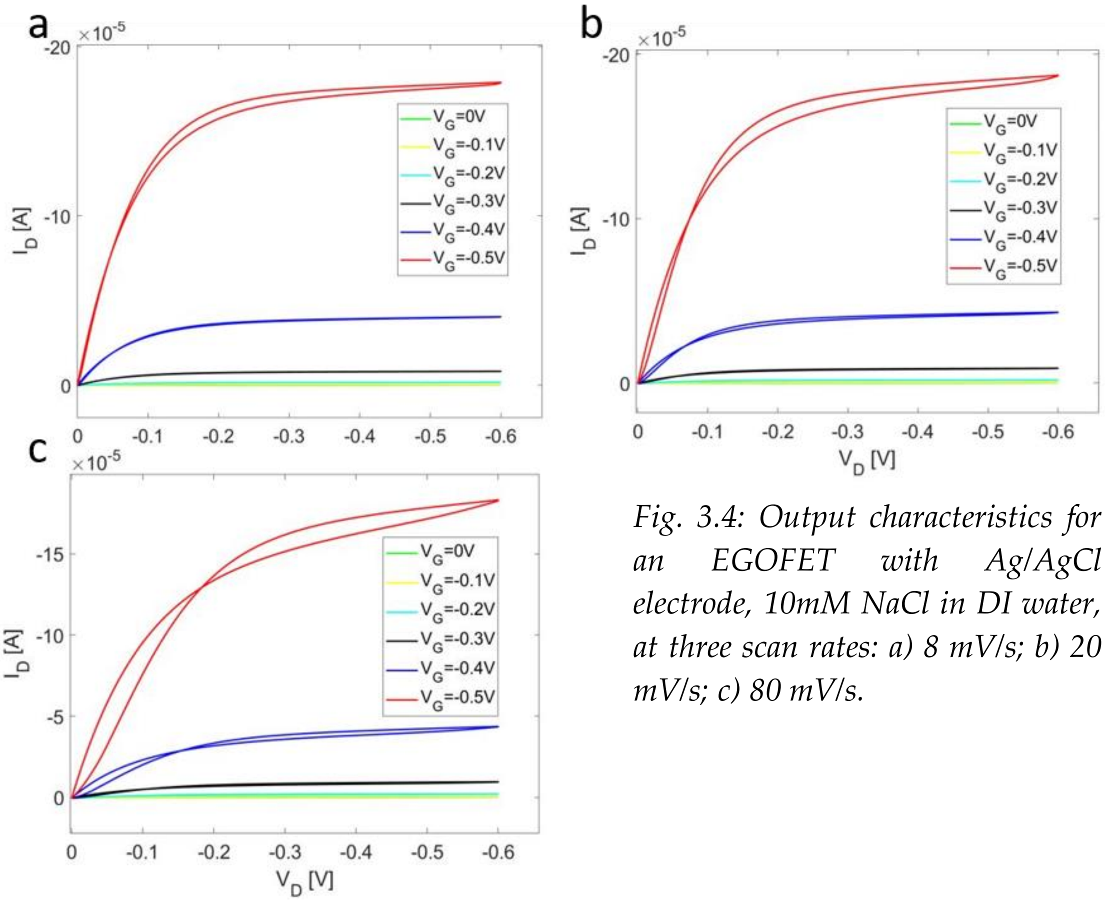

Fig. 3.4: Output characteristics for an EGOFET with Ag/AgCl electrode, 10mM NaCl in DI water, at three scan rates: a) 8 mV/s; b) 20 mV/s; c) 80 mV/s.

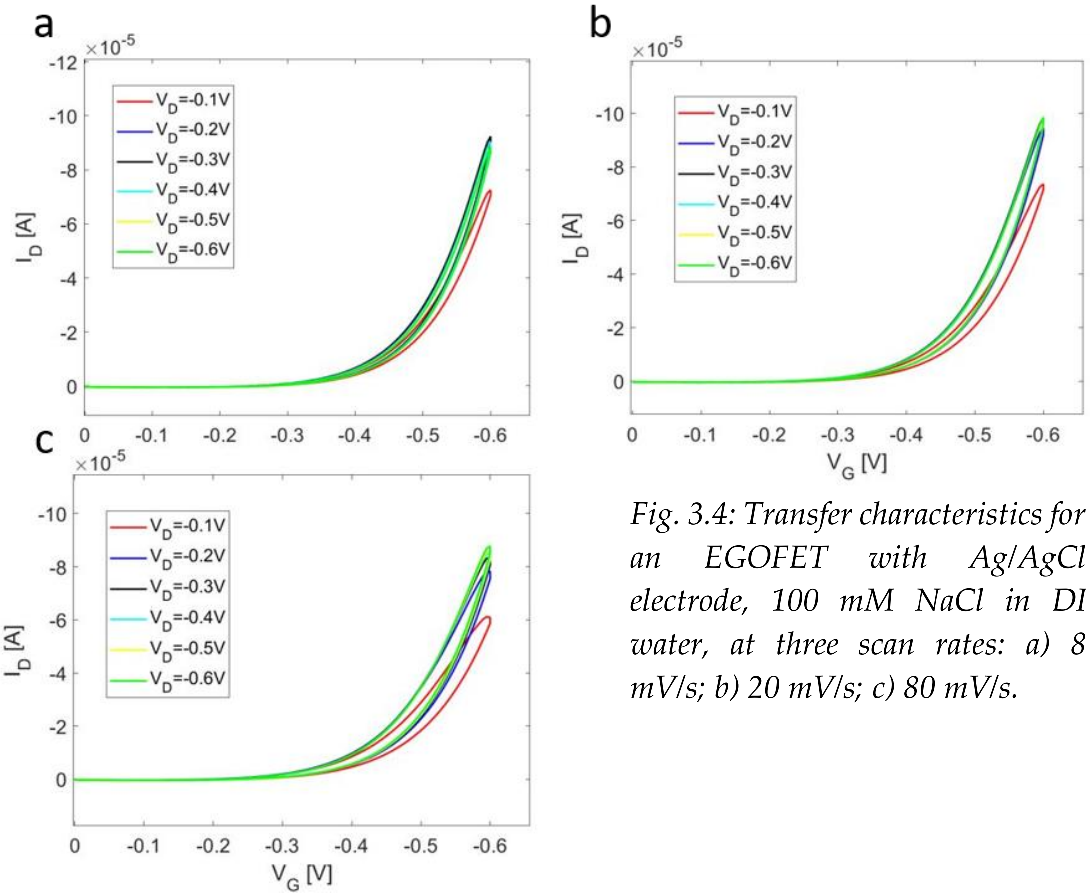

Fig. 3.4: Transfer characteristics for an EGOFET with Ag/AgCl electrode, 100 mM NaCl in DI water, at three scan rates: a) 8 mV/s; b) 20 mV/s; c) 80 mV/s.

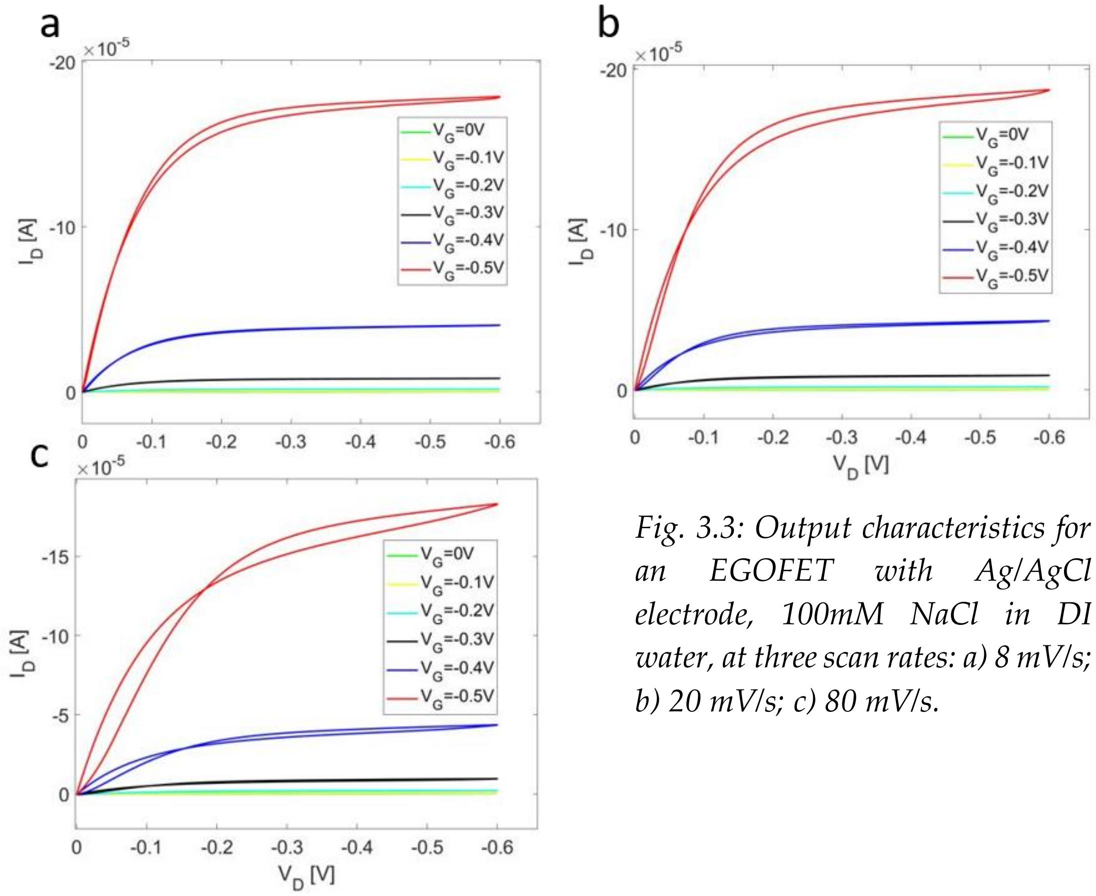

Fig. 3.3: Output characteristics for an EGOFET with Ag/AgCl electrode, 100mM NaCl in DI water, at three scan rates: a) 8 mV/s; b) 20 mV/s; c) 80 mV/s.

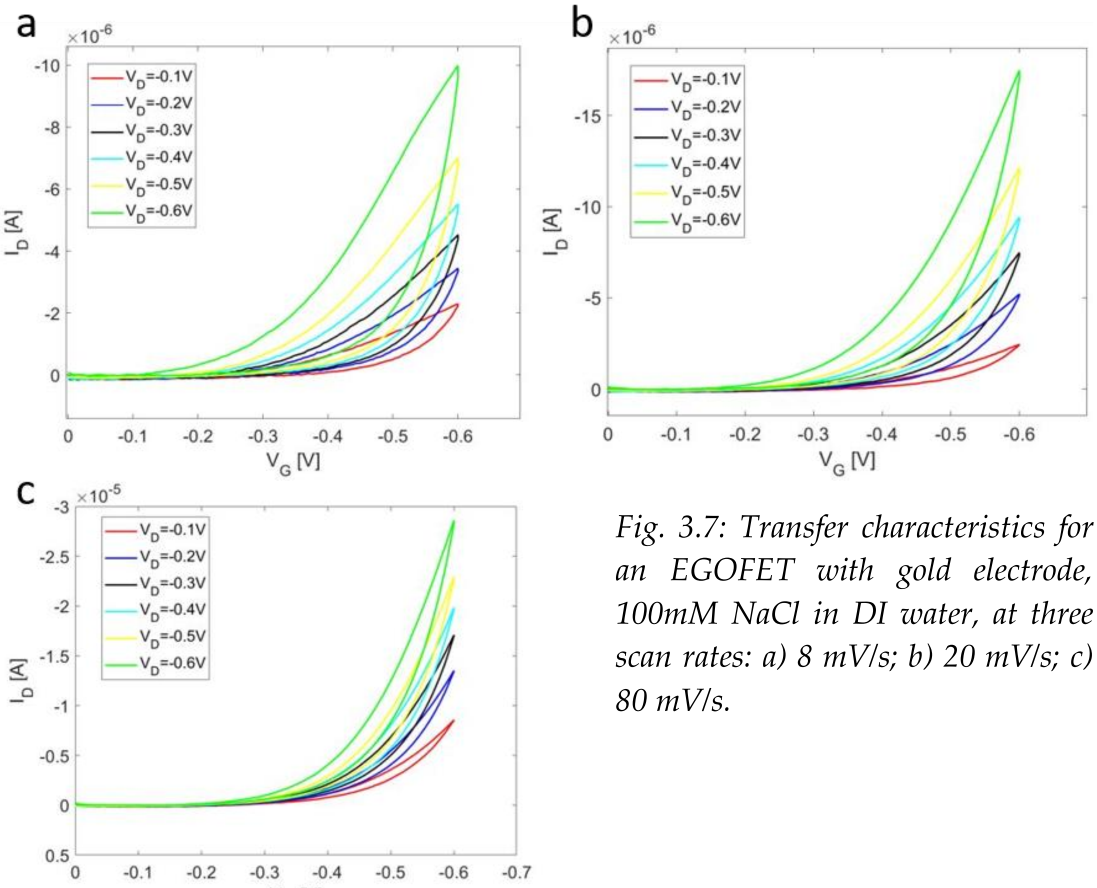

Fig. 3.7: Transfer characteristics for an EGOFET with gold electrode, 100mM NaCl in DI water, at three scan rates: a) 8 mV/s; b) 20 mV/s; c) 80 mV/s.

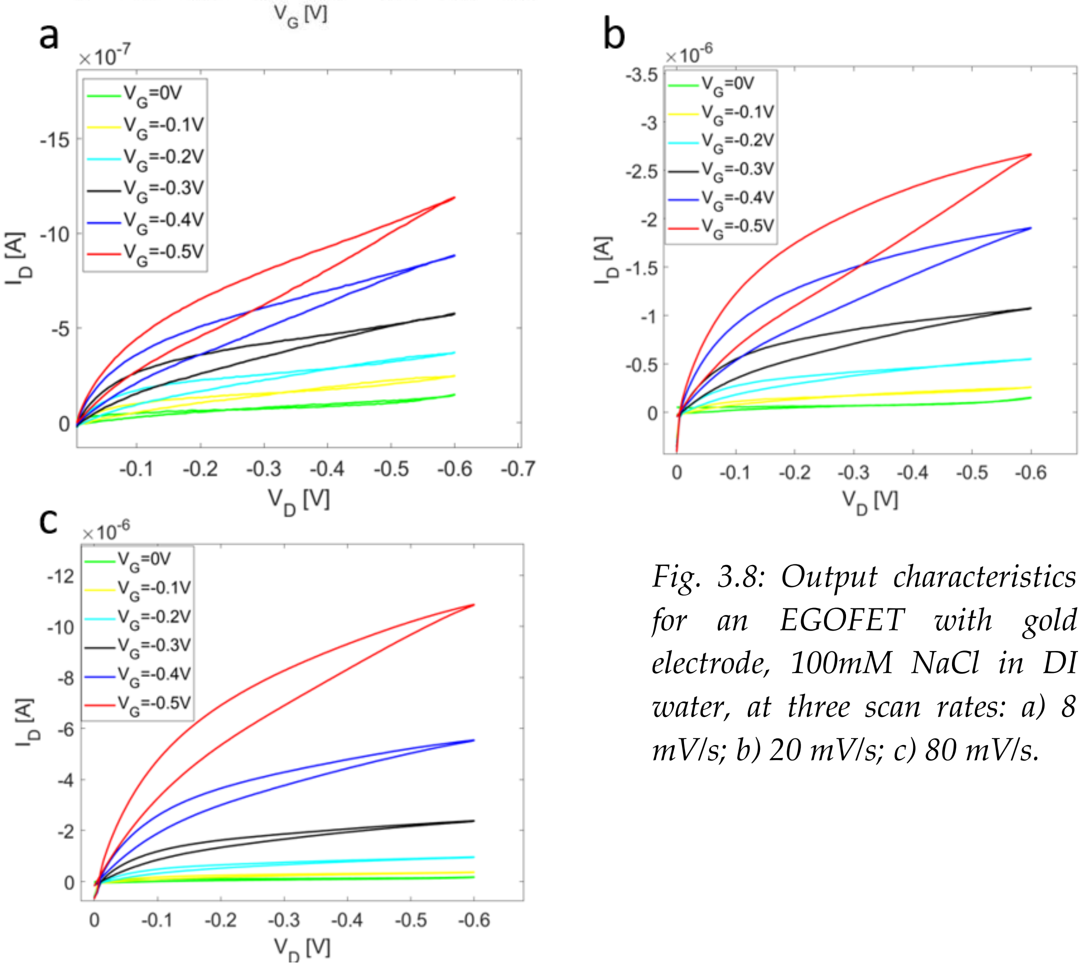

Fig. 3.8: Output characteristics for an EGOFET with gold electrode, 100mM NaCl in DI water, at three scan rates: a) 8 mV/s; b) 20 mV/s; c) 80 mV/s.

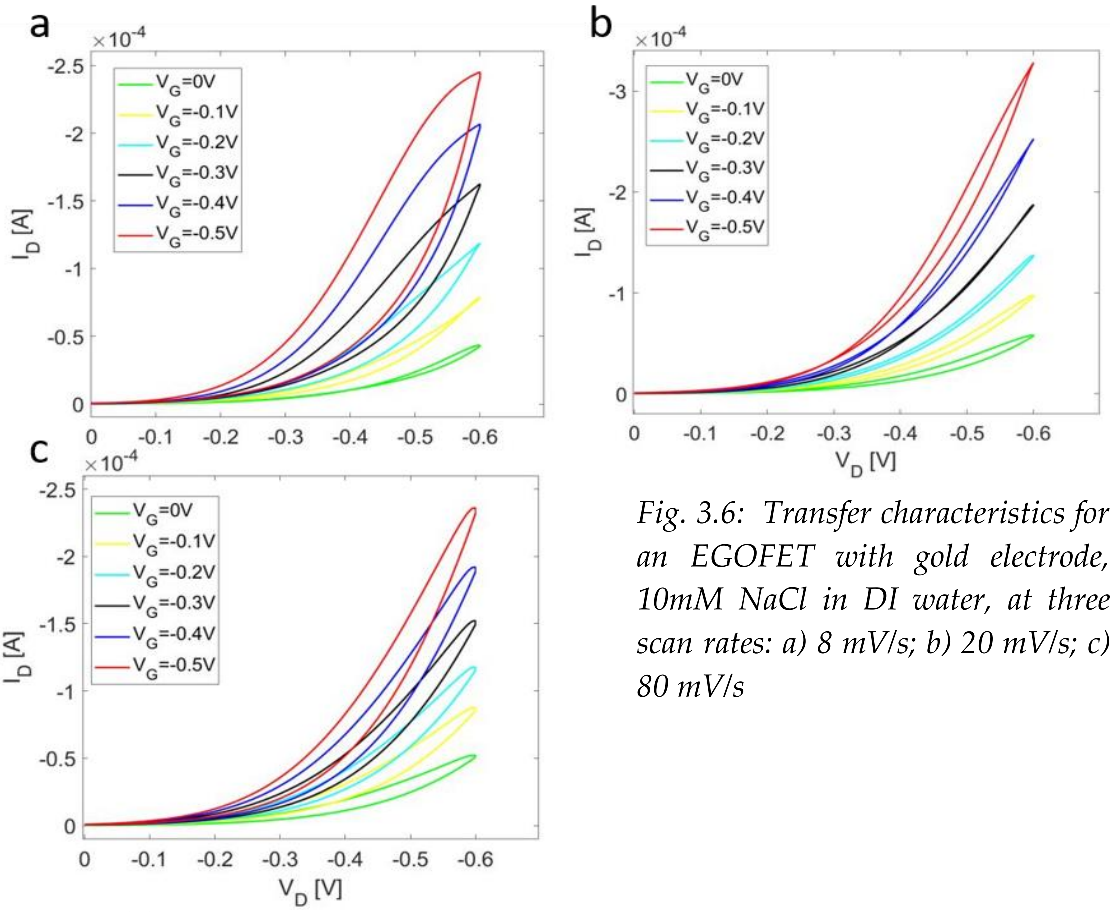

Fig. 3.6: Transfer characteristics for an EGOFET with gold electrode, 10mM NaCl in DI water, at three scan rates: a) 8 mV/s; b) 20 mV/s; c) 80 mV/s

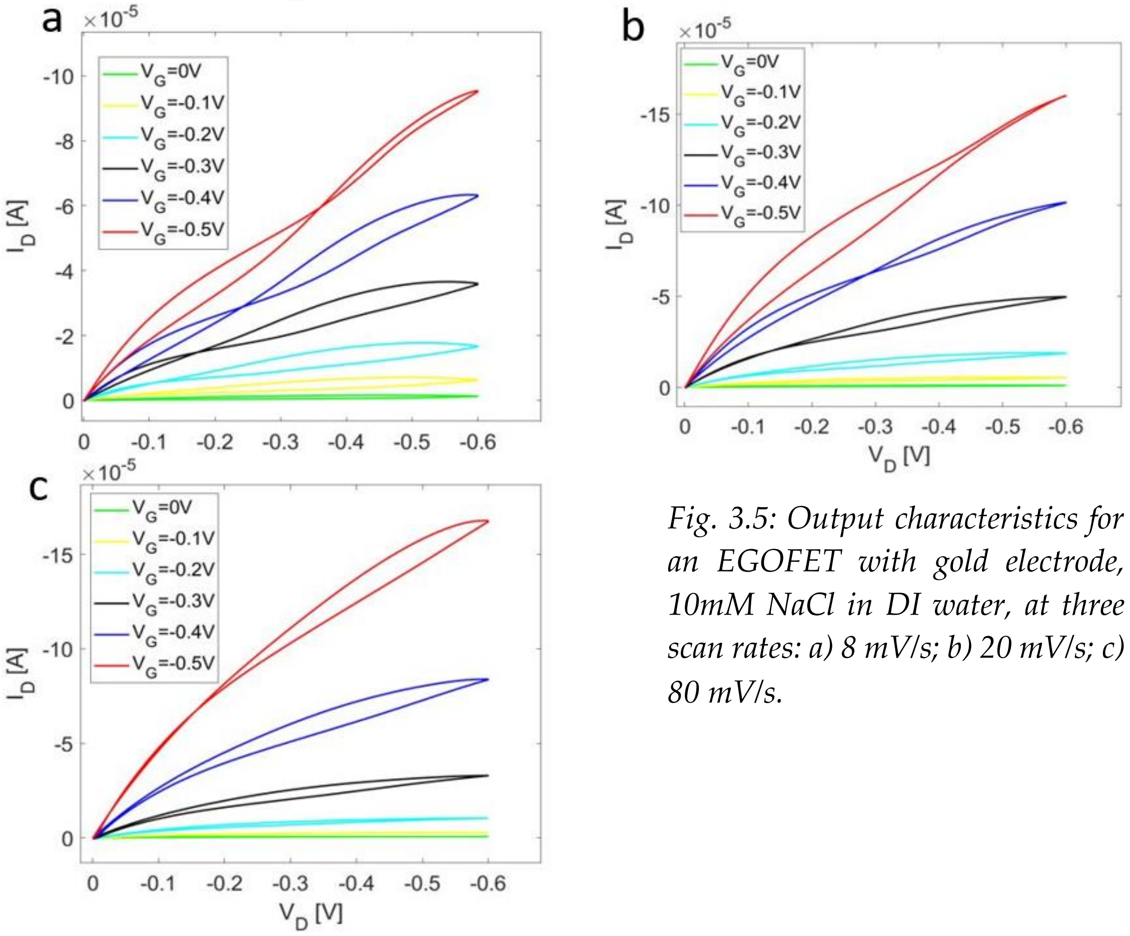

Fig. 3.5: Output characteristics for an EGOFET with gold electrode, 10mM NaCl in DI water, at three scan rates: a) 8 mV/s; b) 20 mV/s; c) 80 mV/s.

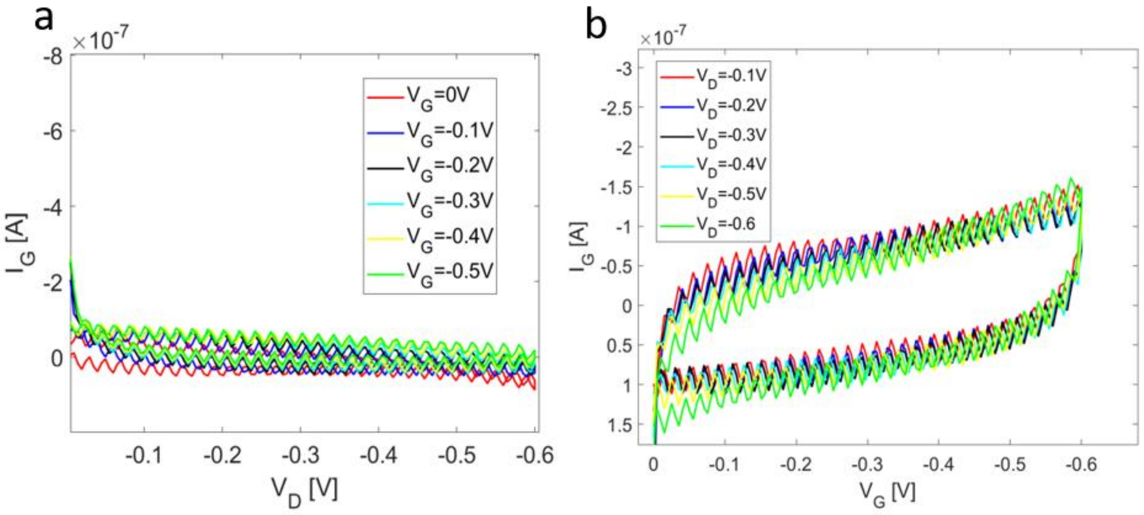

Fig. 3.8: Gate current for an EGOFET with the Au gate electrode, 10mM NaCl in DI water at scan rate 20 mV/s. a) output characteristic b) transfer characteristic.

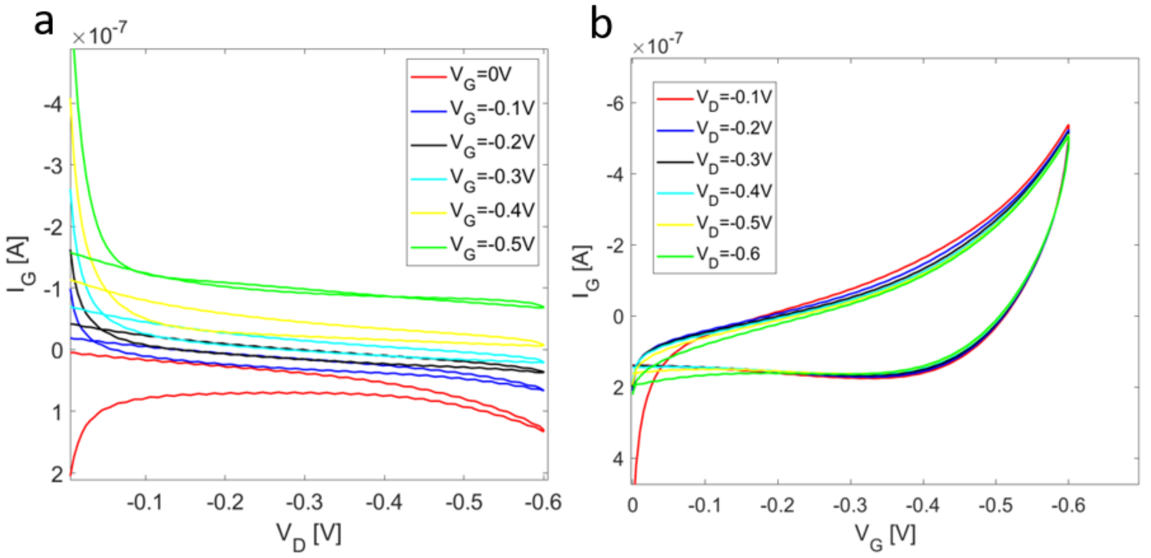

Fig. 3.7: Gate current for an EGOFET with the Ag/AgCl gate electrode, 10mM NaCl in DI water at scan rate 20 mV/s. a) output characteristic b) transfer characteristic.

The EGOFETs exhibit great stability when employed with the Ag/AgCl gate electrode. The output characteristic shows a clear saturation, and already before $V_{DS} = -0.2V$ the current of the device becomes independent from variation of V_{DS}. The transfer characteristics as a natural consequence, appear overlapped, already from $V_D = -0.2V$, that was the voltage where the devices approximately started their saturated behaviour. The recorded on current settles around few hundreds of μA. These values can be considered very high, especially if compared to standard EGOFET with P3HT as OSC [47] [49] [64]: its magnitude improvement ranges from 1 up to 2 orders of magnitude. The devices using a gold gate electrode were able to achieve on currents of the same order of magnitude of those using the Ag/AgCl electrode, but manifested a less stable behaviour, not being able to reach the saturation. In fact, increasing the applied voltage between source and drain terminals the current curve in the output characteristic appears to have more a linear-resistive behaviour. The explanation of this behaviour is related to the electrodes' different response to current flow (see *Chapter 1.3.4*). When, inside the liquid where the gate electrode dipped, a voltage sweep is applied, a polarizable electrode is not capable of maintaining stable the potential at the interface with the electrolyte. Moreover, the linear behaviour of the current I_{DS} at whatever level of V_{DS} is addressable to the difference in the work function among the two electrodes ($q\Phi_{Ag/AgCl} = 4.6\ eV$, $q\Phi_{Au} = 5.1\ eV$) [65]. Even by increasing the range of V_{DS} sweep up to 1 V, the devices did not manage to achieve saturation. Applying even higher voltages is useless because water electrolysis comes into play. A common pattern for these measurements is observed with the variation of the scan rate. Regarding Ag/AgCl-gated samples: with low scan rates ($8\ mV/s$), both output and transfer curves show a very small hysteresis. The operation mode of the EGOFETs can be considered to follow the Field-Effect principles and the small hysteresis can be credited to trapped charges inside the bulk of the semiconductor [47].

The hysteresis is still quite small at scan rate $20\ mV/s$, so the same considerations made at $8\ mV/s$, can still be considered valid at $20\ mV/s$. At faster scan rate ($80\ mV/s$), the hysteresis becomes bigger, as a possible dominance of electrochemical doping mechanism. Increasing the scan rate, also the noise on gate current increases. Regarding the Au-gated samples, same considerations can be made, with the exception that in the electrochemical doping effect is more evident at lower scan rates. These opposite behaviours can be addressed to two different mechanism: in the first case, the trapped charges are in the bulk of the semiconductor and the hysteresis area gets bigger as the scan rate increases as a consequence of majority and minority carriers filling the traps throughout the voltage sweep.

In the second case ions with same polarity of majority carriers, move slowly to the channel where the total charge is fixed by the applied voltage resulting, and the hysteresis gets wider at lower scan rates [66].

3.2 Stability measurements

Stability measurements are performed to check the device behaviour when it undergoes a prolonged electrical stress, such as an overnight measurement. It is well known that the drawback which is the most limiting for EGOFETs wide employment is the performance degradation reported [67]. The same problem can be addressed in this thesis. Overnight experiments started with a well-working device, and by the end of the measurement a consistent reduction in on current flow is observed, as it is clear from *Fig*. 3.9. Overall, all the devices, showed an I_{DS} one order of magnitude below its initial value.

The overnight stress measurement was carried out for a single device within a sample. For all the others, more characterization measurements have been carried out the following day. These measurements have shown that a device kept in-liquid, overnight, the following day can be still considered fresh. In fact, the curves showed no differences whatsoever with respect to the curves showed above (from *Fig. 3.1* to *Fig. 3.11*).

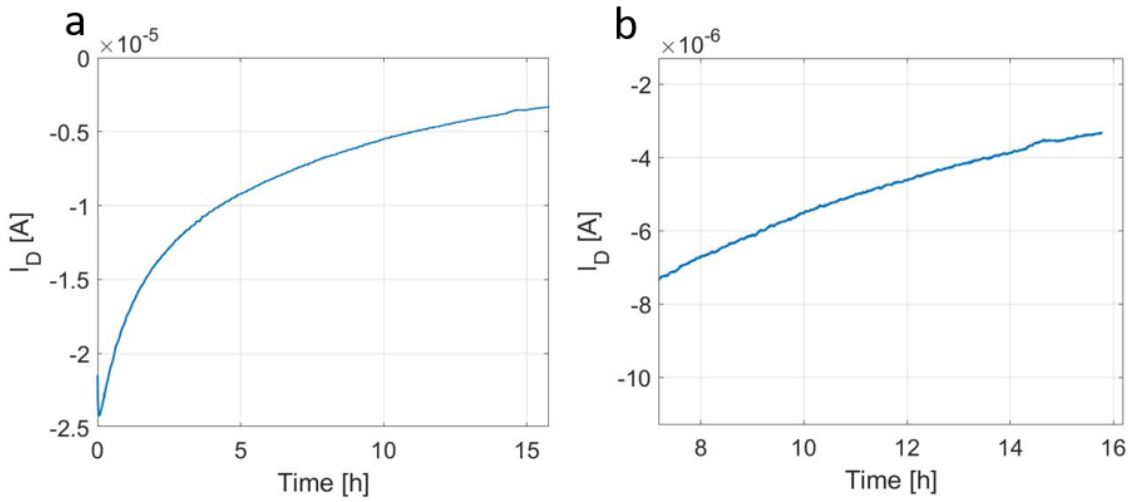

Fig. 3.9: Example of a real-time measurement (Gate: Ag/AgCl. Concentration: 100 mM). On the left the full measurement highlights the double behaviour of the curve. On the right, an insight on the non-exponential part of the measurement. In the last 9 hours the current halves, whereas in the last 2 hours, the current drop is of about 10%

This leads to believe that the degradation of the performance could be mainly addressed to the polymer degradation due to electrical stress than to exposure to external agents (air, water), as it will be examined in *Chapter 3.3.* A common pattern for these type of measurements was that the drain current reduction occurred in the first 3-5 hours of usage; after this stabilization time, the current curve smoothened, giving a curve which could be approximated to a possible baseline for future sensing implementations.

3.3 Figures of merit

Output and transfer curves are used in order to analyse the device in terms of figures of merit.

As it was already stated in the previous chapter, EGOFETs measured with gold as gate electrode showed an overall less stable behaviour than those with Ag/AgCl as gate. Data acquired for the samples with the gold gate and at 1mM ionic strength were not reproducible and will not be discussed in the following.

Given a 100 times repeated transfer characteristic, at scan rate 40 mV/s and fixed $V_{DS} = -0.5V$, by using *(1.2)* it was possible to estimate the transconductance, whose stability under electrical stress is a fundamental requirement for the future biosensor [47]. At each repetition, the maximum value of transconductance was extracted from the curve. Each value was then plotted in $gm_{max}\ vs. measure$ plot (see *Fig. 3.14*) to analyse its stability throughout the measurement. At first glance, the devices using a Ag/AgCl electrode show a higher transconductance of a factor 2-3, than those using an Au electrode, for a fixed concentration of NaCl in the electrolyte. The maximum values reported are in the order of few mS, precisely 2.4 mS for an EGOFET with Ag/AgCl gate electrode and 100 mM of NaCl in DI water, and 1.5 mS for an EGOFET with Au gate electrode and same ionic strength. These values exceed of several order of magnitudes the transconductance reported for EGOFETs employing P3HT as OSC [47], [49].

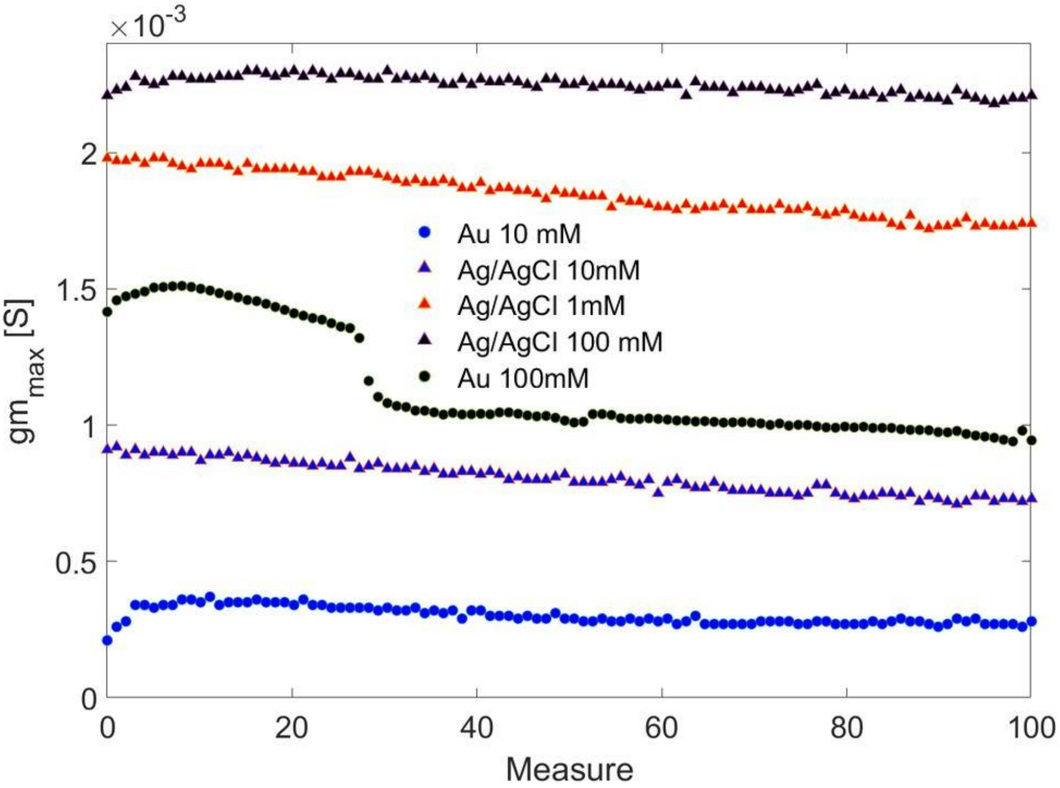

Fig. 3.10: gm_{max} analysed for 100 measurements in a row. The points with same shape indicate same gate electrode, while same colours point out same electrolyte concentration. Rhombuses are plotting the Ag/AgCl electrode, dots are plotting the gold electrode. Black refers to 100mM, blue to 10 mM, red to 1mM.

The devices employing the Ag/AgCl gate electrode also appear to be more stable, as it is better understandable from the normalized plot in *Fig*. 3.15. The normalization has been done for the maximum value transconductance, which always occurred in one of the first repetitions.EGOFETs with gate in Ag/AgCl, display a transconductance drop between the 5-20% to its maximum value, after 100 measurements. The stability of the Au gate electrode is worse: the transconductance drops in the range of 30-40% with respect to its maximum value. Transconductance degradation can be one electrical parameter to justify the performance degradation upon usage of the EGOFETs.

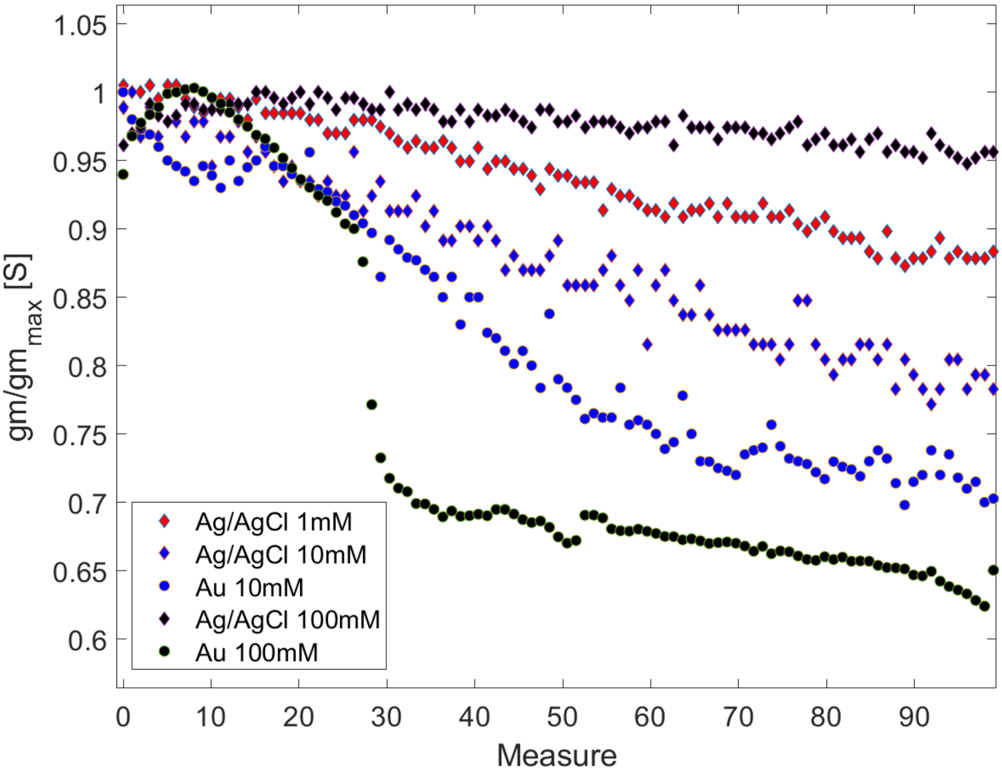

Fig. 3.11: gm normalized at the maximum gm. Also in this case, same shape is related to same electrodes (Ag/AgCl = circles; Au = rhombuses), whereas same colours are related to the concentrations (100mM = black; 10mM = blue; 1mM = red).

The threshold voltage has been extracted as described in *Chapter 1.3.2*. The greater stability of the characterization curves with gate in Ag/AgCl is translated in much more reliable devices behaviour. The range of threshold voltage for the non-polarizable electrode is between $-0.4\ V$ with standard deviation around few tens of mV, while the possible range is much wider ($-0.3\ \pm 0.04\ V$ and $-0.35 \pm 0.06\ V$) for the polarizable gold gate. The difference in the threshold voltage could be addressed to the work function of the two electrodes [68]. In fact, threshold voltage is directly related to the work function through the flat band voltage V_{FB} formula:

$$V_{FB} = \frac{W_{GATE} - W_{P3CPT}}{q} - \frac{Qi}{C} \tag{2.1}$$

Where W_{GATE} and W_{P3CPT} are the work functions, respectively of the gate and of the polymer, q is the elementary charge, Qi the charge density at the interface gate/electrolyte and C the electrical double layer capacitance.

By recalling *Chapter 1.3.2*, it is understood that the fitted part of the $\sqrt{Ids}\ vs.\ Vgs$ must be linear, because the device is working in saturation regime. In the ideal case, after the saturation point of the corresponding output curves, the $\sqrt{Ids}\ vs.\ Vgs$ should overlap for an accurate fit, which is not the case. It is clearer that variations from the expected theorical results and the wider standard deviations for the gold electrode could be addressed to the distortion of the output curves. Threshold voltage statistical distribution is shown in *Fig. 3.16.*

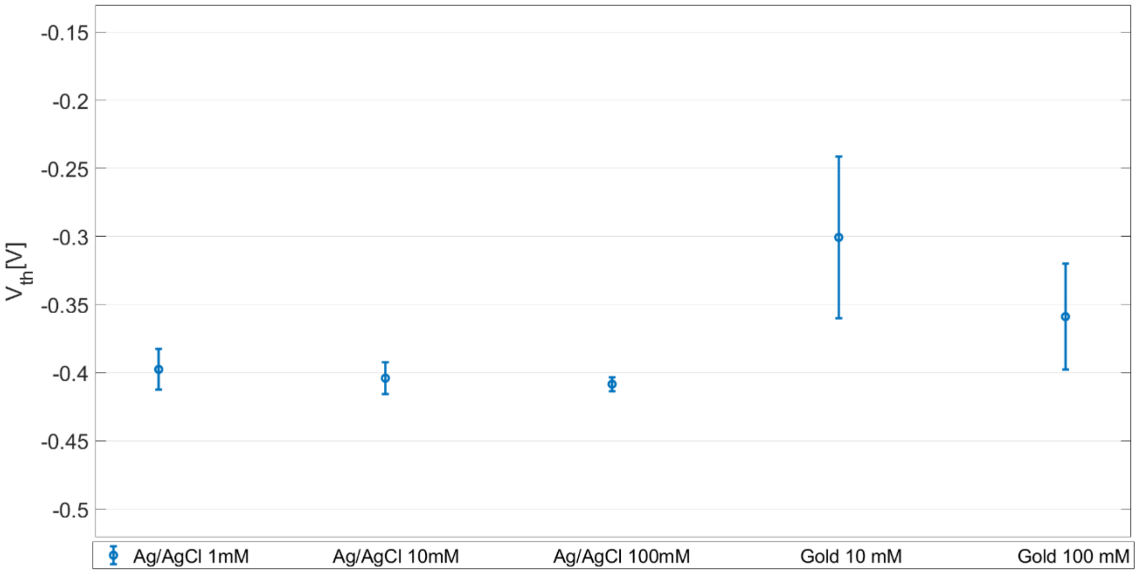

Fig. 3.12: Threshold voltage displayed according to electrodes and electrolyte concentration. The errorbar shows the standard deviation of the statistic.

After the overnight stress, another round of characterization was performed on the samples. In this way it was possible to monitor the threshold voltage, after the electrical stress. The prolonged electrical stress samples undergone is translated in a shift towards higher threshold voltages (in magnitude). These results were found consistent only for the Ag/AgCl-gated samples, as shown in *Fig*. 3.13. The results for Au-gated samples are shown in

8.

Gate voltage pulse measurements (see *Chapter 1.3.2*) were performed to evaluate the electrical double layer capacitance. Data displays the capacitance per unit area, settles around $150 - 300\ \mu F/cm^2$ for devices using an Ag/AgCl gate, while for devices using an Au gate it settles within the range 60-90 $\mu F/cm^2$.The statistical data are depicted in *Fig. 3.19.*

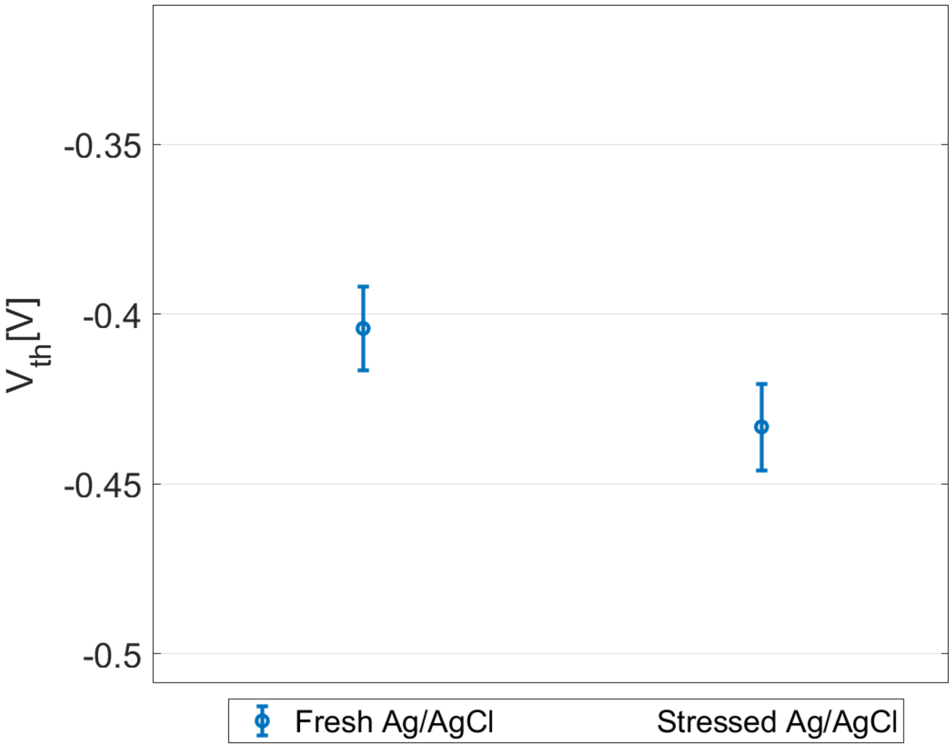

Fig. 3.13: Threshold voltage comparison of fresh samples vs. samples after the overnight stress. The plot represents Ag/AgCl gated devices only. The errorbar represents the standard deviation of the statistic.

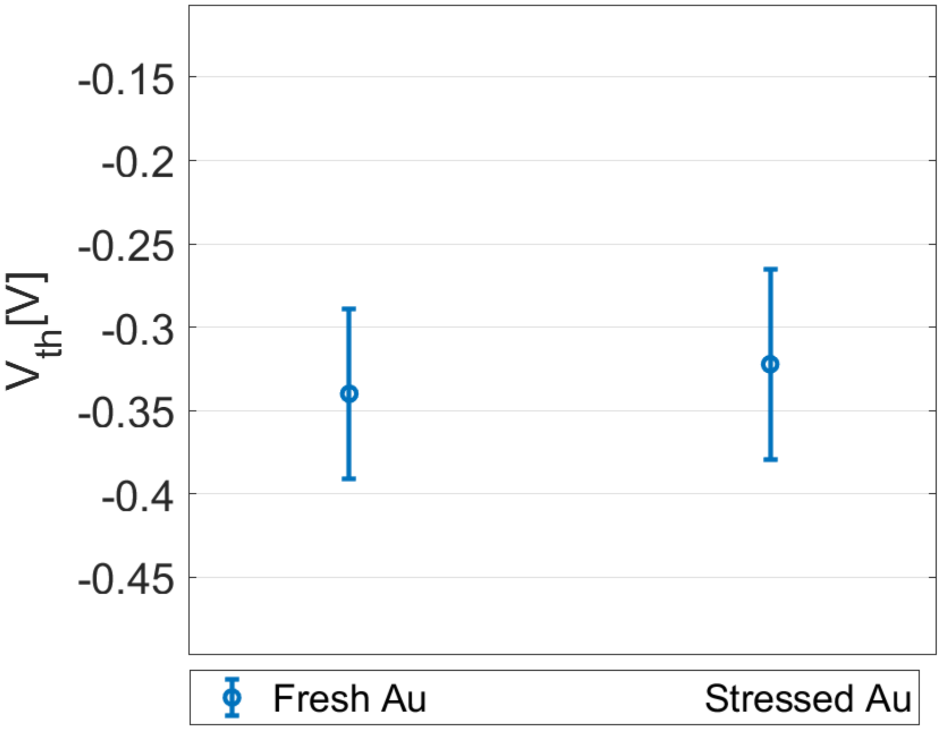

Fig. 3.148: Threshold voltage comparison of fresh samples vs. samples after the overnight stress. The plot represents Au gated devices only. The errorbar represents the standard deviation of the statistic.

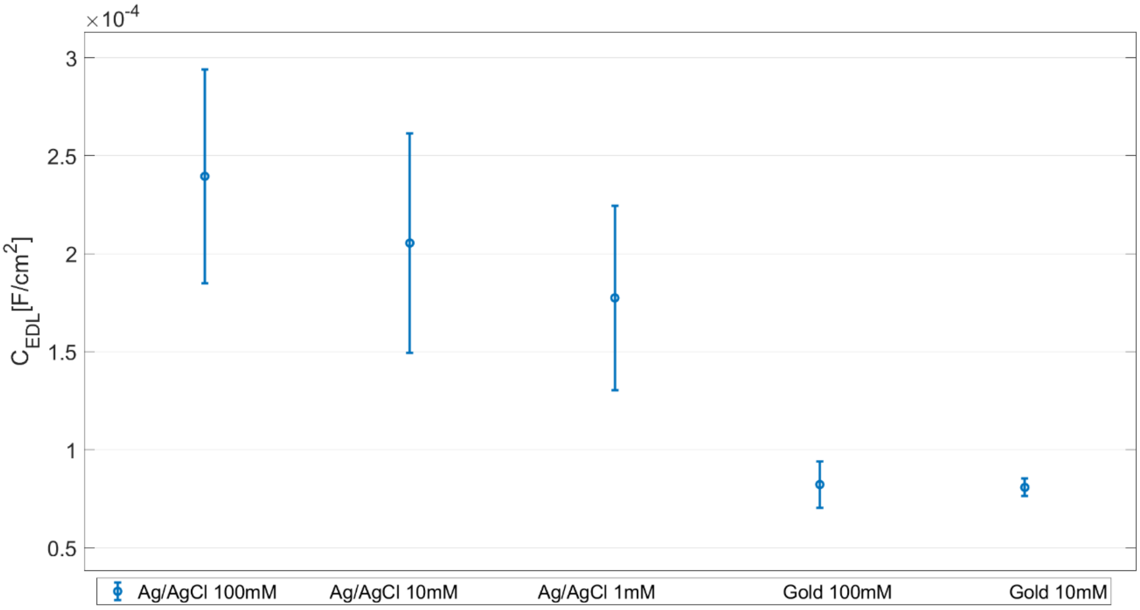

Fig. 3.15: Electrical double layer capacitance. The errorbar is given by the standard deviation of data. The dot represents the mean value, calculated as the arithmetic average of data.

Devices with either gate electrode, exhibit a capacitance of one order of magnitude higher than the one typical of EGOFETs having P3HT as OSC [69]. This might be related to the lateral chains that differentiate P3CPenT from P3HT. P3HT is made up by a methyl group in the sidechain, while P3CPenT ends up in a carboxylic group. The first is an apolar group; the second, the carboxylic group, has polar nature instead, consequently it naturally attracts ions.

However, the capacitance found is comparable with values obtained with the same OSC [70]. To be underlined that gate voltage pulse measurements give a measure of the total capacitance of the gate stack and not just the one of the electrical double layer at the electrolyte/OSC interface.

Recalling *Chapter 1.3.4*, the ideally non-polarizable electrode allows a steady-state current flow such that the electrode behaves like a shortcircuit at the interface with the electrolyte since no electrical double layer is present. The measured value can be addressed only to the EDL at the interface with the polymer. As it is clear from *Fig. 3.16*, the polarizable gold electrode, allows the formation of a further EDL at the electrode/electrolyte interface because of its tendency to follow the applied potential and the total capacitance is given by the series of the two as it follows:

$$C_{TOT} = \frac{C_G \cdot C_{DL}}{C_G + C_{DL}} \tag{3.1}$$

Where C_G is the capacitance at the gate/electrolyte interface and C_{DL} is referred to the double layer capacitance of the OSC/electrolyte interface. To be reminded that this value can be approximated to one of the two capacitance in the case the other of the two is much bigger. Seeing that the total gate stack capacitance among the two gate electrodes is different ($200 - 300$ µF/cm^2 for Ag/AgCl and $60 - 80$ µF/cm^2 for Au), might lead to think that the polymer capacitance is not too small with respect to the gate/electrolyte interface capacitance, or at least big enough to give rise to an appreciable capacitance partition. If, as suspected, P3CPenT capacitance is not high enough to be negligible, at least in first approximation, then the difference seen in *Fig. 3.19* is due to the gate capacitance.

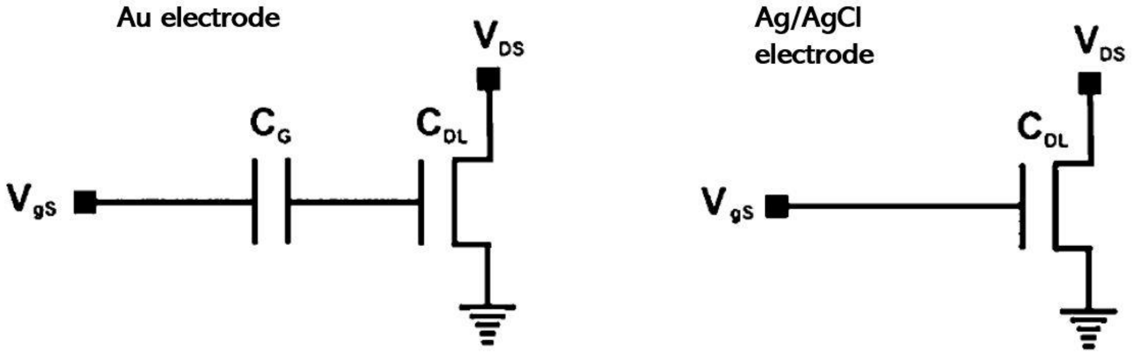

Fig. 3.16: Electrical equivalent model for the two electrodes. C_G is the electrode/electrolyte interface capacitance, while C_{DL} is the polymer/electrode interface capacitance.

Moreover, also the electrolyte concentration plays a role in the electrical double layer strength, as already reported with P3HT and KCl solutions [71]

To confirm the hypothesis of gate capacitance contribution, the reverse path can be taken, evaluating the capacitance analytically from *Equation (1.4)*, where:

- Vth is the mean value taken from the data displayed in *Fig. 3.16*
- Holes mobility (μ) is fixed at $30 \cdot 10^{-3}\ cm^2/Vs$ [70]
- The slope of the output curves is fitted as described for mobility in *Chapter 1.3.2*

The capacitance extracted with this method and listed in *Table 2*, shows averagely the same of magnitude with the values found before. These results seem to confirm that the capacitance variations in *Fig. 3.19* can be ascribed to gate capacitance variations because they have been found to be similar with different (and opposite) methods of extraction.

ELECTRODE	Vth [V]	μ [cm^2/Vs]	m (Ids/Vds)	C [μF/cm^2]
Ag/AgCl (100mM)	-0.408	0.03	0.126	200
Ag/AgCl (10mM)	-0.404	0.03	0.081	120
Ag/AgCl (1mM)	-0.388	0.03	0.468	560
Au (100mM)	-0.360	0.03	0.057	180
Au (10mM)	-0.301	0.03	0.059	170

Table 2: Listing of the changing parameters for capacitance calculation, with fixed charge carrier mobility.

Finally, mobility can be extracted from *Equation (1.4)*, with all the parameters calculated up to now listed in *Table 3*. The mobility shows constant values around $0.05 - 0.1\ cm^2/V \cdot s$, with the exception of the devices at concentration $1\ mM$, which in turn exhibit a mobility in the range of $0.25 - 0.35\ cm^2/V \cdot s$, and those at $100\ mM$ with Ag/AgCl gate that show a slightly worse device-to-device reproducibility. Holes mobility is not expected to change much in the various cases since the thin film polymers were fabricated following the same process.

The obtained values are consistent with values found in literature for standard polythiophenes [72], [73].

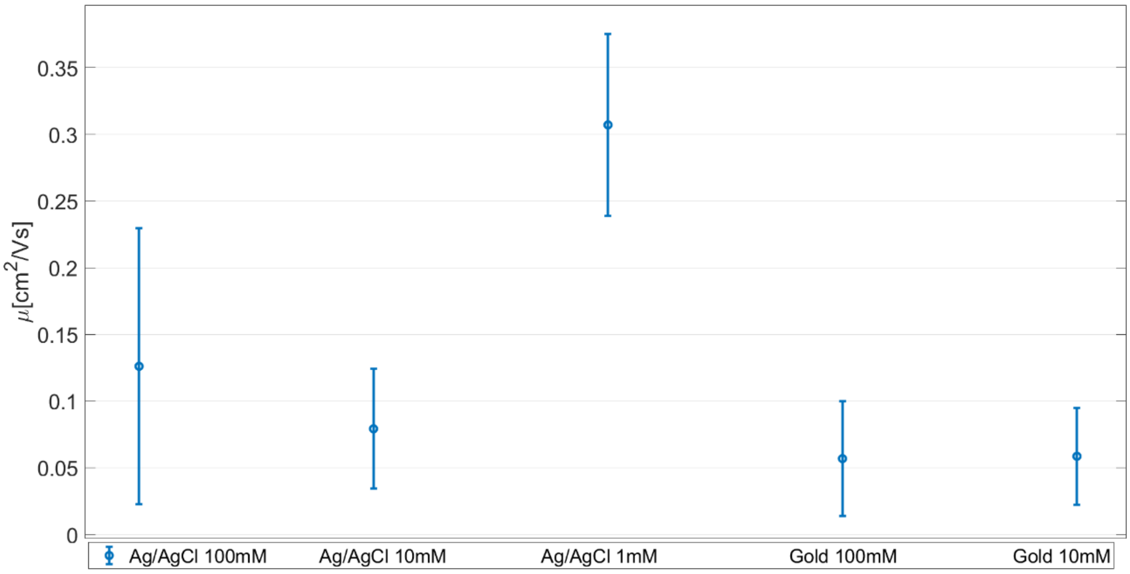

Fig. 3.17: Mobility extracted with parameters listed in Table 3

ELECTRODE	**Vth [V]**	**C [μF/cm^2]**	**m (Ids/Vds)**
Ag/AgCl (100mM)	-0.408	240	0.126
Ag/AgCl (10mM)	-0.404	210	0.079
Ag/AgCl (1mM)	-0.388	180	0.468
Au (100mM)	-0.360	825	0.057
Au (10mM)	-0.301	770	0.059

Table 3: Listing of the changing parameters for mobility calculation, with capacitance extracted from the gate voltage pulse measurements and from output characteristics measured at Vgs= -0.5 V.

4 Conclusions and future work

In conclusion, characterization and stability tests were performed over a set of EGOFETs. The samples were fabricated with a standard photolithographic process, followed by the deposition of the polymer under study, through spin-coating.

Results using the leak-free Ag/AgCl electrode as gate electrode offered much more stable and repeatable performance. Ag/AgCl, being a reference electrode, is a very stable electrode per se. The large number of measurements and electrical characterizations performed with this electrode make the shown results reliable. The gold electrode instead, did not offer performance as excellent as the former, but it cannot be excluded from the projects because it results really easy to functionalize. Functionalization is a crucial step for the future development of the device. EGOFETs can work as biosensor only if a proper functionalization is applied, either to the gate or to the polymer. By employing the Ag/AgCl electrode as a gate, the functionalization will be required at the polymer level (with the -COOH side chain group): this would lead to a better device overall, with greater stability, device-to-device reproducibility and less affected by electrochemical doping and all the disadvantages related to large hysteresis, such as threshold voltage shift. Alternatively, the gold gate electrode could still be employed. A straightforward functionalization, to be applied directly at the gate, makes up a trade-off against the overall worse performance as shown in the section *Results*. The well-known performance degradation upon time, was not solved. However, the acknowledgement of current of higher orders, higher channel control, keeping a relatively high mobility, these results allow to propose P3CPenT as valid possible substitute of state-of-the-art P3HT.

Further investments on the electrical double layer might require more accurate measurements like cyclic voltammetry and electrochemical impedance spectroscopy. Moreover, the speculations done about the threshold voltage might lead to the introduction of a different and more precise method for its extraction.

Another round of characterizations would be useful to better understand the behaviour of gold-gated EGOFETs, especially at lower ionic strengths.

References

[1] M.-P. Marco e D. Barcelò, «Environmental applications of analytical biosensors,» *Measurement and Technology,* vol. 7, n. 11.

[2] M. Malinee, A. Kumar, A. Dhiman e T.-K. Sharman, «Aptamer-Mediated Nanobiosensing for Health Monitoring,» in *Advanced Biosensors for Health Care Applications*, 2019, pp. 227-248.

[3] M. Yahaya, R. Noordin e K. Razak, «Advanced Nanoparticle-Based Biosensors for Diagnosing Foodborne Pathogens,» in *Advanced Biosensors for Health Care Applications*, 2019, pp. 1-43.

[4] D. Rodrigues, A. Barbosa, R. Rebelo, K. R. R. Kwon e V. Correlo, «Skin-IntegratedWearable Systems and Implantable,» *Biosensors,* 21 July 2020.

[5] E. Kisija, D. Osmanovic, J. Nuhic e S. Cifric, «Review of Biosensors in Industrial Process Control,» *CMBEBIH 2019. IFMBE Proceedings,,* vol. 73, pp. 687-694, 2019.

[6] S. Neethirajan, «Recent advances in wearable sensors for animal health management,» *Sensing and Bio-Sensing Research,* vol. 12, pp. 15-21, Feb. 2017.

[7] P. Bergveld, «Development of an Ion-Sensitive Solid-State Device for Neurophysiological Measurements,» *IEEE Transactions on Biomedical Engineering,* Vol. %1 di %2BME-17, n. 1, pp. 70-71, Jan. 1970.

[8] Y. Syu, W. Hsu e C. Lin, «Review - Field-Effect Transistor Biosensing: Devices and Clinical Applications,» *ECS Journal of Solid State Science and Technology,* vol. 7, n. 7, 2018.

[9] L. Clark e C. Lyons, «Electrode systems for continuous monitoring in cardiovascular surgery,» *Annals of the New York Academy Of Sciences,* October 1962.

[10] A. W. A. McNaught, *IUPAC. Compendium of Chemical Terminology, 2nd ed. (the "Gold Book"),* Oxford: Blackwell Scientific Publications, 1997.

[11] J. A. Eggert, M. Palavanzadeh e B. A. , «Screening and Early detecion of lung cancer,» *Seminars in Oncology Nursing,* vol. 33, n. 2, pp. 129-140, 2017.

[12] F. Hirsch, G. Scagliotti, J. Mulshine, R. Kwon, W. Curran, Y. Wu e L. Paz-Ares, «Lung cancer: current therapies and new targeted treatments,» 2016.

[13] M. Schabath e M. Cote, «Cancer Progress and Priorities: Lung Cancer,» *Cancer Epidemiol Biomarkers,* vol. 28, n. 10, p. 1563–1579, 2019.

[14] P. Nanavaty, M. Alvarez e M. Alberts, «Lung Cancer Screening: Advantages, Controversies, and Applications,» *Cancer Control 9,* vol. 21, n. 1, 2014.

[15] D. Kahng e M. Atalla, «Electric Field Controlled Semiconductor Device». Brevetto U. S. Patent No. 3,102,230, 31 May 1960.

[16] J. S., C. S. e S. R. L., «A physical model for drift in pH ISFETs,» *Sensors and Acutators B: Chemical,* vol. 49, n. 1-2, pp. 146-155, June 1998.

[17] P. K. Weimer, «The TFT - A New Thin-Film Transistor,» *Proceedings of the IRE,* vol. 50, n. 6, pp. 1462-1469, June 1963.

[18] A. Tsumura, H. Koezuka e T. Ando, «Macromolecular electronic device: Field-effect transistor with a polythiophene thin film,» *Applied Physics Letters,*, vol. 49, n. 18, pp. 1210-1212, Nov. 1986.

[19] H. Sirringhaus, «Organic Field-Effect Transistors: The Path Beyond Amorphous Silicon,» *Advanced Materials,* vol. 6, n. 9, pp. 1319-1335, 2014.

[20] A. Facchetti, «Semiconductors for organic transistors,» *Materials Today,* vol. 10, n. 3, pp. 28-37, March 2007.

[21] T. Minami, T. Sato, M. T. K. Fukuda, D. Kumaki e T. S. , «A novel OFET-based biosensor for the selective and sensitive detection of lactate levels,» *Biosensors & Bioelectronics,* vol. 74, pp. 45-48, Dec. 2015.

[22] T. Minamiki, S. Tokito e T. Minami, «Fabrication of a Flexible Biosensor Based on an Organic Field-effect Transistor for Lactate Detection,» *Anlytical Science,* vol. 35, n. 1, pp. 103-106, 2019.

[23] D. Sagdullina, N. Lukashkina, A. Parfenova, K. Lyssenkob e T. P., «Highly sensitive OFET-based gas sensors using fluorinated naphthalenediimide semiconductor films,» *Synthetic Metals,* vol. 260, Feb. 2020.

[24] O. H. M. A. A. S. G. M. J. L. T. P. J. B. Z. Knopfmacher, «Highly stable organic polymer field-effect transistor sensor for selective detection in the marine environment,» *Nature communications,* vol. 5, p. 2594, 2014.

[25] I. Manunza e A. Bonfiglio, «Pressure sensing using a completely flexible organic transistor,» *Biosensors and Bioelectronics,* vol. 22, n. 12, pp. 2775-2779, June 2007.

[26] D. Q. T. T. H. B. e. a. Kim, «A Sensor Array Using Multi-functional Field-effect Transistors with Ultrahigh Sensitivity and Precision for Bio-monitoring,» *Scientific Reports,* vol. 5, n. 12705, July 2015.

[27] H. Khana, M. Roberts, O. Johnson, W. Knolla e B. Z., «The effect of pH and DNA concentration on organic thin-film transistor biosensors,» *Organic Electronics,* vol. 13, n. 3, pp. 519-524, March 2015.

[28] Fadliondi, H. Isyanto e P. Chamdareno, «The comparison of organic field effect transistor (OFET) structures,» *2nd International Conference on Frontiers of Sensors Technologies (ICFST),* pp. 6-9, 2017.

[29] Q. Zhang e e. al., «High performing solution-coated electrolyte-gated organic field-effect transistors for aqueous media operation,» *Scientific Reports,* vol. 6, n. 39623, 2016.

[30] E. Macchia, K. Manoli, B. Holzer, C. Di Franco, M. Ghittorelli, F. Torricelli, D. Alberga, G. Mangiatordi, G. Palazzo, G. Scamarcio e L. Torsi, «Single-molecule detection with a millimetre-sized transistor,» *Nature Communications,* vol. 9, n. 3223, 2018.

[31] C. Diacci, M. Berto, M. Di Lauro, E. Bianchini e M. Pinti, «Label-free detection of interleukin-6 using electrolyte gated organic field effect transistors,» *Biointerphases,* vol. 12, n. 5, 2017.

[32] C. Bortolotti, M. Berto, S. M., M. Di Lauro e F. Biscarini, «Biosensing with Electrolyte Gated Organic Field Effect Transistors,» in *Organic Bioelectronics for Life Science and Healthcare*, vol. 56, Millersville, PA 17551, Materials Research Forum LLC, 2019, pp. 71-96.

[33] H. Sinno, Polyelectrolyre Gated Organice Field Effect Transistors: Printing and Electrical Stability, Linköpings Universitet, SE-601 74 Norrköping,

Sweden: Department of Science and Technology (ITN), Linköping University, 2013, 2013.

[34] Z. Stewart, Organic Thin-Film Transistors and TIPS-Pentacene, Lewis Honors College Capstone Collection 11, 2013.

[35] M. Lloyd, J. Anthony e G. Malliaras, «Photovoltaics from soluble small molecules,» *Materials Today,* vol. 10, n. 11, pp. 34-41, 2007.

[36] A. Moliton e R. Hiorns, «Review of electronic and optical properties of semiconducting π-conjugated polymers: applications in optoelectronics,» *Poymer International,* vol. 53, n. 10, pp. 1397-1412, 19 July Oct. 2004.

[37] G. Horowitz, «Organic Field Effect Transistors,» *Advanced Materials,* vol. 10, n. 5, pp. 365-377, 1998.

[38] K. Tremel e S. Ludwigs, «Morphology of P3HT in Thin Films in Relation to Optical and Electrical Properties,» in *P3HT Revisited – From Molecular Scale to Solar Cell Devices*, Berlin, Springer, 2014, pp. 39-82.

[39] J. e. a. Klein, «Critical Role of Side-Chain Attachment Density on the Order and Device Performance of Polythiophenes,» *Macromolecules,* vol. 40, n. 22, pp. 7960-7965, 2007.

[40] M. Dang, L. Hirsch e G. Wantz, «P3HT:PCBM, Best Seller in Polymer Photovoltaic Research,» *Advanced Materials,* vol. 23, n. 31, pp. 3597-3602, 2011.

[41] J. Rogers, Z. K. H. Bao e A. Dodabalapur, «Organic Transistors: Materials, Patterning Techniques and Applications,» in *Thin-Film Transistors*, Taylor & Francis Group, 2003, pp. 386-387.

[42] A. H. L. Lahio, R. Forchheimer, X. Crispin e M. Berggren, «Controlling the dimensionality of charge transport in organic thin-film transistors,» *PNAS,* vol. 108, n. 37, pp. 15069-15073, 13 September 2011.

[43] B. Worfolk e e. al., «Bulk Heterojunction Organic Photovoltaics Based on Carboxylated Polythiophenes and PCBM on Glass and Plastic Substrates,» *Advanced Functional Materials,* vol. 21, n. 10, pp. 1816-1826, April 2011.

[44] Z. Bao e A. Lovinger, «Soluble Regioregular Polythiophene Derivatives as Semiconducting Materials for Field-Effect Transistors,» *Chemistry of Materials,* vol. 11, n. 9, pp. 2607-2612, 1999.

[45] V. Khanna, «Electrolyte-gated organic FET (EGOFET) and organic electrochemical FET (OECFET),» in *Flexible Elextronics, Volume 2*, Bristol, IOP Publishing, 2019, pp. 8-21.

[46] e. a. Ortiz-Conde A., «A review of recent MOSFET threshold voltage extraction methods,» *Microelectronics Reliability,* vol. 42, pp. 583-596, 2002.

[47] M. Parmeggiani, A. Verna, A. Ballesio, M. Cocuzza, E. Piatti, V. Fra, F. Pirri e S. Marass, «P3HT Processing Study for In-Liquid EGOFET Biosensors: Effects of the solvent and the surface,» *Biosensors,* 17 October 2018.

[48] D. Khodagholy, J. Rivnay, M. Sessolo, M. Gurfinkel, P. Leleux, L. Jimison, E. Stavrindou, T. Herve, S. Sanaur, R. Owens e G. Malliaras, «High transconductance organic electrochemical transistors,» *Natue Comminications,* vol. 4, n. 2133, 12 July 2013.

[49] K. Melzer, M. Brandlein, B. Popescu, D. Popescu, P. Lugli e G. Scarpa, «Characterization and simulation of electrolyte-gated organic field-effect transistors,» *Faraday Discussions,* vol. 174, pp. 399-411, 2014.

[50] J. Reynolds, B. THompson e T. Skotheim, «Conjugated Polymer-Based OFET Devices,» in *Conjugated Polymers: Properties, Processing and Applications*, CRC Press, 2019, pp. 10-12.

[51] J. Reynolds, B. Thompson e T. Skotheim, «Conjugated Polymer OFET-Based Devices,» in *Conjugated Polymers: Properties, Processing, and Applications*, CRC, 2019, pp. 11-16.

[52] P. Delahay, Double layers and electrode kinetics, New York: Interscience Publishers, 1965.

[53] J. Lyklema, «Fundamentas of Interface and Colloid Science,» *Solid-Liquid Interface,* vol. 2, pp. 3-1-3-232, 1995.

[54] J. Lyklema, «Electrified interfaces in aqueous dispersions of solids,» *Pure & Applied Chemistry,* vol. 63, n. 6, pp. 895-906, 1991.

[55] A. Barba, S. Bocchicchio, A. Dalmoro, D. Caccavo, S. Cascone e G. Lamberti, «Polymeric and lipid-based systems for controlled drug release: an engineering point of view,» in *Nanomaterials for Drug Delivery and Therapy*, Norwich, NY, William Andrew, 2019, pp. 267-304.

[56] J. Kim, «Electrical double layer: revisit based on boundary conditions,» Texas A&M University , College Station, 2005.

[57] M. Kaszuba, J. Corbett, F. Watson e A. Jones, «High-concentration zeta potential measurements using light-scattering techniques,» *Philos Trans A Math Phys Eng Sci.,* vol. 368, n. 1927, pp. 4439-4451, 2010.

[58] M. Waleed Shinwari, M. Jamal Deen e D. Landheer, «Study of the electrolyte-insulator-semiconductor field-effect transistors (EISFET) with

applications in biosensor design,» *Microelectronics Reliability,* vol. 47, p. 2025–2057, 2007.

[59] D. Harvey, Modern Analytical Chemistry, McGraw-Hill Education, 1999.

[60] M. Jitvisate e J. Seddon, «Direct Measurement of the Differential Capacitance of Solvent-Free and Dilute Ionic Liquids,» *The Journal of Physical Chemistry Letters,* vol. 9, n. 1, pp. 126-131, 2018.

[61] P. Biesheuvel, S. Porada e J. Dykstra, «The difference between Faradaic and non-Faradaic electrode process,» 2018.

[62] J. Rivnay, P. Leleux, M. Ferro, M. Sessolo, A. Williamson e A. Dimitrios, «High-performance transistors for bioelectronics through tuning of channel thickness,» *Science Advances,* vol. 1, n. 4, 2015.

[63] W. Insturments, «Electrophysiology & Cell Biology Research Catalog,» Harvard Apparatus, 2011.

[64] D. Tu, L. Herlogsson, L. Kergoat, X. Crispin e M. Bergren, «A Static Model for Electrolyte-Gated Organic Field-Effect Transistors,» *IEEE Transactions on Electron Devices,,* vol. 58, n. 10, pp. 3574-3582., 2011.

[65] H.-M. Wen, X.-S. L. J.-Y. Z. D.-B. Zhou, Z.-B. Chen, J.-Y. Whan, Z.-C. Chen e Z.-Q. Tian, «Electrical conductance study on 1,3-butadiyne-linked dinuclear ruthenium(ii) complexes within single molecule break junctions,» *Chemical Science,* vol. 6, 2013.

[66] M. Egginger, S. Bauer, R. Schwodiauer, H. Neugebauer e N. Sariciftci, «Current versus gate voltage hysteresis in organic field effect,» *Monatshefte für Chemie - Chemical Monthly,* pp. 735-750, 22 April 2009.

[67] R. Picca, K. Manoli, E. Macchia, A. Tricase, C. Di Franco, G. Scamarcio, N. Cioffi e L. Torsi, «A Study on the Stability of Water-Gated Organic Field-Effect-Transistors Based on a Commercial p-Type Polymer,» *Front. Chem.*, p. 7:667.

[68] L. Kergoat, L. Helogsson, B. Piro, M. Pham, G. Horowitz, C. X. e M. Berggren, «Tuning the threshold voltage in electrolyte-gated organic field-effect transistors,» *PNAS,* vol. 109, n. 22, pp. 8394-8399, 2012.

[69] T. Cramer, A. Campana, F. Leonardi, C. S. A. Kyndiah e M. Murgia, «Water-gated organic field effect transistors – opportunities for biochemical sensing and extracellular signal transduction,» *JCS Mater. Chem.,* p. 3728–3741, 2013.

[70] H. Toss, C. Suspène, B. Piro, A. Yassar, X. Crispin, L. Kergoat, M.-C. Pham e M. Berggren, «On the mode of operation in electrolyte-gated thin film transistors based on different substituted polythiophenes,» *Organic Electronics,* vol. 15, pp. 2420-2427, 2015.

[71] K. Melzer, M. Brandlein, B. Popescu, D. Popescu, P. Lugli e G. Scarpa, «Characterization and simulation of electrolyte-gated field-effect-transistors,» *Faraday Discussions,* vol. 174, n. 399, 2014.

[72] L. Janasz, D. Chelbosz, M. Gradzka, W. Zajaczkowski, T. Marszalek, K. Mullen, A. Ulanski, A. Kiersnowski e W. Pisula, «Improved charge carrier transport in ultrathin poly(3-hexylthiophene) films via solution aggregation,» *Journal of Material Chemistry C,* vol. 4, pp. 11488-11498, 2016.

[73] M.-J. Sher, J. Bartelt, T. Burke, A. Salleo e L. A. McGehee, «Time- and Temperature-Independent Local Carrier Mobility and Effects of Regioregularity in Polymer-Fullerene Organic Semiconductors,» *Advanced Electronic Materials,* vol. 2, n. 3, 2016.

[74] E. Samuelsen e J. Mardelen, «The Structure of Polythiophenes,» in *Handbook of Organic Conductive Molecules and Polymers Vol. 3*, Chichester (UK), Wiley, 1997, pp. 87-120.

[75] M. Vasilopoulou, «Semiconductin Organic Molecules,» in *Encyclopedia of Physical Organic Chemistry, 6 Volume Set*, Hoboken, New Jersey, Wiley, 2018, pp. 3481-3552.

[76] R. Friend, «Electronic Properties of Conjugated Polymers,» in *Physics and Chemistry of Electrons and Ions in Condensed Matter*, Cambridge, UK, Spinger, 1984, pp. 625-651.

[77] I. Salzmann e e. al., «Molecular Electrical Doping of Organic Semiconductors: Fundamental Mechanisms and Emerging Dopant Design Rules,» *ACS Publications,* vol. 49, n. 3, pp. 370-378, 2016.

[78] M. Roesing, J. Howell e D. Boucher, «Solubility characteristics of poly(3-hexylthiophene),» *Journal of Polymer Science Part B: Polymer Physics,* vol. 55, n. 14, pp. 1075-1087, May 2017.

[79] Z. Stewart, «Organic Thin-Film Transistors and TIPS-Pentacene,» Lewis Honors College Capstone Collection. 11, 2013.

[80] C. Sheraw, T. Jackson, D. Eaton e J. Anthony, «Functionalized Pentacene Active Lyer Organic Thin-Film Transistors,» *Advanced Materials,* vol. 15, n. 23, pp. 2009-2011, 2003.

[81] D. Kadri e e. al., «Optimization of 6,13Bis(triisopropylsilylethynyl)pentacene (TIPS-Pentacene) Organic Field Effect Transistor: Annealing Temperature and Solvent Effects,» *Materials Sciences and Applications,* vol. 9, n. 11, 2018.

[82] D. Choi, B. Ahn, S. Kim, K. Hong, M. Ree e C. Park, «High-Performance Triisopropylsilylethynyl Pentacene Transistors via Spin Coating with a Crystallization-Assisting Layer,» *ACS Applied Materias & Interfaces,* vol. 4, n. 1, pp. 117-122, 2012.

[83] D. Bharti e S. Tiwari, «Improved alignment and crystallinity of TIPS-Pentacene thin films by off-center spin coating,» in *2015 IEEE 15th International Conference on Nanotechnology (IEEE-NANO)*, Rome, IEEE, 2015, pp. 432-435.

[84] S. Khandelwal e P. Kushwaha, «Industry Standard FDSOI Compact Model BSIM-IMG for IC Design,» *Electronic and Optical Materials,* pp. 65-87, 2019.

[85] M. Giulianini e N. Motta, «Polymer Self-assembly on Carbon Nanotubes,» in *Self-Assembly of Nanostructures*, New York, Springer Science, 2012, pp. 1-72.

[86] S. Xu, J. Zhan, B. Man, J. S. W. Yue, C. Guo, H. Liu, J. Wang e Y. Zhou, «Real-time reliable determination of binding kinetics of DNA hybridization using a multi-channel graphene biosensor,» *Naure Communications,* vol. 8, n. 14902, 2017.

[87] V. e. a. Parkula, «EGOFET Gated by a Molecular Electronic Switch: A Single-Device Memory Cell,» *Advance Electronic Materials,* vol. 5, n. 6, 2019.

[88] V. e. a. Curto, «Organic transistor platform with integrated microfluidics for in-line multi-parametric in vitro cell monitoring,» *Microsystems and Nanoenergy,* vol. 3, 2017.

[89] P. Lin, X. H. Y. Luo e F. Yan, «Organic Electrochemical Transistors Integrated in Flexible Microfluidic Systems and Used for Label-Free DNA Sensing,» *Advanced Materials,* vol. 23, n. 35, pp. 4035-4040, 2011.

[90] M. Haynes, Handbook of Chemistry and Physics, 91th Edition, CRC, 2009.

[91] M. Kelly, «Electric Field Measurement Techniques,» in *The Earth's Electric Field*, Elsevier Science, 2014, pp. 187-214.